

AD 651914
AFCRL-66-830
DECEMBER 1966
PHYSICAL SCIENCES RESEARCH PAPERS, NO. 299

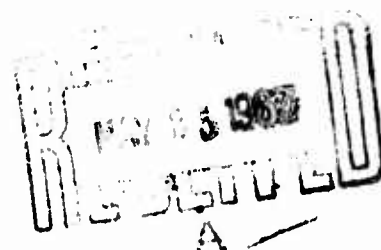


AIR FORCE CAMBRIDGE RESEARCH LABORATORIES

L. G. HANSCOM FIELD, BEDFORD, MASSACHUSETTS

The Interaction of Chromium Ions in Ruby Crystals

RICHARD C. POWELL



**OFFICE OF AEROSPACE RESEARCH
United States Air Force**



ARCHIVE COPY

AFCL-66-830
DECEMBER 1966
PHYSICAL SCIENCES RESEARCH PAPERS, NO. 299



SOLID STATE SCIENCES LABORATORY PROJECT 5620

AIR FORCE CAMBRIDGE RESEARCH LABORATORIES

L. G. HANSCOM FIELD, BEDFORD, MASSACHUSETTS

The Interaction of Chromium Ions in Ruby Crystals

RICHARD C. POWELL

This material was originally submitted in partial fulfillment of the requirements
for the degree of Doctor of Philosophy, Arizona State University

Distribution of this document is unlimited

OFFICE OF AEROSPACE RESEARCH
United States Air Force



Abstract

Absorption, excitation, continuous fluorescence, and pulse fluorescence measurements were made on ruby samples with 0.94 percent and 2.1 percent Cr^{+3} in the temperature range from 4.2°K up to 700°K. The widths, positions, intensities, and lifetimes of the R and N fluorescence lines were determined at numerous temperatures.

The results for the temperature dependence of the linewidths are explained in terms of microscopic strains, Raman scattering of phonons by the impurity ions, and direct phonon processes. The results for the lineshifts with temperature are due to the absorption and emission of virtual phonons. A Debye model of phonons is used with different effective phonon distributions for the linewidth and lineshift processes. Also, the effective phonon distribution for the broadening of pair lines is different than that for the broadening of single-ion lines.

Ratios of the intensities of the R_1 , R_2 , and N_2 lines to the N_1 line are proportional to the relation $\exp [-\Delta E/(KT)]$ at high temperatures but not at low temperatures, indicating that energy transfer between single-ion and double-ion systems is temperature and concentration dependent. The temperature dependence of the relative intensity ratios of the no-phonon lines is used to construct energy level diagrams for two pair systems and to assign the lines to specific transitions.

The observed lifetimes of the R and N lines coincide in the temperature range where the systems are thermalized and the observed decays are pure exponentials. At temperatures where the systems are decoupled, an initial rise in fluorescence is observed at the N lines. The subsequent decay has the lifetime of the R lines for a 0.94 percent sample and the lifetime of the N lines for a 2.1 percent sample.

These results are also explained in terms of energy transfer from single ions to pairs.

The effects of reabsorption on the fluorescence spectrum are also discussed. Selective reabsorption causes the R lines to be self-reversed. Reabsorption effects are also seen in the N_1 and N_2 lines as well as various other lines due to Cr^{+3} ion pairs. The widths of the lines in the reabsorbed spectra are greater than the fluorescence linewidths. The magnitude of these effects is explained by three factors: the dynamics of the excitations, the absorption cross section, and the population of the various levels.

Contents

1. INTRODUCTION	1
2. ENERGY LEVELS AND SPECTRA OF Cr^{+3} IONS IN Al_2O_3	4
2.1 Lightly Doped Ruby	5
2.2 Heavily Doped Ruby	7
3. DYNAMIC CONSIDERATIONS OF A FLUORESCENT SYSTEM	13
3.1 Derivation of the Hamiltonian	14
3.2 Transition Probabilities	24
3.3 Thermal Dependence of the Position, Width, and Shape of Sharp Spectral Lines	32
4. EXPERIMENTAL APPARATUS AND SAMPLES	41
4.1 Samples	41
4.2 Absorption Apparatus	41
4.3 Continuous Fluorescence Apparatus	42
4.4 Apparatus for Excitation Experiments	43
4.5 Pulse Fluorescence Apparatus	44
5. RESULTS AND DISCUSSION OF ABSORPTION EXPERIMENTS	45
5.1 Absorption Spectrum of Lightly Doped Ruby	45
5.2 Absorption Spectrum of Heavily Doped Ruby	47
6. RESULTS AND DISCUSSION OF CONTINUOUS FLUORESCENCE EXPERIMENTS	54
6.1 Fluorescence Spectrum of Lightly Doped Ruby	54
6.2 Fluorescence Spectrum of Heavily Doped Ruby	56
7. RESULTS AND DISCUSSION OF EXCITATION EXPERIMENTS	61
7.1 Excitation Spectrum of the R_1 Line of Lightly Doped Ruby	62
7.2 Excitation Spectra of Heavily Doped Ruby	63

Contents

8. RESULTS AND DISCUSSION OF LINEWIDTH AND LINESHIFT MEASUREMENTS	65
8.1 Theoretical Considerations	65
8.2 Experimental Results	67
8.3 Interpretation of Results and Conclusions	73
9. RESULTS AND DISCUSSION OF RELATIVE INTENSITY MEASUREMENTS	76
9.1 Construction of the Energy Level Systems and Assignments of Transitions	78
9.2 Energy Transfer Between Single-Ion and Pair Systems: Relative Intensities of the R and N Lines	83
10. RESULTS AND DISCUSSION OF FLUORESCENT LIFETIME MEASUREMENTS	86
10.1 Experimental Results	86
10.2 Interpretation of Results	88
10.3 Selective Lifetime Experiments	101
11. RESULTS AND DISCUSSION OF REABSORPTION EXPERIMENTS	102
11.1 Experimental Results	103
11.2 Discussion of Reabsorption Effects	107
11.3 Interpretation of Results	110
12. SUMMARY AND CONCLUSIONS	111
12.1 Summary of Results	111
12.2 Discussions of Results and Conclusions	113
12.3 Implications for Further Work	115
ACKNOWLEDGMENTS	117
REFERENCES	117

Illustrations

1. Structure of the Corundum Lattice	5
2. Ruby Energy Levels	6
3. Continuous Fluorescence Apparatus	42
4. Monochromator Optics	43
5. Pulsed Fluorescence Apparatus	44
6. Absorption Spectra of Ruby with 0.03% Cr at 295°K	46
7. Absorption Spectra of Ruby with 0.03% Cr at 77°K	46
8. Absorption Spectra of Ruby (0.84 mm) with 2.1% Cr at 295°K	47

Illustrations

9. Absorption Spectra of Ruby (0.84 mm) with 2.1% Cr at 77°K	48
10. Absorption Spectra of Ruby (4.26 mm) with 2.1% Cr in the Region of the S, R, and N Lines at 295°K	49
11. Absorption Spectra of Ruby (4.26 mm) with 2.1% Cr in the Region of the R and N Lines at 77°K	50
12. Absorption Spectra of Ruby (4.26 mm) with 2.1% Cr in the Region of the S Lines at 77°K	50
13. Absorption Spectrum ($E \parallel C$) of Ruby (0.84 mm) with 2.1% Cr in the Region of the B Lines at 77°K	52
14. Absorption Spectra of Ruby (4.26 mm) with 2.1% Cr in the Region of the B Lines at 77°K	53
15. Absorption Spectra of Ruby (4.26 mm) with 2.1% Cr in the Region of the "Pair Band"	53
16. Fluorescence Spectrum of Ruby (0.03% Cr)	55
17. Fluorescence Spectrum of Ruby (0.94% Cr)	57
18. Fluorescence Spectrum of Ruby (2.1% Cr)	58
19. Fluorescence Spectrum of Ruby (2.1% Cr) in the Region of the R and N Lines	59
20. Excitation Spectra of the R_1 Line in Ruby with 0.03% Cr at 300°K and 4.2°K	62
21. Excitation Spectra of the R_1 , N_1 , and N_2 Lines and the 7750Å Band in Ruby with 2.1% Cr at 300°K	63
22. Excitation Spectra of the N Lines and the 7750Å Band in Ruby with 2.1% Cr at 4.2°K	64
23. Linewidths of the R and N Lines in Ruby with 2.1% Cr	67
24. Linewidths of the R and N Lines in Ruby with 0.94% Cr	68
25. Energy Shift of the R and N Lines Below Their Values at 0°K for Ruby with 2.1% and 0.94% Cr	69
26. Shape of the N_1 Line in Ruby with 2.1% Cr at 21°K	73
27. Relative Intensities of the R and N Fluorescence Lines in Ruby with 2.1% and 0.94% Cr	79
28. Relative Intensities of Second Nearest Neighbor Pair Lines	80
29. Relative Intensities of the Fourth Nearest Neighbor Pair Lines	81
30. Energy Levels and Transitions of Single Ion and Pair Systems in Ruby	82
31. Cross-relaxation Between Two Fluorescent Systems	84
32. Fluorescent Lifetimes at the R_1 Lines of Ruby (3.76 mm) with 0.03% Cr	88
33. Fluorescent Lifetimes at the R and N Lines in Ruby with 2.1% and 0.94% Cr	90
34. Fluorescent Lifetimes at the 7750Å Band in Ruby with 2.1% and 0.94% Cr	91

Illustrations

35. Examples of Different Types of Decays	92
36. Reabsorbed Spectra of Ruby (2.1% Cr) at 300°K	104
37. Reabsorbed Spectra of Ruby (2.1% Cr) at 125°K	105
38. Reabsorbed Spectra of Ruby (2.1% Cr) at 75°K	106
39. Shape of a Reabsorbed Line	108

Tables

1. Concentration Terminology for Ruby	3
2. Couplings of Cr^{+3} Ions in Ruby	10
3. C_{3v} Product Representations	27
4. C_{3v} Selection Rules	28
5. List of Samples	41
6. Absorption Lines Near the S Lines of Ruby with 2.1% Cr at 77°K	51
7. Absorption Lines Near the B Lines of Ruby with 2.1% Cr at 77°K	51
8. Absorption "Pair Band" in Ruby with 2.1% Cr at 77°K	52
9. Fluorescence Lines of Ruby with 2.1% Cr at 74°K	61
10. Experimental Data on Linewidth of Ruby (2.1% Cr)	70
11. Experimental Data on Linewidth of Ruby (0.94% Cr)	70
12. Experimental Data on Lineshift of Ruby (2.1% Cr)	71
13. Experimental Data on Lineshift of Ruby (0.94% Cr)	72
14. Linewidth and Lineshift Parameters of Ruby	75
15. Fluorescence Intensities of Pair Lines in Ruby with 2.1% Cr	77
16. Relative Intensities of the R and N Lines in Ruby with 2.1% Cr	77
17. Relative Intensities of the R and N Lines in Ruby with 0.94% Cr	78
18. Fluorescent Lifetimes at the R_1 Line in Ruby with 0.03% Cr	87
19. Fluorescent Lifetimes in Ruby with 2.1% Cr	89
20. Fluorescent Lifetimes in Ruby with 0.94% Cr	89
21. Measured Values of t_{max}	91
22. Theoretical Predictions for t_{max}	100
23. Selective Lifetimes in Ruby with 2.1% Cr	101
24. Reabsorption Ratios $I_{\text{ra}}/I_{\text{f}}$	107
25. Linewidths of Reabsorbed Lines	107

The Interaction of Chromium Ions in Ruby Crystals

1. INTRODUCTION

The purpose of this work is to investigate some of the static and dynamic properties of interacting impurity ions in crystals. Because of its importance in quantum electronic devices, ruby has been chosen as an example material for this study.

The extremely rapid development of the laser has given great impetus to both the experimental and theoretical investigations of paramagnetic ions in diamagnetic host lattices. Thus, in recent years, solid state spectroscopy with its interpretation through ligand field theory has become one of the most active and important areas of physics. A great amount of varied information can be obtained through these techniques and applied to the study of numerous physical phenomena. For example, in investigating materials for use as lasers, the interesting spectral features include a wide absorption band, a sharp emission line, and a high quantum efficiency between them.

The experimental techniques and the resulting data are different for the various regions of the spectrum. Optical spectroscopy is the most productive area in terms of information pertinent to the study of laser crystals. Therefore, the present work will deal mainly with this region of the spectrum. The observed spectrum is due to a rearrangement of the coupling of the electrons in the outermost shell of the active ion. Other interesting regions of the spectrum include the

(Received for publication 29 August 1966)

ultraviolet range which yields information on charge transfer processes, the infrared region in which the lattice vibrational frequencies are detected, and the microwave range in which E. P. R. * techniques can be used to study ground state splittings and magnetic properties.

It is possible to categorize the information concerning a fluorescent system which is obtained through solid state spectroscopy as static or dynamic. The former classification includes properties of the fluorescent system per se such as the energy levels and wave functions. The latter category consists of properties of the fluorescence system which arise through the interaction of the system with "external" perturbations such as radiation and lattice vibrations. Examples of this type of information include fluorescent lifetimes and selection rules. The impurity ion can also be used as a probe to extract information about the host lattice and about various phonon processes occurring in the crystal. For example, the fine structure of the "vibronic" bands yields information about characteristic lattice vibrations.

A number of experimental techniques are available in optical spectroscopy. Absorption measurements are made by scanning the monochromatic exciting radiation through the frequency range of interest and detecting the intensity loss of the radiation which passes through the sample at each frequency. The fluorescence spectrum is obtained by exciting a sample with energy spread over a wide range including the main absorption bands and detecting the energy emission at each frequency by scanning over the range of interest. In excitation experiments one emission frequency is monitored while the frequency of the exciting monochromatic light is varied. In pulsed fluorescence experiments a short intense pulse of white light is used to excite the sample and the intensity decay with time of the emission at a specific frequency is monitored. Using the same experimental arrangement with a variable monochromatic pulse yields selective excitation data.

The properties of paramagnetic ions in crystals can best be explained through ligand field theory. In this theory the active ion is considered as being at the center of a coordination polyhedron formed by ligands. The ligands themselves are considered only as point charges which create an electrostatic field surrounding the central ion. Thus, no interaction of the ligand orbitals with those of the central ion can be treated explicitly. Therefore, this model reduces the problem to one of Stark splitting of the energy levels of the magnetic ion in an electrostatic field of specific symmetry. The effect of any covalency in the bonding of the magnetic ion and the ligands is accounted for by adjusting the free ion Racah parameters and the crystal field Dq parameter to give a good theoretical fit with experimental data. A more exact treatment of the problem is given by molecular orbital theory. Combinations of the metal ion and ligand orbitals are formed to give

*Electron paramagnetic resonance

molecular orbitals which account for any overlap. In practice this approach is mathematically cumbersome and generally ligand field theory can explain a large part of the optical spectrum. In the case of ruby, ligand field theory has been quite successful in explaining the observed experimental results.

In general the materials used as lasers have a very low concentration of active ions, for example, standard laser ruby contains 0.05 atomic percent Cr^{+3} . In this situation one paramagnetic ion is completely isolated from the perturbing effects of other paramagnetic ions. At higher impurity concentrations the probability of finding two active ions near together increases and all the ions can no longer be considered as isolated. The interaction between pairs of some of the ions creates an entirely new fluorescent system in the crystal. This is important for several reasons. First, although relatively high concentrations tend to quench the fluorescence (and thus the laser emission) at the normally observed frequencies, it creates the possibility of obtaining laser emission at new frequencies. In fact, laser action has been observed simultaneously at two frequencies in heavily doped ruby due to pair transitions (Schawlow and Devlin, 1961). The pair system in dark ruby is also important in other quantum electronics applications. For example, transitions among the components of the split ground state manifold of the pair systems may be useful for masers and quantum counters in the submillimeter range. From a more basic point of view the study of heavily doped ruby may increase the relatively limited understanding of the phenomena associated with interacting paramagnetic ions in crystals.

This work is an extensive investigation of the spectroscopic properties of heavily doped ruby. Throughout this thesis, the concentration of sample doping is given in atomic percent chromium. The standard terminology which is used is given in Table 1. The properties of pink ruby are summarized and experimental data are presented for the purpose of comparison with dark ruby. The previous work done on heavily doped ruby is discussed and the theory of exchange coupled ion pairs in crystals is developed. Various theoretical topics needed for interpreting the results, such as vibronic transitions and Raman scattering of phonons by impurities, are then developed.

Table 1. Concentration Terminology for Ruby

Color	Relative Amount of Cr Doping	Atomic Percent Cr Concentration
Pink ruby	Lightly doped	Less than 0.1%
Red ruby	Medium doped	0.1% to 0.5%
Dark ruby	Heavily doped	Greater than 0.5%

Several ruby samples with various chromium concentrations were studied. Their absorption spectrum was obtained at room temperature and at 77°K. Complete fluorescence spectra of the samples were obtained at various temperatures from 13°K up to 700°K. Excitation measurements were performed on several of the lines of interest at liquid helium temperature and room temperature. The thermal dependence of line width, line position, line shape, intensity, and fluorescence lifetime were determined for various lines of interest. Reabsorption measurements were also made at various temperatures.

The results of the above experimental work are interpreted in terms of pair effects. A physical model is developed consisting of a host lattice with two types of active impurities, single Cr^{+3} ions and pairs of Cr^{+3} ions. A comparison is made between the effects of various physical phenomena, such as Raman scattering and "vibronic" transitions, on single ions and on coupled pairs of ions. The energy level diagrams are constructed for two nonequivalent pair systems and observed lines are assigned to various transitions within these systems. A cross-relaxation mechanism is developed as a proposed explanation for the transfer of energy from single ions to pairs.

2. ENERGY LEVELS AND SPECTRA OF Cr^{+3} IONS IN Al_2O_3

Ruby is aluminum oxide doped with a small amount of chromium. The α -phase Al_2O_3 host lattice is known as sapphire or corundum. The lattice structure is shown in Figure 1 from Geschwind and Remeika (1962). The planes of oxygen ions are almost hexagonal close-packed. However, the angular distortion of some of the oxygen bonds prevents perfect close-packing and the resulting space group is $R\bar{3}C$ (Wyckoff, 1948). The aluminum ions fit between the oxygen planes with an A-B-C stacking. As seen in Figure 1 the positions of the aluminum ions vary along the C-axis and every third cation site is vacant.

The Cr^{+3} ions enter the host lattice substitutionally for aluminum ions. They are surrounded by six oxygen nearest neighbors in almost octahedral coordination. The ideal site symmetry is characterized by the O_h point group. However, the octahedron is stretched along the three-fold axis corresponding to the C-axis of the crystal. This trigonal distortion lowers the site symmetry to C_{3v} . The angular displacement of the oxygen bonds further lowers the symmetry to C_3 . However, for determining the effects of the crystal field on an impurity Cr^{+3} ion, the cubic O_h symmetry is a good first approximation and the trigonal distortion can be treated as a perturbing effect.

2.1 Lightly Doped Ruby

The optical properties of lightly doped ruby have been thoroughly investigated both experimentally and theoretically. The electronic transitions and resulting spectra are now quite well understood (Sugano and Tanabe, 1958; Sugano and Tsujikawa, 1958; Sugano and Peter, 1961). For concentrations of less than about 0.1% Cr^{+3} the chromium ions can be considered as isolated from any perturbing influences of other chromium ions in the lattice.

The energy levels for ruby are shown in Figure 2. The terms of the free chromium ions are split by the octahedral crystal field into crystal field terms. The total orbital angular momentum L is no longer a good quantum number. The crystal field eigenfunctions transform according to representations of the cubic group and L is replaced by the symbol designating the representation of the cubic group. The total spin S is still a good quantum number in the crystal field.

The octahedral quartet and doublet states are shown in the middle of Figure 2. To the left of these the free ion terms and the crystal configurations are given. The energies of crystal terms with the ground state configuration (t_2^3) do not depend on the crystal field splitting parameter ($10 Dq$) and therefore appear as straight lines in the diagram. Terms belonging to configurations with one or more electrons in e crystal orbitals will be affected by the modulation of $10 Dq$ due to thermal vibrations and they appear as bands in the diagram. The splitting of the octahedral states by the smaller effects of spin-orbit coupling and trigonal distortion is shown on the right side of Figure 2 for the levels that will be discussed later.

The observed absorption and fluorescence spectra can be explained by considering transitions between those energy levels governed by the selection rules discussed in the next section. The absorption and fluorescence spectra are discussed in detail in Sections 5 and 6, respectively. The main features of the absorption spectrum can be divided into two categories, bands and lines. The two most prominent bands are due to transitions from the 4A_2 ground state to the 4T_2 state (U band) and to the 4T_1 state (Y band). There are three groups of lines which appear in the absorption spectrum. The R lines are due to transitions from the ground state to the components of the lowest 2E level split by spin-orbit interaction and the trigonal field.

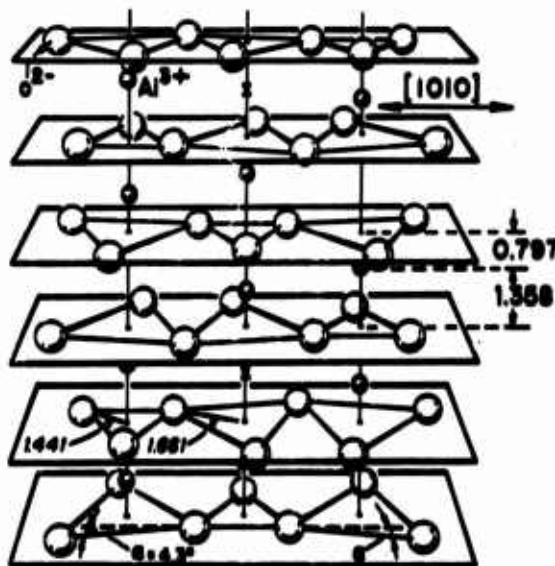


Figure 1. Structure of the Corundum Lattice (after Geschwind and Remelka, 1962)

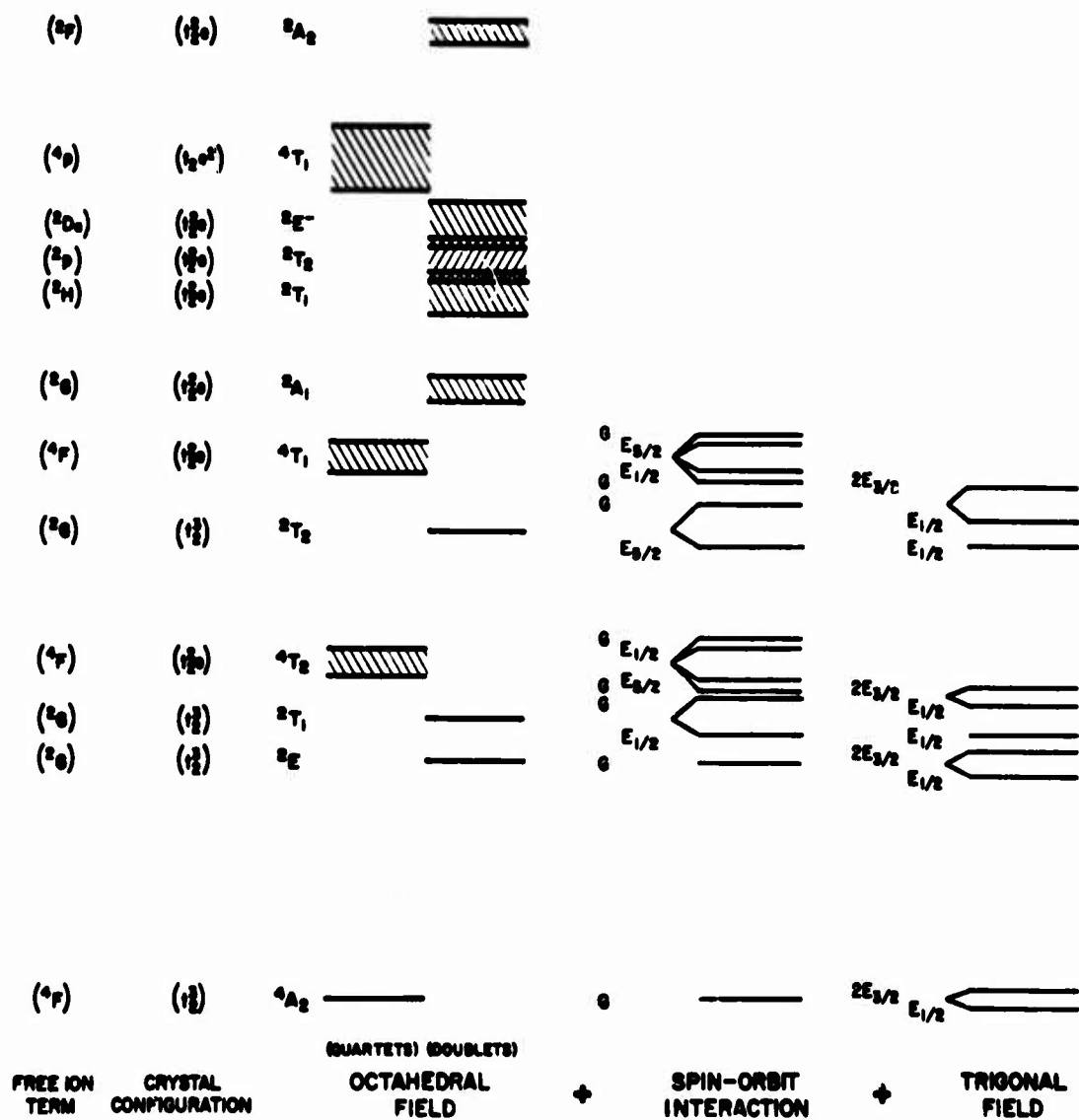


Figure 2. Ruby Energy Levels

The S lines are due to similar transitions to the lowest 2T_1 level. The B lines terminate on the components of the split 2T_2 level between the bands. The most prominent features in the fluorescence spectrum are due to transitions between the split components of the resonant 2E level and the ground state.

2.2 Heavily Doped Ruby

At chromium concentrations greater than those found in lightly doped ruby the probability of forming pairs of chromium ions increases and ion-ion interaction becomes relevant. The number of pairs may be great enough to be significant in spectroscopic investigations. These interacting pairs of ions have different energy levels and spectroscopic properties than the single ions. One of the earliest notable investigations of the spectrum of heavily doped ruby was reported by Deutschbein (1932). He reported the existence of a large number of lines on the low energy side of the two prominent R lines. These were designated "satellite" or N lines. Jacobs (1956) reported the accurate position of 110 lines in the spectrum of heavily doped ruby.

Schawlow et al. (1959) first investigated the concentration dependence of these lines. They found that the relative intensity of the N lines to the R lines increased with concentration, linearly at first and then faster than linearly at higher concentrations. Tolstoi and Abramov (1963) found the same results. The linear increase was explained by attributing the N lines to pairs of coupled ions. The number of ion pairs increases quadratically with concentrations so the intensity ratio of a pair line to a single ion line should depend linearly on concentration. The deviation from linearity was explained in terms of energy transfer from single ions to pairs which is discussed later. Wieder and Sarles (1961) observed stimulated emission in the two most prominent pair lines, N_1 and N_2 . In the same year Schawlow and Devlin (1961) observed simultaneous laser action in these two lines. They interpreted this as indicating that the two lines are associated with different systems of non-equivalent pairs.

The coupling mechanism for the ion pairs has been attributed to exchange interaction because of the antiferromagnetic nature of Cr_2O_3 . The theory of isotropic exchange interaction with an adjustable coupling coefficient J was found to accurately describe the ground state splittings but not those of the excited state (Clogston).

Neglecting the distortion of the environment of one Cr^{+3} ion due to the nearness of another one, we can assume each ion of the pair to be in single ion energy levels. The Hamiltonian for the pair can be written as:

$$H = H_1 + H_2 + H_{\text{interaction}} \quad (1)$$

where the phenomenological coupling term is:

$$H_{\text{int}} = -\frac{J}{\hbar^2} \vec{S}_1 \cdot \vec{S}_2. \quad (2)$$

$J > 0$ corresponds to ferromagnetic coupling, whereas $J < 0$ corresponds to anti-ferromagnetic coupling. As discussed in the last section, the ground state for a Cr^{+3} ion in an octahedral site is ${}^4A_2({}^4F)$. In ruby this is split by spin-orbit interaction and the small trigonal crystal field into two Kramer doublets with spins $M_S = \pm 1/2$ and $M_S = \pm 3/2$. However, this splitting ($\approx 0.38 \text{ cm}^{-1}$) is small compared with the exchange splitting and, therefore, may be neglected. Thus, the ground state for our coupled ion pair is one in which each ion is in its individual ground state with $S_1 = 3/2$. The excited metastable state for the pair occurs when one ion is in the ground state and the other ion is in the 2E single ion state. Matters are complicated here by the splitting of the 2E level of 29 cm^{-1} by spin-orbit interaction and the trigonal field. This is comparable to the exchange splitting.

The single ion ground state term is split by the exchange coupling in the following way. The pair Hamiltonian and its ground state eigenfunction are given by:

$$H_{\text{pair}} = H_1 + H_2 - \frac{J}{\hbar^2} \vec{S}_1 \cdot \vec{S}_2 \quad (3)$$

$$|\psi_{0 \text{ pair}}\rangle = |\psi_0^1\rangle |\psi_0^2\rangle. \quad (4)$$

The complete set of commuting operators for H_{pair} is:

$$H_{\text{pair}}, \vec{S}_1^2, \vec{S}_2^2, \vec{S}^2, \vec{S}_Z.$$

Equation (3) can be put in a different form using

$$\vec{S}_1 \cdot \vec{S}_2 = \frac{\vec{S}^2 - \vec{S}_1^2 - \vec{S}_2^2}{2}. \quad (5)$$

The eigenvalues of \vec{S}^2 and \vec{S}_i^2 are

$$\langle \vec{S}^2 \rangle = \hbar^2 S(S+1), \quad (6)$$

$$\langle \vec{S}_i^2 \rangle = \hbar^2 S_i(S_i+1). \quad (7)$$

For the ground state $S_1 = S_2 = 3/2$. The coupling of two angular momenta of $3/2$ is:

$$S = |S_1 + S_2|, |S_1 + S_2 - 1|, \dots, |S_1 - S_2|,$$

$$S = 3, 2, 1, 0. \quad (8)$$

So the energies of the components of the ground state manifold are:

$$E_{\text{opair}} = \langle \psi_{\text{opair}} | H | \psi_{\text{opair}} \rangle = \langle \psi_0^1 | \langle \psi_0^2 | H_1 + H_2$$

$$- \frac{J}{2\hbar^2} (\vec{S}^2 - \vec{S}_1^2 - \vec{S}_2^2) | \psi_0^1 \rangle | \psi_0^2 \rangle$$

$$= E_0^1 + E_0^2 - \frac{J}{2} [S(S+1) - 3/2(3/2+1) - 3/2(3/2+1)]$$

$$= 2E_0 + \frac{15}{4}J - \frac{J}{2}S(S+1). \quad (9)$$

The first two terms simply shift the energy level without splitting it. However, the last term splits the ground state into four components. Using the values of S from Eq. (8) in Eq. (9) shows the amount of splitting to be:

$$\Delta E = 0, J, 3J, 6J. \quad (10)$$

For ferromagnetic coupling J is positive so the state of lowest energy is $S = 3$. For antiferromagnetic coupling J is negative and the $S = 0$ state has the lowest energy. From this information the energy levels of the ground state manifolds for ferromagnetic and antiferromagnetic coupling can be determined.

In thermal equilibrium the population of a level is given by:

$$n_i = A e^{-E_i/kT}. \quad (11)$$

If several levels are in thermal equilibrium with each other, we can write equations similar to the above one for each state. There is the additional constraint:

$$\sum_i n_i = N. \quad (12)$$

From this we can evaluate A .

$$\sum_i n_i = A \sum_i e^{-E_i/KT} = N$$

$$\therefore A = \frac{N}{\sum_i e^{-E_i/KT}} = \frac{N}{Z}. \quad (13)$$

Here, we let $Z = \sum_i e^{-E_i/KT}$ ~ partition function. The population dependence of the i th state is then given by:

$$n_i = \frac{e^{-E_i/KT}}{Z} N. \quad (14)$$

For the two types of coupling the partition functions are:

$$Z_I = 7 + 5e^{-3J/KT} + 3e^{-5J/KT} + e^{-6J/KT}, \quad (15)$$

$$Z_A = 1 + 3e^{-J/KT} + 5e^{-3J/KT} + 7e^{-6J/KT}, \quad (16)$$

(where the coefficients represent the statistical weights $2S + 1$). A summary of the isotropic exchange splitting and temperature dependence of the level populations is given in Table 2 (Kisliuk et al., 1964).

Table 2. Couplings of Cr^{+3} Ions in Ruby (Kisliuk et al., 1964)

Antiferromagnetic Coupling			Ferromagnetic Coupling		
$H_{\text{EXCH}} = J(\vec{S}_1 \cdot \vec{S}_2)$			$H_{\text{EXCH}} = -J(\vec{S}_1 \cdot \vec{S}_2)$		
$Z_A = 1 + 3e^{-J/KT} + 5e^{-3J/KT} + 7e^{-6J/KT}$			$Z_F = 7 + 5e^{-3J/KT} + 3e^{-5J/KT} + e^{-6J/KT}$		
ENERGY	$S = \vec{S}_1 + \vec{S}_2 $	TEMP DEP	ENERGY	$S = \vec{S}_1 + \vec{S}_2 $	TEMP DEP
6J —	3	$\frac{e^{-6J/KT}}{Z_A}$	6J —	0	$\frac{e^{-6J/KT}}{Z_F}$
3J —	2	$\frac{e^{-3J/KT}}{Z_A}$	5J —	1	$\frac{e^{-5J/KT}}{Z_F}$
J —	1	$\frac{e^{-J/KT}}{Z_A}$	3J —	2	$\frac{e^{-3J/KT}}{Z_F}$
0 —	0	$\frac{1}{Z_A}$	0 —	3	$\frac{1}{Z_F}$

(J is the magnitude of the coupling parameter.)

The theoretical considerations discussed above were used in conjunction with experimental work done by several groups of people to construct energy level diagrams for two non-equivalent types of pairs and to assign twenty-eight lines to specific transitions within the pair systems. Daly attempted to use monochromatic excitation experiments to identify the transitions giving rise to satellite lines (Daly, 1961). He excited the sample with monochromatic light of variable frequency and monitored the fluorescence at a specific N line. Since these experiments were performed at 4°K, the fluorescent transitions were assumed to originate in the lowest components of the excited state manifolds and the absorption transitions to originate in the lowest components of the ground state manifolds. Therefore, fluorescence at a particular frequency was observed only when the excitation energy was at a frequency corresponding to a transition from the ground state to some component of the excited state manifolds. From these experiments the lowest lying components of the metastable states and the various components of the ground state manifolds were obtained along with the assignments of several transitions. The low intensity of the fluorescence caused these measurements to be made with slit widths which were too wide for good resolution.

Kisliuk et al. (1964) investigated the two strongest satellite lines by measuring the temperature dependence of their absorption strength. The problem then was to determine the values of J for the ground states and the initial levels of the various absorption transitions. The temperature dependence of the intensity of a line starting from level E_i is the same as the temperature dependence of the population of E_i and thus is given by Eq. (14). The temperature dependence of the populations of the various components of the ground state were plotted for ferromagnetically coupled pairs and for antiferromagnetically coupled pairs. Some of these curves could then be fit with the points obtained experimentally by assuming specific values of J . For the 7009 Å (N_2) line all three ferromagnetic curves gave a good fit. The $S = 3$ antiferromagnetic curve also fits this data. Using the values of J needed to fit these curves to the experimental data, energy level diagrams were constructed. The transitions predicted from these diagrams were compared with those seen experimentally by Jacobs (1956). Only one set gave a good fit. This fixed the value of J for the 7009 Å line and determined the transitions available to this type of pair. Thus, the 7009 Å line was assigned to a ferromagnetically coupled pair. From the wavelengths given by Jacobs an energy level diagram was constructed which associated three other lines with the same type of pairs. The 7009 Å line was found to terminate on an $S = 1$ level 35 cm^{-1} above the ground state. The value of J was found to be 7 cm^{-1} .

Similar considerations for the 7041 Å (N_1) line showed only fair agreement with experiment. Kisliuk et al. (1964) assigned this transition to an antiferromagnetically coupled pair which terminated on an $S = 1$ level 32 cm^{-1} above the ground state giving a value $J = 32 \text{ cm}^{-1}$ for this line.

Statz et al. (1961) used paramagnetic resonance measurements to investigate the magnitude of the coupling exchange field for various types of pairs. They found that $J = 385 \text{ cm}^{-1}$ for the first nearest neighbors, $J = 1 \text{ cm}^{-1}$ for third and fifth nearest neighbors. The second nearest neighbor coupling constant could not be given a value. The fourth neighbor coupling constant was uncertain and it was suggested that the coupling might be ferromagnetic.

Kisliuk et al. (1964) suggested that for their data to be consistent with that of Statz et al. (1961), the 7009 Å complex should arise from fourth nearest neighbor pairs and the 7041 Å complex from second nearest neighbors. Some work on the piezospectroscopic effect had led to an assignment of the 7041 Å line to the sixth nearest neighbors (Kaplyanskii and Prevuskii, 1962). However, the accuracy of the assignment was not great enough to preclude the fourth nearest neighbor assignment.

After extending their previous investigations to 4.2°K , Kisliuk and Krupke (1965) made a new assignment for the 7041 Å line which gave a closer fit with experiment. They also showed that certain lines disappeared from the absorption spectrum at 4.2°K as predicted theoretically from the temperature dependence of level population. Using the excitation data from Daly's (1961) work and the recurrence of the established ground state energy differences, they were able to assign a number of Jacobs' lines to transitions which established some of the higher levels of the excited state manifolds. Improved values for the ground state splittings were found using a higher order term in the exchange Hamiltonian (Kisliuk and Krupke, 1963). This biquadratic term is $j(\vec{S}_1 \cdot \vec{S}_2)^2$ where

$$j \approx 0.02 J. \quad (17)$$

From this data the 7041 Å line was found to terminate on an $S = 2$ level with $J = 11 \text{ cm}^{-1}$ which was 32.7 cm^{-1} above the ground state. The transition was still thought to arise from an antiferromagnetically coupled pair of second nearest neighbors. Kisliuk and Krupke (1965) pointed out two erroneous assignments of lines in the first paper (Kisliuk et al., 1964). The 7120 Å line was found to be present at low concentrations and thus thought to be a vibronic transition. The 7024.5 Å absorption line was found to disappear at 4.2°K . Since it was assigned to a transition originating in the ground state, it should have been present even at liquid helium temperatures. They suggest that this might be a vibronic transition very near to a forbidden electronic transition.

Recently, Mollenauer (1965) used the results of piezospectroscopic studies to identify lines belonging to first and third nearest neighbors. They were found in the region of the spectrum between 7150 Å and 7550 Å . These pairs were both found to be antiferromagnetically coupled with J values of 183.5 cm^{-1} and 46 cm^{-1} for first and third nearest neighbors, respectively.

From the above considerations, we are led to a physical model of a heavily-doped ruby crystal which consists of a sapphire lattice in which there are two types of optically active centers. One type consists simply of a single Cr^{+3} ion normally found in lightly doped ruby and the other type of an exchange coupled pair of Cr^{+3} ions. These two types of optically active centers give rise to different systems of energy levels. It is possible for the two types of systems to be coupled by some interaction.

It is well known that the single ion R lines are pumped through the Y and U bands. The pair lines also seem to be excited in the same way. However, it appears that there is another excitation mechanism active. This mechanism is the transfer of energy from the single ion system to the pair systems.

As mentioned previously, the greater than linear increase of the intensity ratios of pair lines to single ion lines was attributed to energy transfer from single ion to pairs (Schawlow et al., 1959; Tolstoi and Abramov, 1963). Wieder and Sarles (1961) verified the hypothesis of energy transfer by exciting a red ruby with an R_1 laser pulse and observed the fluorescence in the N_1 and N_2 lines. The mechanism of coupling of the single ion and pair systems was not determined. Recently Imbusch (1966) investigated this energy transfer by measuring the fluorescence lifetimes at the R and N lines. His results are discussed further in Section 10.

One further feature of the spectrum of heavily doped ruby should be mentioned. An absorption band was observed by Linz and Newnham (1961) on the high energy side of the Y band which varies in intensity with the square of the concentration. Naiman and Linz (1963) conclude from their investigations that in this case the pair coupling is not due to an exchange interaction but rather to the transfer of an electron from one of the chromium ions to the other, forming a $d^2 - d^4$ complex.

3. DYNAMIC CONSIDERATIONS OF A FLUORESCENT SYSTEM

Transitions between the various energy levels of the fluorescent system are now discussed. These various processes are due to the fact that the ion finds itself in the presence of two fields of energy, the photon field (external electromagnetic radiation) and the phonon field (thermal vibrations of the crystal lattice). The ion interacts with the electromagnetic radiation by absorbing (or emitting) a quantum of energy from the photon field. This is accompanied by a transition of the ion to a higher (or lower) electronic state. The ion-lattice interaction gives rise to similar processes except that the absorption (or emission) of phonons corresponds to energy changes in the vibrational state of the ion. The lattice vibrations present can be either normal modes of the lattice or local vibrational modes. The total system to be treated now consists of the fluorescent ion plus the phonon field plus the photon field.

3.1 Derivation of the Hamiltonian

The probability per unit time for various transitions can be theoretically predicted. The Hamiltonian for the total system can be written as

$$H = H_0 + H_{em} + H_{latt} + H_{int}^{IE} + H_{int}^{IV}. \quad (18)$$

The expression H_0 includes terms for the electron momentum, the scalar electric potential, the crystal field, and the spin orbit perturbation. H_{latt} and H_{em} are the Hamiltonians representing the phonon and photon fields, respectively. The interaction Hamiltonians for ion-phonon and ion-photon interactions are H_{int}^{IV} and H_{int}^{IE} .

3.1.1 THE PHOTON FIELD

If we consider a single electron ion in an electromagnetic field, the Hamiltonian for the electron is

$$H = \frac{1}{2m} (\vec{p} - \frac{e}{c} \vec{A})^2 + e\phi$$

$$H = \frac{p^2}{2m} + e\phi - \frac{e}{mc} (\vec{p} \cdot \vec{A} + \vec{A} \cdot \vec{p}) + \frac{e^2}{2mc^2} A^2.$$

But,

$$\vec{p} \cdot \vec{A} \psi = \frac{\hbar}{i} \nabla \cdot (\vec{A} \psi) = \frac{\hbar}{i} \vec{A} \cdot \nabla \psi + \frac{\hbar}{i} \psi \nabla \cdot \vec{A} = \vec{A} \cdot \frac{\hbar}{i} \nabla \psi = \vec{A} \cdot \vec{p} \psi$$

(using the Coulomb gauge). Therefore,

$$H = \frac{p^2}{2m} + e\phi - \frac{e}{mc} \vec{A} \cdot \vec{p} + \frac{e^2 A^2}{2mc^2}. \quad (19)$$

So, for an ion with one valence electron in a crystal,

$$H_0 = \frac{p^2}{2m} + e\phi + H_{crystal} + H_{so} \quad (20)$$

and

$$H_{int}^{IE} = - \frac{e}{mc} \vec{A} \cdot \vec{p} + \frac{e^2 A^2}{2mc^2}. \quad (21)$$

(For a many electron ion, we must sum over all the electron coordinates.)

Next, the Hamiltonian of the electromagnetic field itself must be determined. Starting with Maxwell's equations, this can be done in the usual way. Using a Coulomb gauge gives two expressions governing the vector potential.

$$\nabla \cdot \vec{A} = 0. \quad (22)$$

$$\nabla^2 \vec{A} - \frac{1}{c^2} \frac{\partial^2 \vec{A}}{\partial t^2} = 0. \quad (23)$$

Imposing cubic periodic boundary conditions and assuming factored solutions of the form

$$\vec{A}_\alpha(\vec{r}, t) = q_\alpha(t) \vec{A}_\alpha(\vec{r}), \quad (24)$$

we can separate variables in Eq. (23)

$$q_\alpha \nabla^2 \vec{A}_\alpha(\vec{r}) = \frac{1}{c^2} \ddot{q}_\alpha \vec{A}_\alpha(\vec{r}),$$

$$\frac{c^2}{\vec{A}_\alpha(\vec{r})} \nabla^2 \vec{A}_\alpha(\vec{r}) = \frac{\ddot{q}_\alpha}{q_\alpha} = -\omega_\alpha^2,$$

or,

$$\left. \begin{aligned} \ddot{q}_\alpha + \omega_\alpha^2 q_\alpha &= 0 \\ \nabla^2 \vec{A}_\alpha(\vec{r}) + \frac{\omega_\alpha^2}{c^2} \vec{A}_\alpha(\vec{r}) &= 0 \end{aligned} \right\}. \quad (25)$$

The first of Eqs. (25) is simply the harmonic oscillator equation. The second is the equation for a particle in a box. These have solutions of the form

$$q_\alpha = |q_\alpha| e^{-i\omega_\alpha t}$$

$$\vec{A}_\alpha(\vec{r}) = \vec{A} e^{i\vec{K}_\alpha \cdot \vec{r}}, \quad (26)$$

or,

$$\vec{A}_\alpha(\vec{r}) = \hat{e}_\alpha \sqrt{\frac{4\pi c^2}{V}} e^{i\vec{K}_\alpha \cdot \vec{r}}, \quad (27)$$

where the boundary conditions have been used.

$\hat{\pi}_\alpha \sim$ unit vector in the direction of polarization,

$\vec{K} \sim$ propagation vector $(|\vec{K}| = \frac{\omega_\alpha}{c})$.

Thus,

$$\vec{A}_\alpha(\vec{r}, t) = |q_\alpha| \hat{\pi}_\alpha \sqrt{\frac{4\pi c^2}{V}} e^{i(\vec{K}_\alpha \cdot \vec{r} - \omega_\alpha t)}. \quad (28)$$

Since $\nabla \cdot \vec{A} = 0$, we find $\hat{\pi} \cdot \vec{K} = 0$. Therefore, the waves are transverse. Allowing negative values of K and ω , the general expression for $\vec{A}(\vec{r}, t)$ becomes

$$\vec{A}(\vec{r}, t) = \sum_{\text{pol}, \alpha} [q(t) \vec{A}(\vec{r}) + q^*(t) \vec{A}^*(\vec{r})], \quad (29)$$

$$\vec{A}(\vec{r}, t) = \sqrt{\frac{4\pi c^2}{V}} \sum_{\text{pol}, \alpha} |q_\alpha| \hat{\pi} \left[e^{i(\vec{K}_\alpha \cdot \vec{r} - \omega_\alpha t)} + e^{-i(\vec{K}_\alpha \cdot \vec{r} - \omega_\alpha t)} \right]. \quad (30)$$

Now,

$$\vec{E} = -\frac{1}{c} \frac{\partial \vec{A}}{\partial t},$$

$$\therefore \vec{E} = \frac{i\omega}{c} [q \vec{A}(\vec{r}) - q^* \vec{A}^*(\vec{r})]. \quad (31)$$

The Hamiltonian for the radiation field is

$$H_{\text{em}} = \frac{1}{8\pi} \int (E^2 + H^2) d\tau = \frac{1}{4\pi} \int E^2 d\tau.$$

With (31), this becomes

$$H_{\text{em}} = \frac{1}{4\pi} \int \left\{ \sum_{\alpha, \text{pol}} \frac{i\omega_\alpha}{c} (q_\alpha \vec{A}_\alpha(\vec{r}) - q_\alpha^* \vec{A}_\alpha^*(\vec{r})) \right. \\ \left. \times \sum_{\alpha', \text{pol}} \frac{i\omega_{\alpha'}}{c} (q_{\alpha'} \vec{A}_{\alpha'}(\vec{r}) - q_{\alpha'}^* \vec{A}_{\alpha'}^*(\vec{r})) \right\} d\tau.$$

But,

$$\int \vec{A}_\alpha(\vec{r}) \cdot \vec{A}_{\alpha'}(\vec{r}) d\tau = \frac{4\pi c^2}{V} \int e^{i(\vec{K}_\alpha + \vec{K}_{\alpha'}) \cdot \vec{r}} d\tau = 4\pi c^2 \delta_{\alpha, -\alpha'}.$$

Thus,

$$\begin{aligned}
 H_{em} &= - \frac{1}{4\pi c^2} \sum_{\alpha, \alpha', \text{pol}} \omega_{\alpha} \omega_{\alpha'} \int \left\{ \left(q_{\alpha} q_{\alpha'} \vec{A}_{\alpha} \cdot \vec{A}_{\alpha'} + q_{\alpha}^* q_{\alpha'}^* \vec{A}_{\alpha}^* \cdot \vec{A}_{\alpha'}^* \right) \right. \\
 &\quad \left. - \left(q_{\alpha'} q_{\alpha}^* \vec{A}_{\alpha} \cdot \vec{A}_{\alpha'}^* + q_{\alpha} q_{\alpha'} \vec{A}_{\alpha}^* \cdot \vec{A}_{\alpha'} \right) \right\} d\tau, \\
 H_{em} &= \frac{1}{4\pi c^2} \sum_{\alpha, \text{pol}} \omega_{\alpha}^2 2 q_{\alpha} q_{\alpha}^* 4\pi c^2, \\
 H_{em} &= 2 \sum_{\alpha, \text{pol}} \omega_{\alpha}^2 q_{\alpha}^* q_{\alpha}. \tag{32}
 \end{aligned}$$

This can be put in the form of a harmonic oscillator Hamiltonian by the following change of coordinates

$$\left. \begin{aligned} Q_{\alpha} &= q_{\alpha} + q_{\alpha}^* \\ P_{\alpha} &= \dot{Q}_{\alpha} = -\omega_{\alpha} (q_{\alpha} - q_{\alpha}^*) \end{aligned} \right\}. \tag{33}$$

Then,

$$\left. \begin{aligned} q_{\alpha} &= \frac{1}{2} \left(Q_{\alpha} - \frac{1}{i\omega_{\alpha}} P_{\alpha} \right) \\ q_{\alpha}^* &= \frac{1}{2} \left(Q_{\alpha} + \frac{1}{i\omega_{\alpha}} P_{\alpha} \right) \end{aligned} \right\}. \tag{34}$$

So,

$$H_{em} = \frac{1}{2} \sum_{\alpha} \left(P_{\alpha}^2 + \omega_{\alpha}^2 Q_{\alpha}^2 \right). \tag{35}$$

This classical Hamiltonian can be taken into quantum mechanics by means of the relationship between commutators and Poisson brackets. The expressions in Eq. (34) for q_{α} and q_{α}^* can now be expressed in terms of the creation and destruction operators for the quantum mechanical oscillator,

$$\left\{ \begin{aligned} a_{\alpha}^{\lambda} &= \frac{1}{\sqrt{\frac{\hbar}{2\omega_{\alpha}}}} q_{\alpha} = \sqrt{\frac{\omega_{\alpha}}{2\hbar}} \left(Q_{\alpha} - \frac{1}{i\omega_{\alpha}} P_{\alpha} \right) \sim \text{destruction}, \\ a_{\alpha}^{\lambda+} &= \frac{1}{\sqrt{\frac{\hbar}{2\omega_{\alpha}}}} q_{\alpha}^* = \sqrt{\frac{\omega_{\alpha}}{2\hbar}} \left(Q_{\alpha} + \frac{1}{i\omega_{\alpha}} P_{\alpha} \right) \sim \text{creation}. \end{aligned} \right. \tag{36}$$

Substituting these expressions into Eq. (32) gives:

$$H_{em} = \sum_{\alpha, pol} \hbar \omega_{\alpha} \left(a_{\alpha}^{\dagger} a_{\alpha} + \frac{1}{2} \right). \quad (37)$$

The ion-photon interaction Hamiltonian can also be written in terms of the creation and destruction operators by using Eqs. (27), (29), and (36) in Eq. (21)

$$\begin{aligned} H_{int}^{IE} &= - \frac{e}{mc} \vec{A} \cdot \vec{p} + \frac{e^2 A^2}{2mc^2} \\ &= - \frac{e}{m} \sum_{K, \lambda} \frac{\sqrt{2\pi\hbar}}{\sqrt{\omega_K V}} \hat{n}_K^{\lambda} \cdot \vec{p} \left(a_K^{\lambda} e^{i\vec{K} \cdot \vec{r}} + a_K^{\lambda\dagger} e^{-i\vec{K} \cdot \vec{r}} \right) \\ &\quad + \frac{2\pi\hbar e^2}{mV} \sum_{K, \lambda} \sum_{K', \lambda'} \frac{1}{\sqrt{\omega_K \omega_{K'}}} \hat{n}_K^{\lambda} \cdot \hat{n}_{K'}^{\lambda'} \left(a_K^{\lambda} e^{i\vec{K} \cdot \vec{r}} + a_K^{\lambda\dagger} e^{-i\vec{K} \cdot \vec{r}} \right) \\ &\quad \times \left(a_{K'}^{\lambda'} e^{i\vec{K}' \cdot \vec{r}} + a_{K'}^{\lambda'\dagger} e^{-i\vec{K}' \cdot \vec{r}} \right), \\ &= H_1 + H_2. \end{aligned} \quad (38)$$

The creation and destruction operators have the following well-known properties:

$$\left. \begin{aligned} a |n\rangle &= \sqrt{n} |n-1\rangle \\ a^{\dagger} |n\rangle &= \sqrt{n+1} |n+1\rangle \\ \langle n | a^{\dagger} a | n \rangle &= n \\ \langle n-1 | a | n \rangle &= \sqrt{n} \\ \langle n+1 | a^{\dagger} | n \rangle &= \sqrt{n+1} \end{aligned} \right\} \quad (39)$$

3.1.2 THE PHONON FIELD

Next we must account for the presence of the phonon field. The treatment is similar to that of the radiation field. The Hamiltonian for the lattice vibrations can be derived in the standard way (see, for example, Bak, 1964). The atoms in the lattice vibrate about their equilibrium positions. Since the atoms are bound to each other, their vibrations are strongly coupled. The problem is, thus, to find solutions in terms of normal modes and normal coordinates of the lattice, that is, to uncouple the $3N$ components of the vibrations.

Consider a lattice with basic vectors \vec{a}_1 , \vec{a}_2 , and \vec{a}_3 . The position of an ion in the lattice is given by

$$\vec{r}_n = n_1 \vec{a}_1 + n_2 \vec{a}_2 + n_3 \vec{a}_3,$$

where the n_i are integers. Assume that the crystal has one atom per unit cell and contains $N = N_1 \cdot N_2 \cdot N_3$ cells, where N_1 is the number of cells in direction \vec{a}_1 , and so forth.

In the harmonic approximation, only the quadratic term is retained in the expansion of the potential energy about the equilibrium position. Therefore, considering the interatomic forces as being proportional to the relative displacements of the atoms, we can write

$$\left. \begin{aligned} T &= \frac{1}{2} m \sum_{i=1}^N \sum_{\alpha=1}^3 \dot{U}_{i\alpha}^2 \\ V &= \frac{1}{2} \sum_{i=1}^N \sum_{j=1}^N \sum_{\alpha=1}^3 \sum_{\beta=1}^3 A_{i\alpha, j\beta} U_{i\alpha} U_{j\beta} \end{aligned} \right\}, \quad (40)$$

where $U_{i\alpha}(t)$ is the displacement of the i th atom in the α direction at time t , and the $A_{i\alpha, j\beta}$ are constants describing the interatomic forces. Thus, the Hamiltonian for the lattice is

$$H = T + V = \frac{1}{2m} \sum_{i=1}^N \sum_{\alpha=1}^3 p_{i\alpha}^2 + \frac{1}{2} \sum_{i=1}^N \sum_{j=1}^N \sum_{\alpha=1}^3 \sum_{\beta=1}^3 A_{i\alpha, j\beta} U_{i\alpha} U_{j\beta}, \quad (41)$$

where $p_{i\alpha} = m \dot{U}_{i\alpha}$.

We now introduce the complex normal coordinates with the following transformations

$$U_{i\alpha} = \frac{1}{\sqrt{Nm}} \sum_{q\lambda} Q_q^\lambda \epsilon_{q\alpha}^\lambda e^{i\vec{q} \cdot \vec{r}_i}, \quad (42)$$

$$Q_q^\lambda = \sqrt{\frac{m}{N}} \sum_{i\alpha} U_{i\alpha} \epsilon_{q\alpha}^{\lambda*} e^{-i\vec{q} \cdot \vec{r}_i}. \quad (43)$$

where q ranges from 1 to N , λ ranges over the different branches. But,

$Q_{-q}^\lambda = Q_q^{\lambda*}$, so the coordinates associated with \vec{q} and $-\vec{q}$ are not independent.

In order to deal with only the $3N$ independent real coordinates, Eq. (42) can be rewritten as

$$U_{i\alpha} = \frac{1}{\sqrt{Nm}} \sum_{q>0}^{N/2} \left(Q_q^\lambda \epsilon_{q\alpha}^\lambda e^{i\vec{q} \cdot \vec{r}_i} + Q_q^{\lambda*} \epsilon_{q\alpha}^{\lambda*} e^{-i\vec{q} \cdot \vec{r}_i} \right). \quad (44)$$

Equation (42) can now be substituted into Eq. (40) to express the kinetic and potential energy in terms of the normal coordinates. The kinetic energy becomes (Kittel, 1963):*

$$\begin{aligned}
 T &= \frac{m}{2} \sum_{i,\alpha} \left\{ \frac{1}{Nm} \left(\sum_{q,\lambda} \dot{Q}_q^\lambda \epsilon_{q\alpha}^\lambda e^{i\vec{q} \cdot \vec{r}_i} \right) \left(\sum_{q',\lambda'} \dot{Q}_{q'}^{\lambda'} \epsilon_{q'\alpha}^{\lambda'} e^{i\vec{q}' \cdot \vec{r}_i} \right) \right\} \\
 &= \frac{1}{2N} \sum_{i,\alpha} \left\{ \sum_{\substack{q,\lambda \\ q',\lambda'}} \dot{Q}_q^\lambda \dot{Q}_{q'}^{\lambda'} e^{i(\vec{q} + \vec{q}') \cdot \vec{r}_i} \epsilon_{q\alpha}^\lambda \epsilon_{q'\alpha}^{\lambda'} \right\} \\
 &= \frac{1}{2} \sum_{\substack{q,\lambda \\ q',\lambda'}} \dot{Q}_q^\lambda \dot{Q}_{q'}^{\lambda'} \delta_{q',-q} \sum_{\alpha} \epsilon_{q\alpha}^\lambda \epsilon_{q'\alpha}^{\lambda'} \\
 &= \frac{1}{2} \sum_{\substack{q,\lambda \\ \lambda'}} \dot{Q}_q^\lambda \dot{Q}_{-q}^{\lambda'} \delta_{\lambda,\lambda'} \\
 T &= \frac{1}{2} \sum_{q,\lambda} \dot{Q}_q^\lambda \dot{Q}_{-q}^\lambda.
 \end{aligned} \tag{45}$$

Similarly,

$$\begin{aligned}
 V &= \frac{1}{2} \sum_{i,\alpha} \sum_{j,\beta} A_{i\alpha,j\beta} \frac{1}{Nm} \left(\sum_{q,\lambda} Q_q^\lambda \epsilon_{q\alpha}^\lambda e^{i\vec{q} \cdot \vec{r}_i} \right) \left(\sum_{q',\lambda'} Q_{q'}^{\lambda'} \epsilon_{q'\beta}^{\lambda'} e^{i\vec{q}' \cdot \vec{r}_j} \right) \\
 &= \frac{1}{2} \sum_{i,\alpha} \sum_{q,\lambda} \sum_{q',\lambda'} \frac{1}{Nm} \sum_{\beta} \left(\sum_j A_{i\alpha,j\beta} e^{i\vec{q}' \cdot \vec{r}_j} \right) Q_q^\lambda Q_{q'}^{\lambda'} \epsilon_{q\alpha}^\lambda \epsilon_{q'\beta}^{\lambda'} e^{i\vec{q} \cdot \vec{r}_i}.
 \end{aligned}$$

But, we can write

$$\begin{aligned}
 \frac{1}{m} \sum_j A_{i\alpha,j\beta} e^{i\vec{q}' \cdot \vec{r}_j} &= \frac{1}{m} \sum_j A_{i\alpha,j\beta} e^{-i\vec{q}' \cdot (\vec{r}_i - \vec{r}_j)} e^{i\vec{q}' \cdot \vec{r}_i} \\
 &= G_{\alpha\beta}(\vec{q}') e^{i\vec{q}' \cdot \vec{r}_i}.
 \end{aligned}$$

Therefore,

$$\begin{aligned}
 V &= \frac{1}{2} \sum_{i,\alpha} \sum_{q,\lambda} \sum_{q',\lambda'} \frac{1}{N} \sum_{\beta} G_{\alpha\beta}(\vec{q}') e^{i(\vec{q}' + \vec{q}) \cdot \vec{r}_i} Q_q^\lambda Q_{q'}^{\lambda'} \epsilon_{q\alpha}^\lambda \epsilon_{q'\beta}^{\lambda'} \\
 &= \frac{1}{2} \sum_{q,\lambda} \sum_{q',\lambda'} \sum_{\alpha} \sum_{\beta} G_{\alpha\beta}(\vec{q}') \delta_{q',-q} Q_q^\lambda Q_{q'}^{\lambda'} \epsilon_{q\alpha}^\lambda \epsilon_{q'\beta}^{\lambda'}
 \end{aligned}$$

*The orthogonality relations used in this development are derived in the first section.

$$\begin{aligned}
&= \frac{1}{2} \sum_{q,\lambda} \sum_N \sum_{\alpha} \left[\sum_{\beta} G_{\alpha\beta} (-\vec{q}) \epsilon_{-q\beta}^N \right] \epsilon_{q\alpha}^{\lambda} Q_q^{\lambda} Q_{-q}^N \\
&= \frac{1}{2} \sum_{q,\lambda} \sum_N \sum_{\alpha} \omega_{q\lambda}^2 \epsilon_{-q\alpha}^N \epsilon_{q\alpha}^{\lambda} Q_q^{\lambda} Q_{-q}^N \\
&= \frac{1}{2} \sum_{q,\lambda} \sum_N \omega_{q\lambda}^2 \delta_{\lambda,N} Q_q^{\lambda} Q_{-q}^N \\
V &= \frac{1}{2} \sum_{q,\lambda} \omega_{q\lambda}^2 Q_q^{\lambda} Q_{-q}^{\lambda}, \tag{46}
\end{aligned}$$

where

$$\begin{aligned}
\sum_{\beta}^3 G_{\alpha\beta} (-\vec{q}) \epsilon_{-q\beta}^N &= \omega_{q\lambda}^2 \epsilon_{-q\alpha}^N \\
&= \frac{1}{m} \sum_{\beta} \sum_j A_{i\alpha,j\beta} e^{+i\vec{q} \cdot (\vec{r}_i - \vec{r}_j)} \epsilon_{-q\beta}^N. \tag{47}
\end{aligned}$$

The Lagrangian for the system is

$$L = T - V = \frac{1}{2} \sum_{q,\lambda} \dot{Q}_q^{\lambda} \dot{Q}_{-q}^{\lambda} - \frac{1}{2} \sum_{q,\lambda} \omega_{q\lambda}^2 Q_q^{\lambda} Q_{-q}^{\lambda}. \tag{48}$$

Thus, the momentum conjugate to Q_q^{λ} is

$$P_q^{\lambda} = \frac{\partial L}{\partial \dot{Q}_q^{\lambda}} = \dot{Q}_{-q}^{\lambda} = P_{-q}^{\lambda*}. \tag{49}$$

The Hamiltonian is given by

$$\begin{aligned}
H &= \sum_{q,\lambda} P_q^{\lambda} \dot{Q}_q^{\lambda} - L \\
&= \frac{1}{2} \sum_{q,\lambda} P_{-q}^{\lambda} P_q^{\lambda} + \frac{1}{2} \sum_{q,\lambda} \omega_{q\lambda}^2 Q_{-q}^{\lambda} Q_q^{\lambda} \\
&= \frac{1}{2} \sum_{q,\lambda} \left(P_q^{\lambda*} P_q^{\lambda} + \omega_{q\lambda}^2 Q_q^{\lambda*} Q_q^{\lambda} \right). \tag{50}
\end{aligned}$$

In quantum mechanics, P_q^λ and Q_q^λ become non-Hermitian operators and the Hamiltonian can be written as

$$H = \frac{1}{2} \sum_{q,\lambda} \left(P_q^{\lambda\dagger} P_q^\lambda + \omega_{q\lambda}^2 Q_q^{\lambda\dagger} Q_q^\lambda \right). \quad (51)$$

The usual creation and destruction operators can be formed

$$b_q^\lambda = \sqrt{\frac{\omega_{q\lambda}}{2\hbar}} \left(Q_q^\lambda + \frac{i}{\omega_{q\lambda}} P_q^{\lambda\dagger} \right), \quad (52)$$

$$b_q^{\lambda\dagger} = \sqrt{\frac{\omega_{q\lambda}}{2\hbar}} \left(Q_q^{\lambda\dagger} - \frac{i}{\omega_{q\lambda}} P_q^\lambda \right), \quad (53)$$

$$\therefore Q_q^\lambda = \sqrt{\frac{\hbar}{2\omega_{q\lambda}}} \left(b_q^\lambda + b_{-q}^{\lambda\dagger} \right), \quad (54)$$

$$P_q^\lambda = \frac{1}{i} \sqrt{\frac{\hbar\omega_{q\lambda}}{2}} \left(b_{-q}^\lambda - b_q^{\lambda\dagger} \right). \quad (55)$$

These operators have the same properties as the a_α^λ and $a_\alpha^{\lambda\dagger}$.

$$\left. \begin{aligned} b_q^\lambda |n_q^\lambda\rangle &= \sqrt{n_q^\lambda} |n_q^\lambda - 1\rangle \\ b_q^{\lambda\dagger} |n_q^\lambda\rangle &= \sqrt{(n_q^\lambda + 1)} |n_q^\lambda + 1\rangle \end{aligned} \right\}. \quad (56)$$

Thus,

$$H = \sum_{q,\lambda} \frac{3N}{2} \hbar \omega_{q\lambda} \left(b_q^{\lambda\dagger} b_q^\lambda + \frac{1}{2} \right). \quad (57)$$

Finally, the ion-phonon interaction Hamiltonian must be determined. Substituting Eq. (54) into (42) gives the displacement of the atom from its equilibrium position in terms of b_q^λ and $b_q^{\lambda\dagger}$.

$$U_{i\alpha} = \sqrt{\frac{\hbar}{2Nm}} \sum_{q,\lambda} \frac{\epsilon_{q\alpha}^\lambda}{\sqrt{\omega_{q\lambda}}} e^{i\vec{q} \cdot \vec{r}_i} \left(b_q^\lambda + b_{-q}^{\lambda\dagger} \right)$$

$$U_{i\alpha} = \frac{1}{\sqrt{Nm}} \sum_{q,\lambda} \sqrt{\frac{\hbar}{2\omega_{q\lambda}}} \left(\epsilon_{q\alpha}^{\lambda} e^{i\vec{q} \cdot \vec{r}_i} b_q^{\lambda} + \epsilon_{q\alpha}^{\lambda*} e^{-i\vec{q} \cdot \vec{r}_i} b_q^{\lambda\dagger} \right). \quad (58)$$

The ion-phonon interaction takes place through the change in the crystal field due to the change in the relative positions of the active ions and their surrounding ligands. This is proportional to the local strain defined by the tensor

$$\epsilon_{\alpha\beta} = \frac{1}{2} \left(\frac{\partial U_{\alpha}}{\partial X_{\beta}} + \frac{\partial U_{\beta}}{\partial X_{\alpha}} \right). \quad (\alpha, \beta = 1, 2, 3) \quad (59)$$

If we assume that this tensor can be approximated by an average strain

$$\epsilon \approx \frac{\partial U}{\partial X}. \quad (60)$$

Then, from Eq. (58) we find

$$\epsilon = \left. \frac{\partial U}{\partial X} \right|_{X=0} = i \sum_q \sqrt{\frac{\hbar\omega_q}{2Mv^2}} (b_q - b_q^{\dagger}). \quad (61)$$

The expansion of the crystal field in terms of the strain is

$$V_{\text{crystal}} = V_0 + V_1 \epsilon + V_2 \epsilon^2 + \dots \quad (62)$$

Here, V_0 is the H_{crystal} term in Eq. (20). Terms V_1 and V_2 are functions of the electrons on the magnetic ion and of the relative distances between the ion and the ligands. Thus,

$$H_{\text{int}}^{\text{IV}} = V_1 \epsilon + V_2 \epsilon^2 + \dots \quad (63)$$

Therefore, using Eqs. (20), (21), (37), (57), (62), and (63), we can write out (18) explicitly as

$$\begin{aligned}
H = & \frac{p^2}{2m} + \dots + V_0 + H_{so} + \sum_{\alpha, \beta} \hbar \omega_{\alpha\beta} \left(b_{\alpha}^{\dagger} b_{\beta} + 1/2 \right) + \sum_{q, \lambda} \hbar \omega_{q\lambda} \left(b_{q\lambda}^{\dagger} b_{q\lambda} + 1/2 \right) \\
& - \frac{e}{mc} \vec{A} \cdot \vec{p} + \frac{e^2 A^2}{2mc^2} + i V_1 \sum_q \frac{\sqrt{\hbar \omega_q}}{\sqrt{2M V^2}} \left(b_q - b_q^{\dagger} \right) \\
& - V_2 \sum_{q, q'} \frac{\hbar}{2M V^2} \frac{1}{\sqrt{\omega_q \omega_{q'}}} \left(b_q - b_q^{\dagger} \right) \left(b_{q'} - b_{q'}^{\dagger} \right) \dots \quad (64)
\end{aligned}$$

The wave function of the total system can be written as

$$\Psi = |\psi^{el}\rangle |n_1\rangle |n_2\rangle \dots |n_q\rangle \dots |n'_1\rangle |n'_2\rangle \dots |n'_2\rangle \dots, \quad (65)$$

where n_i are phonon occupation numbers and n'_i are photon occupation numbers. The transition probability per unit time (Golden Rule of time-dependent perturbation theory) is:

$$W = \frac{2\pi}{\hbar} |M|^2 \rho_f(E_f = E_i), \quad (66)$$

where M is the transition matrix element and $\rho_f(E)$ is the density of final states.

3.2 Transition Probabilities

3.2.1 ELECTRONIC TRANSITIONS

The probability for electronic transitions can be determined by first finding the matrix elements of H_{int}^{IE} . From the properties of the creation and destruction operators given in (39) it is obvious that the matrix elements for the emission and absorption of photons are

$$\begin{aligned}
M_K^{emission} &= \langle \Psi_f | H_{int}^{IE} | \Psi_i \rangle = \langle \psi_f^{el}; n'_K + 1 | H_1 | \psi_i^{el}; n'_K \rangle \\
&= -\frac{e}{m} \sqrt{\frac{2\pi\hbar}{\omega_K V}} \langle \psi_f^{el} | e^{-i\vec{K} \cdot \vec{r}} \vec{p} \cdot \hat{n}_K^\lambda | \psi_i^{el} \rangle \sqrt{n'_K + 1}. \quad (67)
\end{aligned}$$

$$\begin{aligned}
M_K^{absorption} &= \langle \Psi_f | H_{int}^{IE} | \Psi_i \rangle = \langle \psi_f^{el}; n'_K - 1 | H_1 | \psi_i^{el}; n'_K \rangle \\
&= -\frac{e}{m} \sqrt{\frac{2\pi\hbar}{\omega_K V}} \langle \psi_f^{el} | e^{i\vec{K} \cdot \vec{r}} \vec{p} \cdot \hat{n}_K^\lambda | \psi_i^{el} \rangle \sqrt{n'_K}. \quad (68)
\end{aligned}$$

In order to find the transition probabilities per unit time the density of final states must be determined. Using the boundary conditions imposed previously in obtaining an expression for A_α the density of final photon states is just (see for

example Griffith, 1961).

$$\rho(\nu_K) = \frac{4\pi V}{C^3} \nu_K^2. \quad (69)$$

To evaluate transition probabilities, Eq. (66) is used with the matrix elements from Eqs. (67) and (68) and the density of states given in Eq. (69). This must be summed over polarization and integrated over all angles.

To evaluate the matrix elements in Eq. (67) and (68) the exponential functions are expanded. The first term in the expansion is the electric dipole term. The second term gives the magnetic dipole and electric quadrupole contributions. Higher order terms are usually neglected. Let us now consider the electric dipole interaction. The ionic matrix element can then be written as

$$\langle \psi_f^{el} | \vec{p} \cdot \hat{\pi}_K^\lambda | \psi_i^{el} \rangle \text{ dipole.}$$

But

$$\begin{aligned} \langle \psi_f^{el} | \vec{r} | \psi_i^{el} \rangle &= (E_f - E_i)^{-1} \langle \psi_f^{el} | (H_{ion} \vec{r} - \vec{r} H_{ion}) | \psi_i^{el} \rangle \\ &= (E_f - E_i)^{-1} \left\langle \psi_f^{el} \left| \frac{1}{2m} \vec{p}^2 \vec{r} - \frac{1}{2m} \vec{r} \vec{p}^2 \right| \psi_i^{el} \right\rangle \\ &= \frac{(E_f - E_i)^{-1}}{2m} \langle \psi_f^{el} | [\vec{p}^2, \vec{r}] | \psi_i^{el} \rangle \\ &= \frac{-i\hbar}{m(E_f - E_i)} \langle \psi_f^{el} | \vec{p} | \psi_i^{el} \rangle. \end{aligned}$$

Using this the dipole matrix element becomes

$$im \omega_K \langle \psi_f^{el} | \vec{r} \cdot \hat{\pi}_K^\lambda | \psi_i^{el} \rangle \text{ dipole,} \quad (70)$$

$$\text{where } \omega_K = \frac{E_f - E_i}{K}.$$

Again, for a many electron ion it is necessary to sum over all electron coordinates. Thus, the dipole interaction operator is given by

$$\sum_i e \vec{r}_i. \quad (71)$$

An electric multipole operator of order l has associated with it an orbital angular momentum of $l\hbar$. For conservation of angular momentum $J_f = J_i + l$. So, for the electric dipole operator ($l = 1$), $\Delta J = \pm 1, 0$. (Note, however, that both J_f and J_i cannot be identically zero.) For Russell-Saunders coupling the "multiplicity selection rule" requires that S and M_s must be the same for the initial and final states. In this case $\Delta L = \pm 1, 0$. Also, since the electric dipole operator is an odd function, the initial and final states must have different parity for the integral not to vanish. This is called the "Laporte selection rule."

Transitions that have nonvanishing electric dipole matrix elements are called allowed transitions. All other transitions are called forbidden. Forbidden transitions may occur due to higher order multipole operators. They are much weaker, however, than allowed transitions.

When the ion is in a crystal field environment the multiplicity selection rule is still valid. The Laporte forbidden transitions may become partially allowed, however, through the mixing of orbitals with different parity. Since the transitions observed in ruby involve the rearrangement of the electrons in their d orbitals, they would be Laporte forbidden in the free ion.

The selection rules for transitions between different crystal states can be found from group theory. The representation of the multipole operator in the spherical rotation group is reduced in terms of the representations of the crystal field group. Then, because of the orthogonality of wavefunctions denoted by different representations, the product representation of the operator and the initial state must contain the representation of the final state for the matrix element to be non-zero. The electric dipole operator is represented by D_{1u} in the rotation group and will transform like x , y , or z depending on the direction of polarization. All three of these belong to the T_1 representation of the O_h group.

When a trigonal field is present as in ruby the symmetry group which is relevant to the selection rules is C_{3v} . In this group z belongs to A_1 and x and y belong to E . The product representations of the C_{3v} group and their reduction into irreducible representations are shown in Table 3. For dipole radiation polarized parallel to the c axis, transitions can occur between states whose product representation includes the A_1 irreducible representation. For polarization perpendicular to the c axis, the allowed transitions are those whose product representation contains the E irreducible representation. The results are tabulated in Table 4.

3.2.2 RADIATIONLESS DECAY

Consider first the direct (or single phonon) process. The system then consists of the ion and the lattice vibrations and can be represented by a product state function including an ion part and a phonon part (neglecting the influence of the interaction). Substituting this along with the ion-lattice interaction part of Eq. (64) into

Table 3. C_{3v} Product Representations

C_{3v}	E	\bar{E}	C_3, \bar{C}_3^2	\bar{C}_3, C_3^2	$3\sigma_v$	$3\bar{\sigma}_v$	
A_1	1		1		1		Z
A_2	1		1		-1		
E	2		-1		0		x, y
$E_{1/2}$	2	-2	1	-1	0	0	
$E_{3/2}^+$	1	-1	-1	1	i	-i	
$E_{3/2}^-$	1	-1	-1	1	-i	i	
$A_1 A_1$	1		1		1		A_1
$A_1 A_2$	1		1		-1		A_2
$A_1 E$	2		-1		0		E
$A_1 A_2$	1		1		1		A_1
$A_2 E$	2		-1		0		E
E E	4		1		0		$A_1 + A_2 + E$
$E_{1/2} E_{3/2}^+$	2	2	-1	-1	0	0	E
$E_{1/2} E_{3/2}^-$	2	2	-1	-1	0	0	E
$E_{1/2} E_{1/2}$	4	4	1	1	0	0	$A_1 + A_2 + E$
$E_{3/2}^+ E_{3/2}^+$	1	1	1	1	-1	1	A_2
$E_{3/2}^+ E_{3/2}^-$	1	1	1	1	1	1	A_1
$E_{3/2}^- E_{3/2}^-$	1	1	1	1	-1	-1	A_2

Table 4. C_{3v} Selection Rules

C_{3v}	A_1	A_2	E	$E_{1/2}$	$E_{3/2}^+$	$E_{3/2}^-$
A_1		0	\perp			
A_2	0		\perp			
E	\perp	\perp	$\perp + $			
$E_{1/2}$				$\perp + $	\perp	\perp
$E_{3/2}^+$				\perp	0	
$E_{3/2}^-$				\perp		0

Eq. (66) gives

$$w = \frac{2\pi}{h} \left| \left\langle f \left| V_1 \epsilon + V_2 \epsilon^2 + \dots \right| i \right\rangle \right|^2 \rho(E_f = E_i),$$

where E_f and E_i include both the energy of the ion and of the phonons.

The direct processes are represented by the following diagram:



Only the first term in the expansion of the interaction Hamiltonian contributes to these processes. Thus, the transition probability per unit time for absorption of a phonon of wave vector q can be written as

$$\begin{aligned}
 w &= \frac{2\pi}{h} \left| \left\langle \psi_f \left| i V_1 \sqrt{\frac{\hbar \omega_q}{2 M v^2}} b_q \right| \psi_i \right\rangle \right|^2 \rho(E_f = E_i) \\
 w &= \frac{\pi \omega_q}{M v^2} \left| \left\langle \psi_f^{el} \left| V_1 \right| \psi_i^{el} \right\rangle \right|^2 \left| \left\langle n_q - 1 \left| b_q \right| n_q \right\rangle \right|^2 \rho(E_f = E_i) \\
 w &= \frac{\pi \omega_q}{M v^2} n_q \left| \left\langle \psi_f^{el} \left| V_1 \right| \psi_i^{el} \right\rangle \right|^2 \rho(E_f = E_i). \quad (72)
 \end{aligned}$$

Similarly, for a single phonon emission process

$$w = \frac{\pi \omega_q}{M v^2} (n_q + 1) \left| \langle \psi_f^{el} | V_1 | \psi_i^{el} \rangle \right|^2 \rho(E_f = E_i). \quad (73)$$

The density of final states for these processes is given by

$$\begin{aligned} \rho(E_f = E_i) &= \rho(E_f) \delta(E_f - E_i) dE_f \\ &= \rho(E_f^{el}) \rho(E_f^{phon}) \rho \left[(E_f^{el} + E_f^{phon}) - (E_i^{el} + E_i^{phon}) \right] dE_f^{el} dE_f^{phon} \\ &= \frac{1}{\hbar} g(\omega_{fi}^{el} - \omega_r) \rho(\omega_q) \delta \left[\omega_{fi}^{el} - \omega_q \right] d\omega_{fi}^{el} d\omega_q, \end{aligned} \quad (74)$$

where

$$\omega_{if}^{el} = \frac{E_i^{el} - E_f^{el}}{\hbar}, \quad (75)$$

$$g(\omega_{fi}^{el} - \omega_r) = \text{normalized line shape} \simeq \delta(\omega_{fi}^{el} - \omega_r),$$

ω_r = central frequency of the transition.

In the Debye approximation the density of phonon states is (Kittel, 1956)

$$\begin{aligned} \rho(\omega) &= \frac{3V\omega^2}{2\pi^2 v^3} \quad \text{when } \omega \leq \omega_D, \\ \rho(\omega) &= 0 \quad \text{when } \omega > \omega_D. \end{aligned} \quad (76)$$

The occupation numbers for the phonon states are given by (Orbach, 1962)

$$n_q = \frac{1}{e^{\hbar\omega_q/KT} - 1}. \quad (77)$$

The total transition probability for the emission or absorption of a single phonon can be found by substituting Eqs. (74), (76), and (77) into Eqs. (72) or (73) and integrating over ω_{fi} and ω_q . Because of the delta functions the results can be immediately written as

$$W_{abs} = \left(\frac{3\omega_r^3}{2\pi\rho v^5 \hbar} \right) \left| \langle \psi_f^{el} | V_1 | \psi_i^{el} \rangle \right|^2 n_r. \quad (78)$$

$$W_{em} = \left(\frac{3 \omega_r^3}{2 \pi \rho v^5 \hbar} \right) \left| \langle \psi_f^{el} | V_1 | \psi_i^{el} \rangle \right|^2 (n_r + 1). \quad (79)$$

Equations (78) and (79) depend on temperature only through the phonon occupation numbers n_r which are given by (77). They can be expressed as a constant times a temperature dependent factor.

$$W_{abs} = \sum_{f>i} \beta'_{if} \left[\frac{1}{e^{\hbar\omega_r/KT} - 1} \right], \quad (80)$$

$$W_{em} = \sum_{f<i} \beta'_{if} \left[\frac{e^{\hbar\omega_r/KT}}{e^{\hbar\omega_r/KT} - 1} \right], \quad (81)$$

$$\beta'_{if} = \frac{3 |\omega_r|^3}{2 \pi \rho v^5 \hbar} \left| \langle \psi_f^{el} | V_1 | \psi_i^{el} \rangle \right|^2. \quad (82)$$

If the distance between energy levels is greater than KT_D , radiationless decay can take place only by the emission of more than one phonon. These higher order processes can be treated by higher order perturbation theory. Thus the probability for multiphonon processes to occur decreases as the number of phonons involved increases. The calculation of transition probabilities for multiphonon processes is complicated by the numerous methods of phonon decay connecting two levels, that is, different numbers of phonons may be involved as long as their total energy sums to the energy gap between levels. In general, multiphonon processes give negligible contributions to the thermal dependence of the width and position of sharp fluorescence lines. Some specific two-phonon processes are important, however, and are considered in detail in Section 3.3.

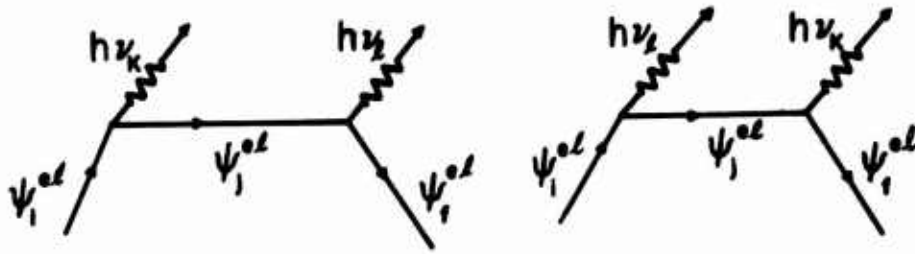
3.2.3 VIBRONIC TRANSITIONS

The fluorescence spectrum of a magnetic ion in a host crystal is characterized by sharp, intense peaks. On both sides of these lines are wide bands displaying a distinct structure of less intense and broader peaks. The former lines are due to purely radiative transitions while the latter are due to phonon assisted transitions called "vibronics." The vibronics on the high energy side of the no-phonon line are assigned to processes involving phonon annihilation. Those on the low energy side correspond to phonon creation transitions. Because of the nature of these transitions the vibronic structure of the spectra exhibits specific characteristics (especially temperature dependence) which makes it possible to identify and study these processes.

Vibronics may also be observed in absorption spectra. In this case the high energy vibronics correspond to the emission of a phonon along with the absorption of a photon while the low energy vibronics are due to the concurrent absorption of a phonon and a photon. This is just the opposite of what is seen in the fluorescence spectra.

Consider the transition in which a photon of frequency ν_l and polarization $\hat{\pi}_l^\lambda$ is created along with a phonon of frequency ν_K . Since the first order operators H_{int}^{IV} and H_{int}^{IE} cannot connect the initial state with the proper final state in a first order treatment, second order perturbation theory must be used.

The Feynman diagrams which represent this second order process are:



Since the intermediate states of the system are virtual states, energy need not be conserved except when considering the entire system before and after the complete transition. The sum over j includes all possible states of the system.

For the low energy emission vibronics, second order perturbation theory gives

$$M = \sum_j \left[\frac{\langle \psi_f^{el}, n_K+1, n_l+1 | H_{int}^{IE} | \psi_j^{el}, n_K+1, n_l \rangle \langle \psi_j^{el}, n_K+1, n_l | H_{int}^{IV} | \psi_i^{el}, n_K, n_l \rangle}{E_i^{el} - (E_j^{el} + h\nu_K)} + \frac{\langle \psi_f^{el}, n_K+1, n_l+1 | H_{int}^{IV} | \psi_j^{el}, n_K, n_l+1 \rangle \langle \psi_j^{el}, n_K, n_l+1 | H_{int}^{IE} | \psi_i^{el}, n_K, n_l \rangle}{E_i^{el} - (E_j^{el} + h\nu_l)} \right]. \quad (83)$$

The only terms in the interaction Hamiltonian for which there are non-zero matrix elements of this form are:

$$M = -i \sqrt{\frac{\hbar \omega_K}{2 M v^2}} \sqrt{\frac{2 \pi \hbar}{\omega_l M}} \left(\frac{e}{m} \right) \sqrt{n_K+1} \sqrt{n_l+1} \times \sum_j \frac{\langle \psi_f^{el} | \Sigma e^{-i \vec{R} \cdot \vec{r}} \vec{p} \cdot \hat{\pi}_l^\lambda | \psi_j^{el} \rangle \langle \psi_j^{el} | V_l | \psi_i^{el} \rangle}{E_i^{el} - (E_j^{el} + h\nu_K)}, \quad (84)$$

where the second term in Eq. (83) is neglected since $\nu_I \gg \nu_K$. Similarly the matrix elements for the high energy emission vibronic transitions (creation of a photon plus absorption of a phonon) have the form:

$$M = i \sqrt{\frac{\hbar \omega_K}{2 M v^2}} \sqrt{\frac{2 \pi \hbar}{\omega_I V}} \left(\frac{e}{m} \right) \sqrt{n_I + 1} \sqrt{n_K} \\ \times \sum_j \frac{\langle \psi_I^{el} | \sum e^{-i \vec{K} \cdot \vec{r}} \vec{p} \cdot \hat{\pi}_I^\lambda | \psi_j^{el} \rangle \langle \psi_j^{el} | V_I | \psi_I^{el} \rangle}{E_I^{el} - (E_j^{el} - \hbar \nu_K)} . \quad (85)$$

The matrix elements given in Eqs. (84) and (85) can be used with the density of final states given in the last section and the Golden Rule to determine the probability for vibronic processes.

Since they involve phonons, vibronic lines will be strongly temperature dependent. At low temperatures there will be fewer phonons available for the ion to absorb. Thus, the intensity of the vibronics on the high energy side of the emission no-phonon line will decrease with temperature and will finally disappear entirely. At higher temperatures there should be a high energy vibronic line corresponding to each low energy line. As temperature is increased, the integrated intensity of the vibronic bands is strengthened relative to the pure electronic transition line. The intensities of the vibronic lines are increased due to the greater perturbation of the phonon field. The wavelength range of the bands is greater because the abundance of phonons in the field allows multiphonon processes to occur.

3.3 Thermal Dependence of the Position, Width, and Shape of Sharp Spectral Lines

Since transitions between electronic states take place at a specific frequency, it would seem that experimental spectroscopic data should appear as vertical straight lines at discrete frequencies. Even under the most ideal conditions, however, where no perturbations are present the spectral lines will have a certain frequency distribution. This is due to the uncertainty principle for time and energy and is called the natural linewidth. Since each excited level has a finite lifetime, it must also have a finite energy width and thus a frequency distribution associated with it. The lifetime of the metastable state in ruby is about three milliseconds. The lifetime broadening should be proportional to $1/\tau_I$. The observed linewidth is much greater than $1/\tau_I$, however, and is temperature dependent. There are several causes of line broadening. They can be divided into two categories, those which produce a Gaussian line shape and those which produce a Lorentzian line shape.

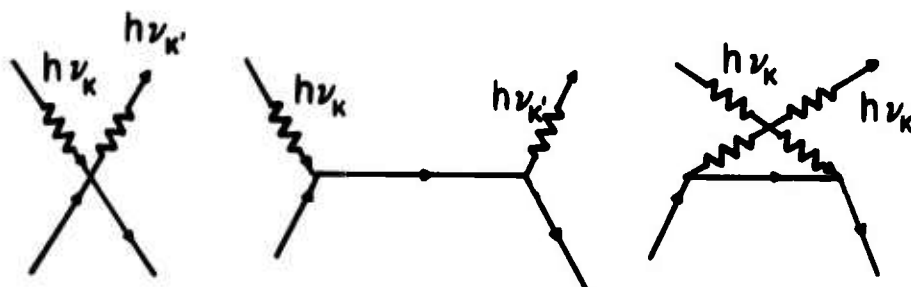
A Gaussian curve is the superposition of a great number of independent events with random probabilities of occurrence. A spectral line is in this case the superposition of a great number of individual lines. Each individual line has a certain frequency distribution and a slightly different central frequency due to the different environments at the instant of the transition. The difference in the local environment is attributed to internal microscopic strains in the crystal which produce a spatially random distribution of the effective crystal field strength at the ion site. A similar effect takes place in gases where the Doppler effect also produces a Gaussian line.

A Lorentzian curve arises from the superposition of a great number of independent events each with the same probability of occurrence. In gases a mechanism which gives a Lorentzian shape is the collision between two atoms. The probability for a specific atom undergoing a collision with another atom is the same for all atoms. This is called collision broadening. The comparable effect in solids is the interaction of the active ion with thermal vibrations of the lattice. Here again the interaction between a single ion and the lattice vibrations is the same for all ions.

The observed spectral line will be broadened simultaneously by Gaussian and Lorentzian processes. The observed line shape will be a superposition of the Gaussian and Lorentzian shapes. Mathematically this is expressed as the convolution of the probability densities for Gaussian and Lorentzian curves and the resulting line shape is called a Voigt profile.

Assuming that the microscopic strains are independent of temperature, the temperature dependent part of the broadening of a spectral line of an ion in a crystal is due to the ion-lattice interaction. The width of a line is the sum of the widths of the initial and final states of the transition. The contribution to the linewidth of a specific type of process is proportional to the probability of occurrence for that process. The probabilities for direct processes have already been derived. One of the most important broadening processes is the two phonon Raman process. The probability for this type of process will now be derived.

Raman scattering is the absorption of a phonon by the active ion and the re-emission of a phonon of a different frequency. The ion changes vibrational states but remains in the same electronic state. Thus, this type of process does not affect the lifetime of the state. The Feynman diagrams for this process are given by:



Writing the first order ion-lattice interaction Hamiltonian as H' and the second order ion-lattice interaction Hamiltonian as H'' the matrix element for Raman scattering is

$$\begin{aligned}
 \langle f | H_{\text{Raman}} | i \rangle &= \langle \psi_i^{\text{el}}; n_{K'}-1, n_{K'}+1 | H_{\text{Raman}} | \psi_i^{\text{el}}; n_{K'}, n_{K'} \rangle \\
 &= \sum_j \left[\frac{\langle \psi_j^{\text{el}}; n_{K'}-1, n_{K'}+1 | H' | \psi_j^{\text{el}}; n_{K'}-1, n_{K'} \rangle \langle \psi_i^{\text{el}}; n_{K'}-1, n_{K'} | H' | \psi_i^{\text{el}}; n_{K'}, n_{K'} \rangle}{E_i^{\text{el}} - (E_j^{\text{el}} - \hbar \omega_{K'})} \right. \\
 &\quad \left. + \frac{\langle \psi_i^{\text{el}}; n_{K'}-1, n_{K'}+1 | H' | \psi_j^{\text{el}}; n_{K'}, n_{K'}+1 \rangle \langle \psi_j^{\text{el}}; n_{K'}, n_{K'}+1 | H' | \psi_i^{\text{el}}; n_{K'}, n_{K'} \rangle}{E_i^{\text{el}} - (E_j^{\text{el}} + \hbar \omega_{K'})} \right] \\
 &\quad + \langle \psi_i^{\text{el}}; n_{K'}-1, n_{K'}+1 | H'' | \psi_i^{\text{el}}; n_{K'}, n_{K'} \rangle . \\
 \langle f | H_{\text{Raman}} | i \rangle &= \frac{\hbar}{2 M v^2} \sqrt{\omega_K \omega_{K'}} \left\{ \sum_j \left[\frac{|\langle \psi_i^{\text{el}} | v_1 | \psi_j^{\text{el}} \rangle|^2}{E_i^{\text{el}} - (E_j^{\text{el}} - \hbar \omega_K)} \langle n_{K'}-1, n_{K'}+1 | b_K^+ b_K | n_{K'}, n_{K'} \rangle \right. \right. \\
 &\quad \left. + \frac{|\langle \psi_i^{\text{el}} | v_1 | \psi_j^{\text{el}} \rangle|^2}{E_i^{\text{el}} - (E_j^{\text{el}} + \hbar \omega_{K'})} \langle n_{K'}-1, n_{K'}+1 | b_K b_K^+ | n_{K'}, n_{K'} \rangle \right] \\
 &\quad \left. + \langle \psi_i^{\text{el}} | v_2 | \psi_i^{\text{el}} \rangle \langle n_{K'}-1, n_{K'}+1 | 2 b_K b_K^+ | n_{K'}, n_{K'} \rangle \right\} \\
 &\approx \frac{\hbar}{M v^2} \sqrt{\omega_K \omega_{K'} n_K (n_{K'}+1)} \left[\sum_{j \neq i} \frac{|\langle \psi_i^{\text{el}} | v_1 | \psi_j^{\text{el}} \rangle|^2}{E_i^{\text{el}} - E_j^{\text{el}}} + \langle \psi_i^{\text{el}} | v_2 | \psi_i^{\text{el}} \rangle \right]. \tag{86}
 \end{aligned}$$

This can be written as

$$\langle f | H_{\text{Raman}} | i \rangle = \alpha' \sqrt{\omega_K \omega_{K'} n_K (n_{K'}+1)} \tag{87}$$

where

$$\alpha' = \frac{\hbar}{M v^2} \left[\sum_{j \neq i} \frac{|\langle \psi_i^{\text{el}} | v_1 | \psi_j^{\text{el}} \rangle|^2}{E_i^{\text{el}} - E_j^{\text{el}}} + \langle \psi_i^{\text{el}} | v_2 | \psi_i^{\text{el}} \rangle \right]. \tag{88}$$

The probability per unit time of a Raman scattering process is given by the Golden Rule in Eq. (66) with the matrix element of Eq. (87) and the density of final states for sharp lines given by

$$\rho(\omega_f) = \rho(\omega_K) \rho(\omega_{K'}) \delta(\omega_K - \omega_{K'}) d\omega_K d\omega_{K'} . \quad (89)$$

Integrating over $\omega_{K'}$ and $\omega_{K'}$ gives the probability per unit time for all Raman processes.

$$\begin{aligned} W &= \frac{2\pi}{\hbar^2} \iint |\langle i | H_{\text{Raman}} | f \rangle|^2 \rho(\omega_K) \rho(\omega_{K'}) \delta(\omega_K - \omega_{K'}) d\omega_K d\omega_{K'} \\ &= \frac{2\pi}{\hbar^2} |\alpha'|^2 \int_0^{\omega_D} [\rho(\omega_K)]^2 \omega_K^2 n_K (n_K + 1) d\omega_K . \end{aligned}$$

Using Eqs. (76) and (77) this becomes

$$\begin{aligned} W &= \frac{2\pi}{\hbar^2} |\alpha'|^2 \frac{3V^2}{4\pi^4 v^6} \int_0^{\omega_D} \frac{\omega_K^6 e^{\hbar\omega_K/KT}}{e^{\hbar\omega_K/KT} - 1} d\omega_K \\ W &= \frac{9V^2}{2\pi^3 \hbar^2 v^6} |\alpha'|^2 \left(\frac{KT_D}{\hbar}\right)^7 \left(\frac{T}{T_D}\right)^7 \int_0^{T_D/T} \frac{x^6 e^x}{(e^x - 1)^2} dx . \end{aligned}$$

So the contribution to the linewidth due to the Raman scattering of phonons is

$$\Delta \tilde{\nu}(\text{cm}^{-1}) = \bar{\alpha} \left(\frac{T}{T_D}\right)^7 \int_0^{T_D/T} \frac{x^6 e^x}{(e^x - 1)^2} dx , \quad (90)$$

where

$$\bar{\alpha} = (3.34 \times 10^{-11}) \frac{9}{2\pi^3 \rho^2 v^{10}} \left(\frac{KT_D}{\hbar} \right)^7 \times \left[\sum_{j \neq i} \frac{|\langle \psi_i^{el} | V_1 | \psi_j^{el} \rangle|^2}{E_i^{el} - E_j^{el}} + \langle \psi_i^{el} | V_2 | \psi_i^{el} \rangle \right]^2. \quad (91)$$

Since $\bar{\alpha}$ is intrinsically positive an increase in temperature will cause an increase in linewidth.

Along with Raman scattering processes which leave the ion in the same electronic state we can also have Raman relaxation and Raman excitation processes. In these processes phonons of different frequencies are absorbed and emitted and the intermediate state is a virtual state as in Raman scattering. In Raman excitation or relaxation processes, however, the initial and final electronic states are different. The energy splitting of these states is equal to the difference in energy of the absorbed and emitted phonons. Mathematically these cases can be treated similarly to Raman scattering. The temperature dependent (phonon) part will be exactly the same as that given in Eq. (90). The only difference will be in the matrix elements of the crystal field operator between electronic states. This changes $\bar{\alpha}$. In considering experimentally observed linewidths, however, $\bar{\alpha}$ is treated as an adjustable parameter. Thus, Eq. (90) can be used in determining the linewidth contribution of all the Raman processes. It should be noted that Raman excitation and relaxation processes will contribute to the lifetime of the level whereas Raman scattering processes will not.

In certain cases it is possible to have two phonon relaxation and excitation processes which have as their intermediate state a real electronic level. These are called Orbach processes. Since these processes involve a real transition between the level under consideration and another real level, they are taken into account when all the direct processes are considered.

Thus, the width of a spectral line is given by

$$\Delta \tilde{\nu}(\text{cm}^{-1}) = \Delta \tilde{\nu}_0 + \bar{\alpha} \left(\frac{T}{T_D} \right)^7 \int_0^{T_D/T} \frac{x^6 e^x}{(e^x - 1)^2} dx + \sum_{f>i} \beta_{if} \left[\frac{1}{e^{\hbar\omega_{fi}/KT} - 1} \right] + \sum_{f<i} \beta_{if} \left[\frac{e^{\hbar\omega_{if}/KT}}{e^{\hbar\omega_{if}/KT} - 1} \right], \quad (92)$$

where $\bar{\alpha}$ is given by Eq. (91), $\beta_{if} = (3.34 \times 10^{-11}) \beta'_{if}$ which is given by Eq. (82) and $\Delta \tilde{\nu}_0$ is the temperature-independent contribution due to microscopic strains. In this expression the linewidths of Gaussian and Lorentzian broadening processes have simply been added. Although this is not exactly correct, Eq. (92) does give an accurate description of the thermal dependence of linewidths.

Finally, let us consider the thermal shift of a spectral line. This is due to the continual absorption and re-emission of virtual phonons by the impurity ion in the phonon field. Using the first two terms in the expansion of the ion-phonon interaction Hamiltonian given in Eq. (64), the energy due to ion-phonon interaction for the i th state of the system is:

$$\delta \tilde{\nu}_i = \langle i | H'' | i \rangle + \sum_{j \neq i} \frac{|\langle j | H' | i \rangle|^2}{E_i - E_j}. \quad (93)$$

Since n_i depends on temperature, $\delta \tilde{\nu}$ is temperature dependent. This thermal dependence of the interaction energy is the cause of the shift of spectral lines with temperature.

We can evaluate $\delta \tilde{\nu}_i$ as follows:

$$\begin{aligned} \delta \tilde{\nu}_i &= \sum_j \frac{\langle i | H' | j \rangle \langle j | H' | i \rangle}{E_i - E_j} + \langle i | H'' | i \rangle \\ &= - \frac{\hbar}{2 M v^2} \left\{ \sum_{jK} \left[\frac{\langle \psi_i^{el}; n_K | V_1 \sum_l \sqrt{\omega_l} (b_l - b_l^\dagger) | \psi_j^{el}; n_{K+1} \rangle}{E_i^{el} - (E_j^{el} + \hbar \omega_K)} \right. \right. \\ &\quad \times \frac{\langle \psi_j^{el}; n_{K+1} | V_1 \sum_{l'} \sqrt{\omega_{l'}} (b_{l'} - b_{l'}^\dagger) | \psi_i^{el}; n_K \rangle}{E_i^{el} - (E_j^{el} + \hbar \omega_K)} \\ &\quad \left. \left. + \frac{\langle \psi_i^{el}; n_K | V_1 \sum_l \sqrt{\omega_l} (b_l - b_l^\dagger) | \psi_j^{el}; n_{K-1} \rangle \langle \psi_j^{el}; n_{K-1} | V_1 \sum_{l'} \sqrt{\omega_{l'}} (b_{l'} - b_{l'}^\dagger) | \psi_i^{el}; n_K \rangle}{E_i^{el} - (E_j^{el} - \hbar \omega_K)} \right] \right. \\ &\quad \left. + \langle \psi_i^{el}; n_K | V_2 \sum_{l,l'} \sqrt{\omega_l \omega_{l'}} (b_l - b_l^\dagger) (b_{l'} - b_{l'}^\dagger) | \psi_i^{el}; n_K \rangle \right\} \end{aligned}$$

$$\begin{aligned}
\delta \tilde{\nu}_1 &= \frac{\hbar}{2 M v^2} \left\{ \sum_{jK} \omega_K \left[\frac{\langle \psi_i^{el} | V_1 | \psi_j^{el} \rangle \langle \psi_j^{el} | V_1 | \psi_i^{el} \rangle}{E_i^{el} - (E_j^{el} + \hbar \omega_K)} \langle n_K | b_K b_K^\dagger | n_K \rangle \right. \right. \\
&\quad \left. \left. + \frac{\langle \psi_i^{el} | V_1 | \psi_j^{el} \rangle \langle \psi_j^{el} | V_1 | \psi_i^{el} \rangle}{E_i^{el} - (E_j^{el} - \hbar \omega_K)} \langle n_K | b_K^\dagger b_K | n_K \rangle \right] \right. \\
&\quad \left. + \sum_K \omega_K \langle \psi_i^{el} | V_2 | \psi_i^{el} \rangle \langle n_K | b_K b_K^\dagger + b_K^\dagger b_K | n_K \rangle \right\} \\
&= \frac{\hbar}{2 M v^2} \left\{ \sum_{jK} \omega_K |\langle \psi_i^{el} | V_1 | \psi_j^{el} \rangle|^2 \right. \\
&\quad \times \left[\frac{n_K + 1}{E_i^{el} - (E_j^{el} + \hbar \omega_K)} + \frac{n_K}{E_i^{el} - (E_j^{el} - \hbar \omega_K)} \right] \\
&\quad \left. + \sum_K \omega_K \langle \psi_i^{el} | V_2 | \psi_i^{el} \rangle (1 + 2 n_K) \right\}. \tag{94}
\end{aligned}$$

Even when n_K is zero δE_i is not zero. This temperature independent zero field shift is similar to the Lamb shift produced in atomic systems by an electromagnetic field. It is given by

$$\delta \tilde{\nu}_1^0 = \frac{\hbar}{M v^2} \left\{ \sum_{jK} \frac{\omega_K |\langle \psi_i^{el} | V_1 | \psi_j^{el} \rangle|^2}{E_i^{el} - (E_j^{el} + \hbar \omega_K)} + \sum_K \omega_K \langle \psi_i^{el} | V_2 | \psi_i^{el} \rangle \right\}. \tag{95}$$

Disregarding this contribution the temperature dependent shift is given by

$$\begin{aligned}
\delta \tilde{\nu}_1 &= \frac{\hbar}{2 M v^2} \left\{ \sum_{j=i} |\langle \psi_i^{el} | V_1 | \psi_i^{el} \rangle|^2 \right. \\
&\quad \times \sum_K n_K \omega_K \left[\frac{1}{E_i^{el} - E_j^{el} - \hbar \omega_K} + \frac{1}{E_i^{el} - E_j^{el} + \hbar \omega_K} \right] \left. \right\}. \tag{96}
\end{aligned}$$

First consider the case where $|E_i^{el} - E_j^{el}| \gg \hbar \omega_D$.

$$\begin{aligned}
\delta \tilde{\nu}_1 &\approx \frac{\hbar}{M v^2} \sum_K \omega_K n_K \left[\sum_{j=1} \frac{|\langle \psi_i^{el} | V_1 | \psi_j^{el} \rangle|^2}{E_i^{el} - E_j^{el}} \right. \\
&\quad \left. + \langle \psi_i^{el} | V_2 | \psi_i^{el} \rangle \right] \\
&= \alpha' \sum_K n_K \omega_K,
\end{aligned} \tag{97}$$

where:

$$\alpha' = \frac{\hbar}{M v^2} \left[\sum_{j \neq i} \frac{|\langle \psi_i^{el} | V_1 | \psi_j^{el} \rangle|^2}{E_i^{el} - E_j^{el}} + \langle \psi_i^{el} | V_2 | \psi_i^{el} \rangle \right]. \tag{98}$$

The sum over K can be changed to an integral as follows:

$$\begin{aligned}
\sum_K n_K \omega_K &\rightarrow \int_0^{\omega_D} \frac{\rho(\omega_K) \omega_K}{e^{\hbar \omega_K / KT} - 1} d\omega_K \\
&= \frac{3V}{2\pi^2 v^3} \int_0^{\omega_D} \frac{\omega_K^3}{e^{\hbar \omega_K / KT} - 1} d\omega_K = \frac{3V}{2\pi^2 v^2} \left(\frac{KT}{h} \right)^4 \int_0^{T_D/T} \frac{x^3}{e^x - 1} dx. \tag{99}
\end{aligned}$$

Thus, the temperature dependent lineshift is given by

$$\delta \tilde{\nu} (\text{cm}^{-1}) = \alpha \left(\frac{T}{T_D} \right)^4 \int_0^{T_D/T} \frac{x^3}{e^x - 1} dx, \tag{100}$$

where

$$\alpha = (5.03 \times 10^{15}) \frac{3\hbar}{2\pi^2 \rho v^5} \left(\frac{KT_D}{h} \right)^4 \left[\sum_{j=1} \frac{|\langle \psi_i^{el} | V_1 | \psi_j^{el} \rangle|^2}{E_i^{el} - E_j^{el}} + \langle \psi_i^{el} | V_2 | \psi_i^{el} \rangle \right] \tag{101}$$

For this case α can be either positive or negative depending on $E_i^{el} - E_j^{el}$.

Now consider the case when $|E_i^{el} - E_j^{el}| \lesssim \omega_D$. For this case

$$\begin{aligned}
 \delta \tilde{\nu}(\text{cm}^{-1}) &= \frac{\hbar}{2 M v^2} \sum_{j \neq i} |\langle \psi_i^{el} | V_1 | \psi_j^{el} \rangle|^2 \int \rho(\omega_K) n_K \omega_K \frac{2(E_i^{el} - E_j^{el})}{(E_i^{el} - E_j^{el})^2 - (\hbar \omega_K)^2} d\omega_K \\
 &= \sum_{j \neq i} \frac{\hbar}{M v^2} \frac{3V}{2\pi^2 v^2} |\langle \psi_i^{el} | V_1 | \psi_j^{el} \rangle|^2 \frac{(E_i^{el} - E_j^{el})^3}{(E_i^{el} - E_j^{el})^2} \\
 &\quad \times \left(\frac{KT}{\hbar}\right)^4 \frac{1}{(KT)^2} P \int_0^{T_D/T} \frac{x^3}{e^x - 1} \frac{1}{x^2 - (\Delta E_{ij}/KT)^2} dx \\
 &= \sum_{j < i} \beta_{ij}'' \left(\frac{T}{\Delta E_{ij}}\right)^2 P \int_0^{T_D/T} \frac{x^3}{e^x - 1} \frac{1}{x^2 - (\Delta E_{ij}/KT)^2} dx \\
 &\quad - \sum_{j > i} \beta_{ij}'' \left(\frac{T}{\Delta E_{ij}}\right)^2 P \int_0^{T_D/T} \frac{x^3}{e^x - 1} \frac{1}{x^2 - (\Delta E_{ij}/KT)^2} dx, \quad (102)
 \end{aligned}$$

where

$$\beta_{ij}'' = (3.34 \times 10^{-11}) \frac{3|\omega_{ij}|^3}{2\pi^2 \rho v^5} |\langle \psi_i^{el} | V_1 | \psi_j^{el} \rangle|^2 \quad (103)$$

and the pole in the integrand is accounted for by taking the principal value of the integral denoted by P (Louisell, 1964).

Thus, for the total thermal lineshift we find

$$\begin{aligned}
 \delta \tilde{\nu}(\text{cm}^{-1}) &= \alpha \left(\frac{T}{T_D}\right)^4 \int_0^{T_D/T} \frac{x^3}{e^x - 1} dx \\
 &\quad + \sum_{j < i} \beta_{ij}'' \left(\frac{T}{\Delta E_{ij}}\right)^2 P \int_0^{T_D/T} \frac{x^3}{e^x - 1} \frac{1}{x^2 - (\Delta E_{ij}/KT)^2} dx
 \end{aligned}$$

$$- \sum_{j>i} \beta_{ij}'' \left(\frac{T}{\Delta E_{ij}} \right)^2 P \int_0^{T_D/T} \frac{x^3}{e^x - 1} \frac{1}{x^2 - \left(\Delta E_{ij}/KT \right)^2} dx, \quad (104)$$

where α and β_{ij}'' are given by Eqs. (101) and (103), respectively.

4. EXPERIMENTAL APPARATUS AND SAMPLES

4.1 Samples

Six Verneuil grown ruby samples of various concentrations and dimensions were used in the experiments discussed in the following sections. They are listed in Table 5.

Table 5. List of Samples

Sample	Concentration Cr ³⁺ (Atomic %)	Method Concentration Determined	Dimensions (mm)
1	0.03	Absorption data (Dodd, 1964)	9.45 × 7.34 × 3.759
2	0.94	Absorption data (Dodd, 1964)	10.73 × 10.8 × 0.965
3*	2.1	X-ray diffraction**	12.65 × 7.49 × 4.26
4	2.1	(Same boule as No. 3)	10.48 × 6.52 × 0.838
5	2.1	(Same boule as No. 3)	3.25 × 4.445 × 9.525
6	2.1	(Same boule as No. 3)	4.064 × 4.978 × 9.525

* Spectroscopic analysis of this boule by Jarrell-Ash Company indicated that no impurity other than chromium was present in concentrations greater than 0.01%. The chromium concentration was estimated by this technique to be 3.05%.

** This analysis was made by Dr. A. Linz of the M.I.T. Crystal Physics Laboratory. The lattice parameters a and c were measured and the percent of chromium determined from tables compiled by Professor R. Newnham of M.I.T.

4.2 Absorption Apparatus

The apparatus used to obtain the absorption spectra was a Cary Model 14 recording spectrophotometer. The samples were mounted on the cold finger of a liquid nitrogen cryostat. Measurements were made at room temperature and 77°K. The radiation was polarized by using Glan prisms. In the optical region a 650-watt Sylvania DWY Sun Gun was used as a source and a 1-P28 photomultiplier tube as a detector. In the ultraviolet region, from 3500 Å down to 2500 Å, the source was

changed to a hydrogen lamp. The infrared region was also run using a lead sulfide cell as a detector.

4.3 Continuous Fluorescence Apparatus

A block diagram of the continuous fluorescence apparatus is shown in Figure 3. The monochromator shown between the source and the sample is used only for excitation experiments. In the normal arrangement for studying continuous fluorescence the samples were illuminated with white light from an air-cooled General Electric BH6 1000-watt high pressure mercury lamp. The energy emitted by this source was passed through 4 cm of saturated CuSO_4 to filter out the infrared radiation and reduce the heating of the sample. It was then focused on the sample by a two lens condenser.

For measurements at room temperature and below, the samples were mounted in a Janis Model 8DT cryostat. The sample temperature could be varied from 4.2°K up to 300°K by using an exchange gas technique. For obtaining temperatures above 300°K the samples were mounted in a quartz furnace; the temperature was regulated by varying the amount of current in a Ni-Cr ribbon wound around the furnace. In both cases the temperature was monitored by thermocouples and measured with a Leeds and Northrup 8690 millivolt potentiometer. Copper constantan thermocouples were used below room temperature, iron constantan above room temperature.

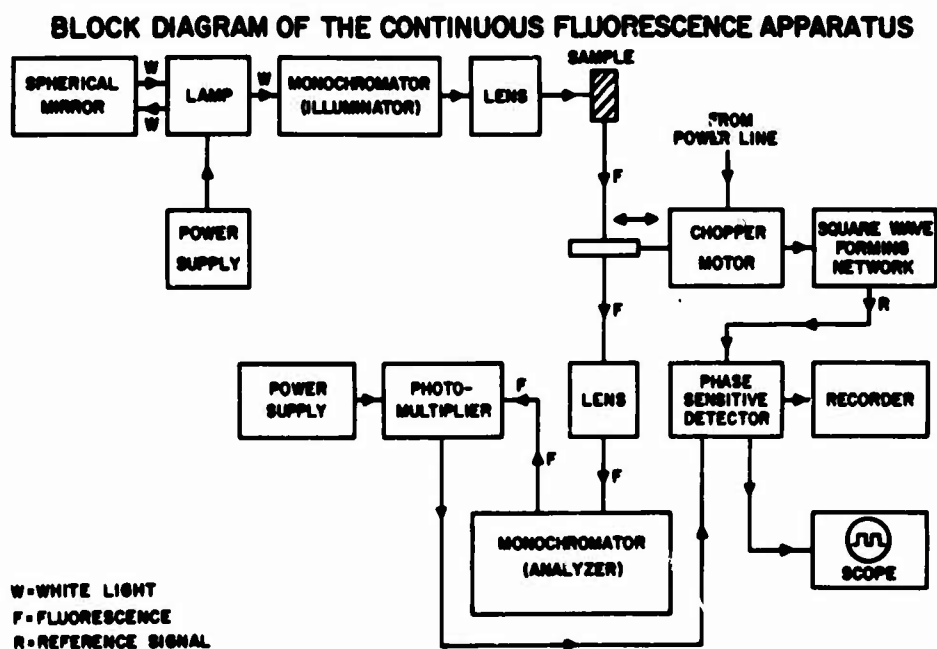


Figure 3. Block Diagram of the Continuous Fluorescence Apparatus

The fluorescence emission from the samples was observed at 90° from the direction of the incident radiation. It was chopped at 20 Hz and then focused onto the entrance slit of a McPherson Model 213 one-meter scanning monochromator. This was a Czerny-Turner (1930) type monochromator with the optical arrangement shown in Figure 4. The grating used was a Bausch and Lomb type 35-53-15-36 blazed at 7500 \AA with a ruling of 1200 lines/mm. A slit width of ten microns gave a resolution of 0.15 \AA in first order of the grating and 0.07 \AA in second order. These resolutions are about twice the theoretical resolution in first order and two and one half times the theoretical second order resolution for a one-meter Czerny-Turner instrument with this grating.

The signal was detected by an RCA 7102 (S-1) photomultiplier tube which was cooled by liquid nitrogen. The modulated signal was then amplified by a P.A.R. JB-5 lock-in amplifier tuned to the reference signal from the chopper. The resulting spectrum was displayed on a Leeds and Northrup speedomax W strip chart recorder.

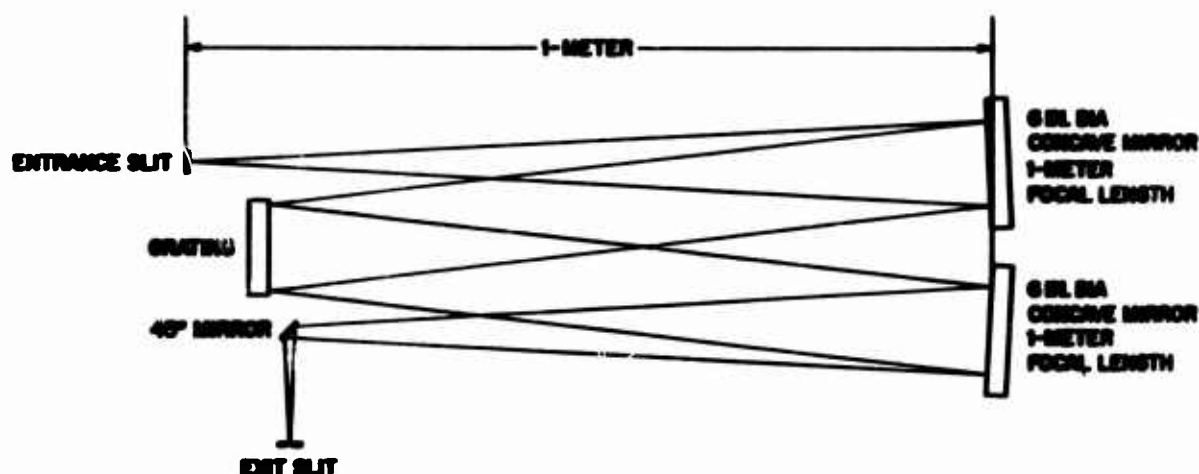


Figure 4. Monochromator Optics

4.4 Apparatus for Excitation Experiments

The experimental arrangement used for the excitation experiments was essentially the same as that shown in Figure 3 for the continuous fluorescence experiments. There were two differences, however. The lamp used in these experiments was a Sylvania DWY 650W Sun Gun. Also a monochromator was placed between the source and the sample to provide selective excitation of variable frequency. This monochromator was an Engis 505-02 with a Bausch and Lomb 35-53-08-01 grating

which has a ruling of 600 lines/mm blazed at 3000 Å. A slit width of 1 mm corresponded to a resolution of 55 Å.

4.5 Pulse Fluorescence Apparatus

A block diagram of the pulse fluorescence apparatus is shown in Figure 5. Again, in the normal arrangement the monochromator shown between the source and the sample is not used. The sample mount and temperature control system, the monochromator, and the photomultiplier are all the same as those used for the continuous fluorescence experiments. The source of excitation and the method of monitoring the detected signal are, however, different. The source used was an EG&G flashtube, either an FX-12 or an FX-33, with various capacitors needed to obtain different pulse lengths. The fluorescence decay was displayed on a Tektronix Type 531 oscilloscope and photographed with a Polaroid camera. The same apparatus could be used for selective excitation experiments by placing the Engis monochromator between the source and the sample to provide an excitation of varying frequency.

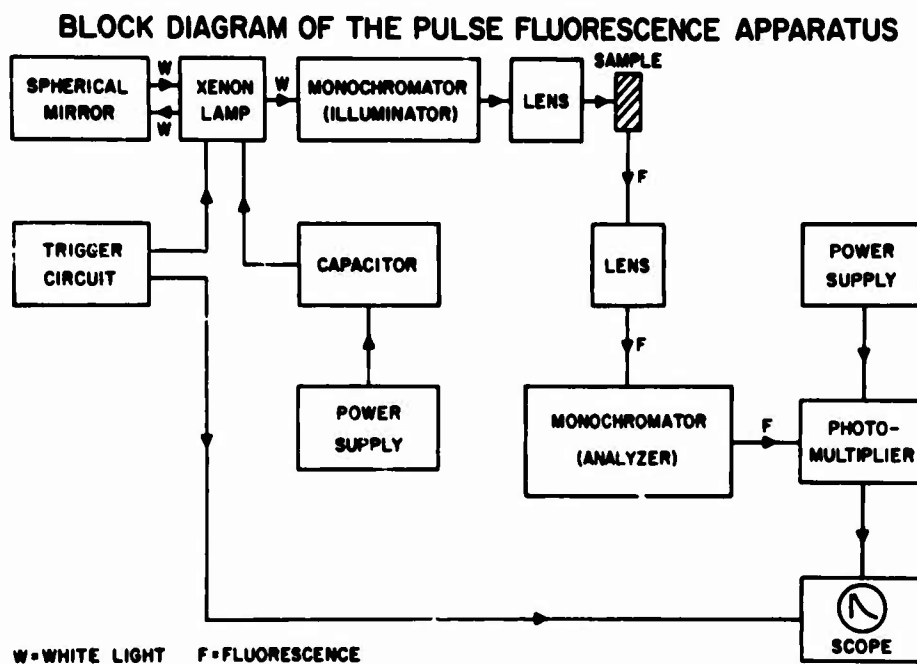


Figure 5. Block Diagram of the Pulsed Fluorescence Apparatus

5. RESULTS AND DISCUSSION OF ABSORPTION EXPERIMENTS

Absorption experiments were performed on three ruby samples, a 0.03% sample of 3.759-mm thickness (listed as No. 1 in Table 5), a 2.1% sample of 4.26-mm thickness (listed as No. 3 in Table 5), and a 2.1% sample of 0.838-mm thickness (listed as No. 4 in Table 5). These measurements were made with both parallel and perpendicular polarizations at both room temperature and liquid nitrogen temperature. The equipment used for these experiments was the absorption apparatus described in Section 4.2. During these experiments the slit width varied from about 0.02 to 0.7 mm. This corresponds to a resolution of 0.74 Å to 17.5 Å.

5.1 Absorption Spectrum of Lightly Doped Ruby

The results of the absorption experiments made on the lightly doped sample at the two temperatures are shown in Figures 6 and 7. The spectrum consists of two broad intense bands and three sets of sharp lines. As the temperature is lowered from 295°K to 77°K the bands and lines all become narrower and more intense at the peaks. They also shift slightly in position toward lower wavelengths. The integrated intensity of the bands remains approximately constant as the temperature is changed.

The most prominent features of the spectra are the two large absorption bands located near 4000 Å and 5500 Å. These are due to spin allowed transitions from the 4A_2 ground state to the 4T_1 and 4T_2 bands respectively (see Figure 2). The differences in intensity in the two polarizations are due to the different selection rules (see Table 4). The structure on the 5500 Å band at 77°K has been attributed to vibronic transitions (McClure, 1959).

The three sets of sharp lines appearing in the absorption spectra are all due to spin forbidden transitions occurring within the ground state configuration (t_2^3). The first set consists of the two R lines occurring near 6950 Å. They arise from transitions originating in the ground state and terminating on the two components of the 2E level split by 29 cm^{-1} due to spin-orbit interaction and the trigonal field.

The second set of lines is found near 6600 Å. They are less intense and broader than the R lines. These three S lines represent transitions from the ground state to the split 2T_1 level. Their greater width may be due to the fact that they are close enough to the lower 2E level for direct decay processes to occur. These lines have been studied by Low (1960) and Margerie (1962).

The third set of lines appears between the two bands at approximately 4750 Å. They are designated as B lines and are due to transitions from the ground state to the three components of the split 2T_2 state. These lines have been studied by several people (Sugano and Tsujikawa, 1958; Low, 1960; Cohen and Bloembergen, 1964).

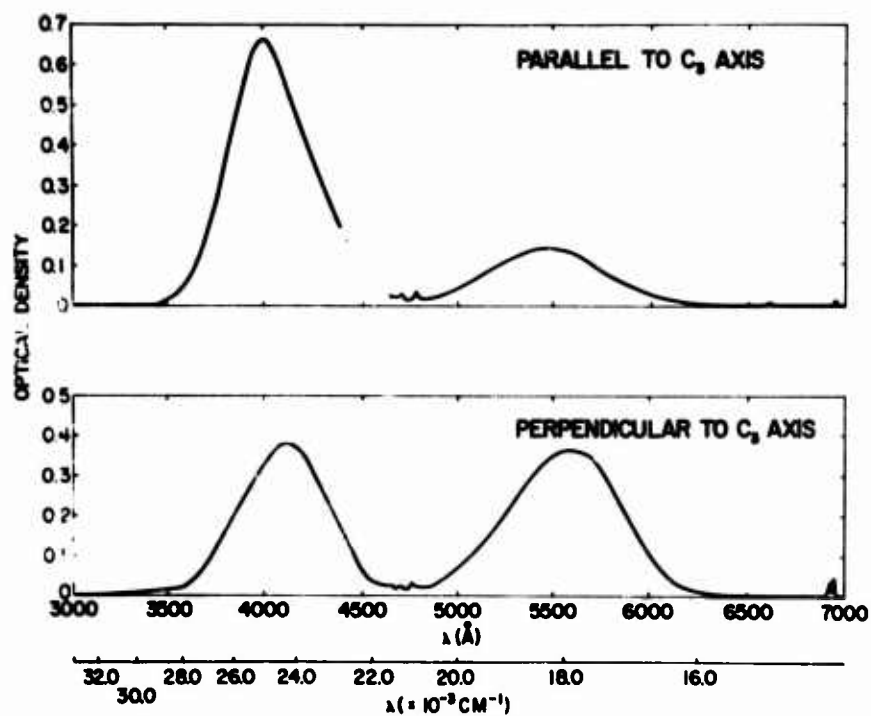


Figure 6. Absorption Spectra of Ruby with 0.03% Chromium at 295°K

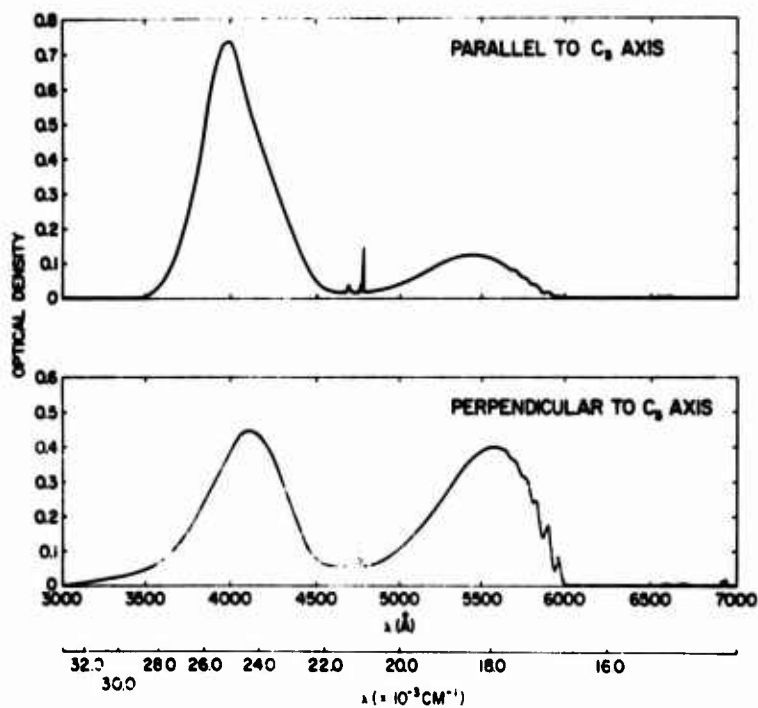


Figure 7. Absorption Spectra of Ruby with 0.03% Chromium at 77°K

The differences in intensities of the various lines in the two polarizations are due to the different selection rules as was the case with the bands. Comparison of the parallel and perpendicular spectra with the axial spectra shows the transitions to be electric dipole in nature (McClure, 1962). In the observed spectra the ground state splitting (0.38 cm^{-1}) was not resolved in any of the lines.

5.2 Absorption Spectrum of Heavily Doped Ruby

The absorption spectra obtained at room temperature and at 77°K are shown in Figures 8 and 9, respectively, for the thin 2.1% ruby (sample No. 4). The general features of the absorption spectrum of lightly doped ruby discussed in the last section are also observed in the absorption spectrum of heavily doped ruby. There is, however, a set of lines and a band that appear in the absorption spectrum of concentrated ruby that do not appear in the spectrum of lightly doped ruby. They have both been found to vary quadratically with Cr^{+3} concentration and, therefore, have been attributed to pair effects. The pair band is located around 3400 \AA and was first studied by Linz and Newnham (1961) and Naiman and Linz (1963).

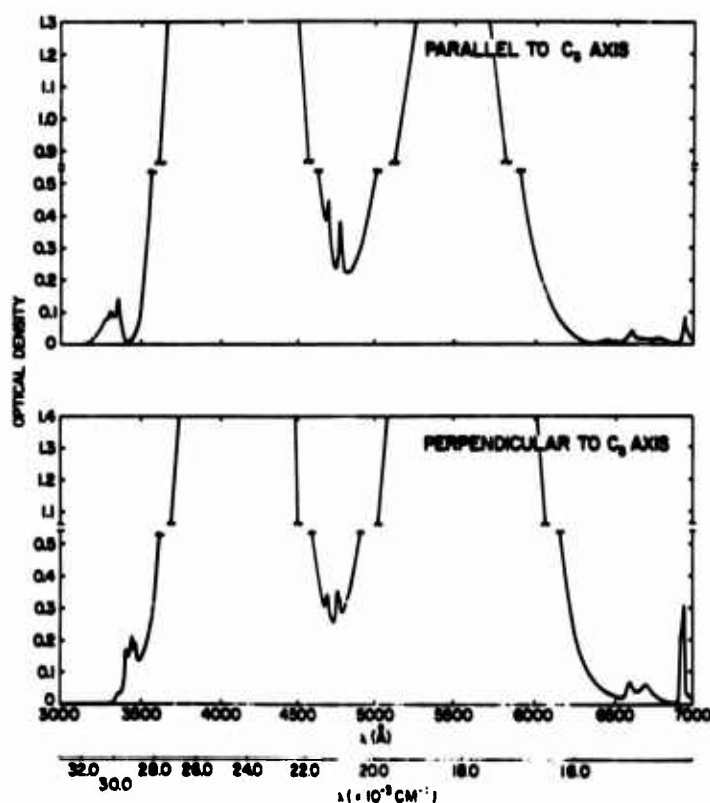


Figure 8. Absorption Spectra of Ruby (0.84 mm) with 2.1% Chromium at 295°K

The new lines are the N lines and the other pair lines seen at about 7000 Å. Also for the more heavily doped sample the intensities of all the lines and bands are larger due to the increase in Cr^{+3} ions. Because of this the structure of the four sets of lines (R, S, B, and N) can be better determined.

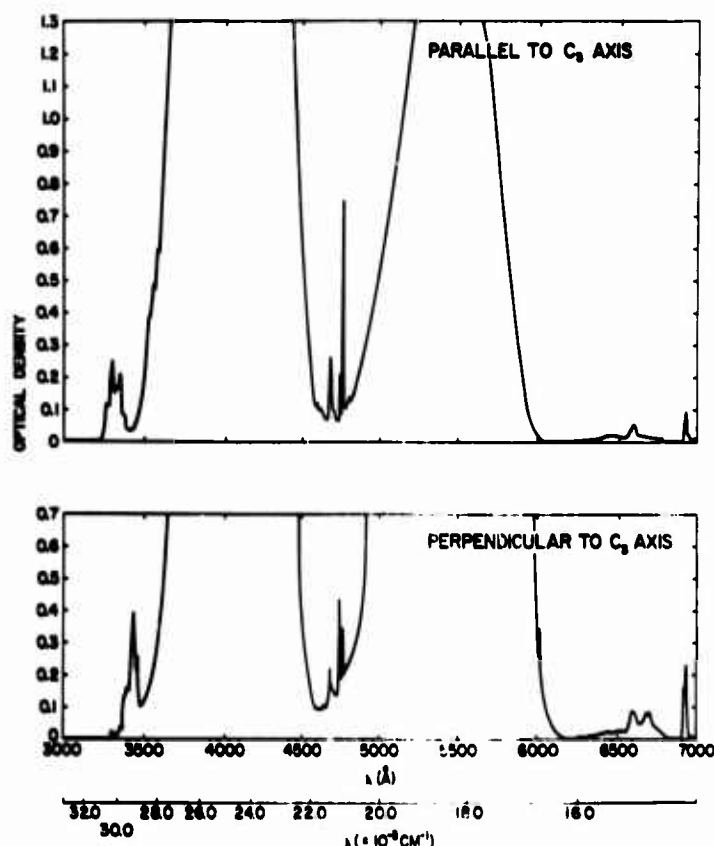


Figure 9. Absorption Spectra of Ruby (0.84 mm) with 2.1% Chromium at 77°K

Figure 10 shows the region of the spectrum consisting of the S, R, and pair lines at 295°K for the thick 2.1% ruby (sample No. 3). The R lines and the pair lines of the same sample at 77°K are shown in Figure 11. The spectrum in this region is observed to be extremely complex with lines appearing on both sides of the R lines and between the R_1 and R_2 lines. The lines on the low energy side of the R lines with wavelength greater than 6948 Å have been associated with pairs of Cr^{+3} ions by their quadratic dependence on concentration (Schawlow et al., 1959). The other lines on both sides and in between the R lines are probably also pair lines (see Section 9.1 and Daly, 1961). The weak line near 7065 Å is probably due

to a vibronic transition of the R_1 line (Kushida). Note that the N_1 line depends strongly on polarization while the N_2 line has very little polarization dependence. These absorption lines which can be identified in fluorescence are marked with an asterisk in Table 9.

Figure 12 shows the S lines of the thick 2.1% sample at liquid nitrogen temperature. The S_3 line has been assigned to transitions from the ground state to the two upper components of the split ${}^2T_1(t_2^3)$ levels and thus consists of two unresolved lines (Margerie, 1962). The S_2 line has been assigned to the transition terminating on the lowest component of the ${}^2T_1(t_2^3)$ level. The lines designated as S_0 and S_1 have been associated with high energy vibronic transitions of the R_1 line (Kushida). The other observed structure in the spectra may be due to the vibronics of the 2T_1 levels. Table 6 lists the absorption lines seen in this region of the spectrum.

The region of the spectrum in the vicinity of the B lines at 77°K is shown in Figures 13 and 14. The former shows the results obtained on the thin 2.1% sample (No. 4) with parallel polarization. The latter figure gives the results obtained for the thick 2.1% sample (No. 3) with both polarizations. The three B lines have been assigned to transitions terminating on the three split components of the ${}^2T_2(t_2^3)$ level (Sugano and Peter, 1961). The other lines observed in this region may be vibronics of the 2T_2 level. They are listed in Table 7. It should also be mentioned that the unassigned lines appearing near the B and S lines, in samples with this high concentration, may be due to transitions terminating on excited levels of the pair systems. A verification of this would require more measurements on samples with several concentrations.

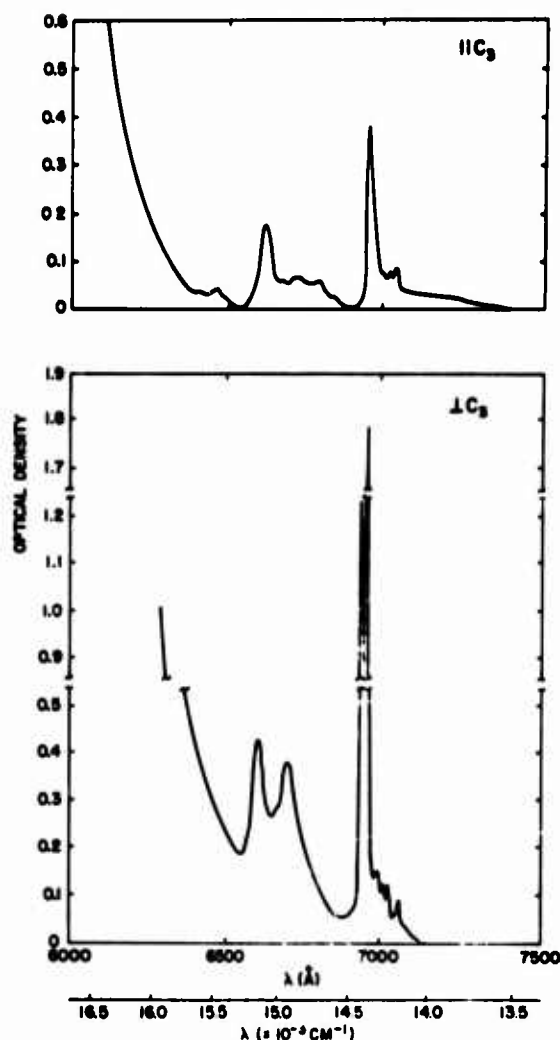


Figure 10. Absorption Spectra of Ruby (4.26 mm) with 2.1% Chromium in the Region of the S, R, and N Lines at 295°K

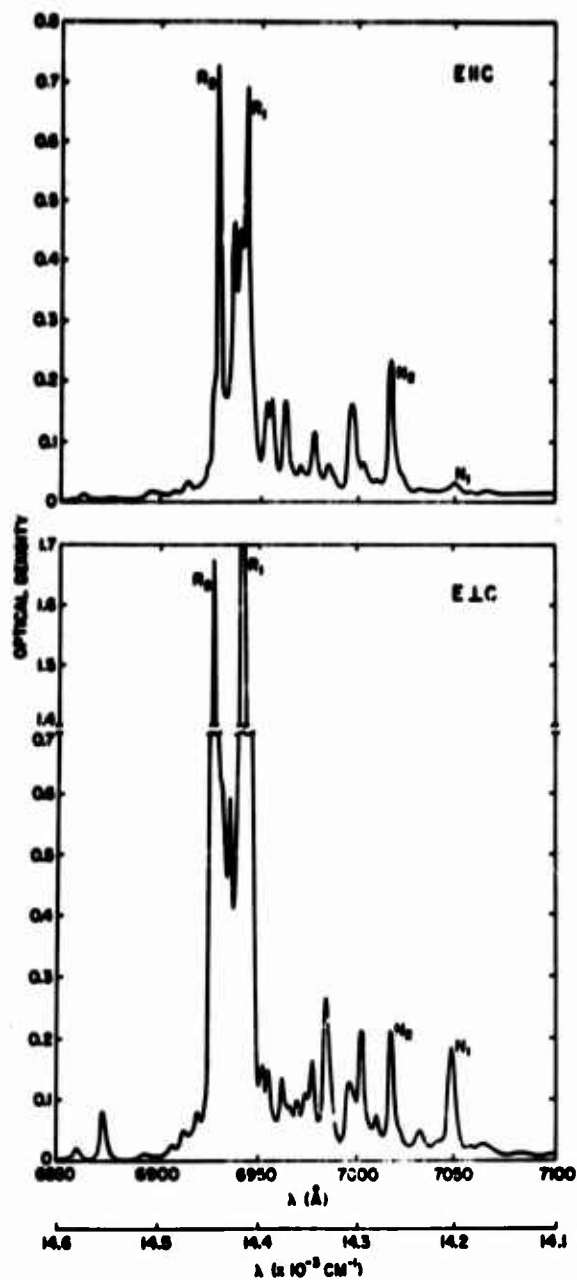


Figure 11. Absorption Spectra of Ruby (4.26 mm) with 2.1% Chromium in the Region of the R and N Lines at 77°K

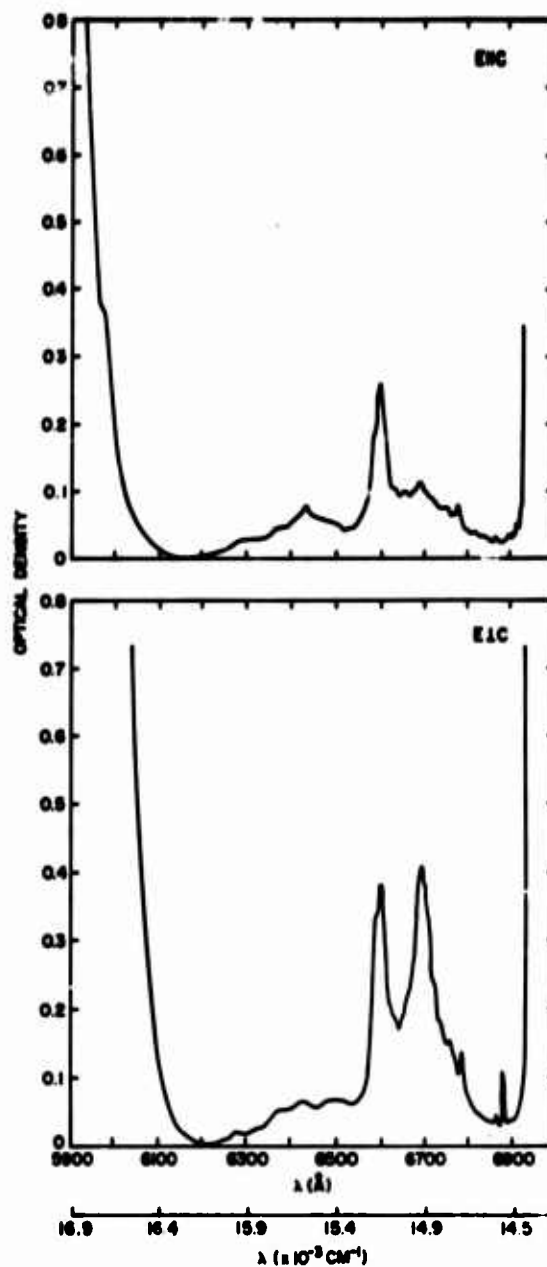


Figure 12. Absorption Spectra of Ruby (4.26 mm) with 2.1% Chromium in the Region of the S Lines at 77°K

Table 6. Absorption Lines Near the S Lines of Ruby With 2.1% Cr at 77°K

$\lambda(\text{\AA})$		$\tilde{\nu}(\text{cm}^{-1})$	
$E \perp c$	$E \parallel c$	$E \perp c$	$E \parallel c$
6275	6280	15,936	15,924
6375	6380	15,686	15,674
6425	6435	15,564	15,540
6490	6460	15,408	15,480
(S ₃) {	6590	15,174	15,174
	6598	15,156	15,152
	6630	15,083	15,072
	6655	15,026	15,026
(S ₂)	6690	14,948	14,948
	6730	14,859	14,881
(S ₁)	6760	14,793	14,815
(S ₀)	6780	14,749	14,749
	6805	14,695	14,674
	6865	14,567	14,567
	6880	14,535	
	6900	14,493	14,493

Table 7. Absorption Lines Near the B Lines of Ruby With 2.1% Cr at 77°K

$\lambda(\text{\AA})$		$\tilde{\nu}(\text{cm}^{-1})$	
$E \perp c$	$E \parallel c$	$E \perp c$	$E \parallel c$
4589	4590	21,791	21,786
4606	4606	21,711	21,711
4622	4622	21,636	21,636
4633	4631	21,584	21,584
4647	4646	21,519	21,524
4664	4664	21,441	21,441
(B ₃)	4691	21,317	21,317
	4707	21,245	21,254
	4714	21,213	21,213
	4732		21,133
	4742	21,088	21,079
(B ₂)	4753	21,039	21,035
(B ₁)	4770	20,964	20,964
	4787	20,890	20,903
	4792		20,868
4811	4811	20,786	20,786
	4817		20,760
	4840		20,661

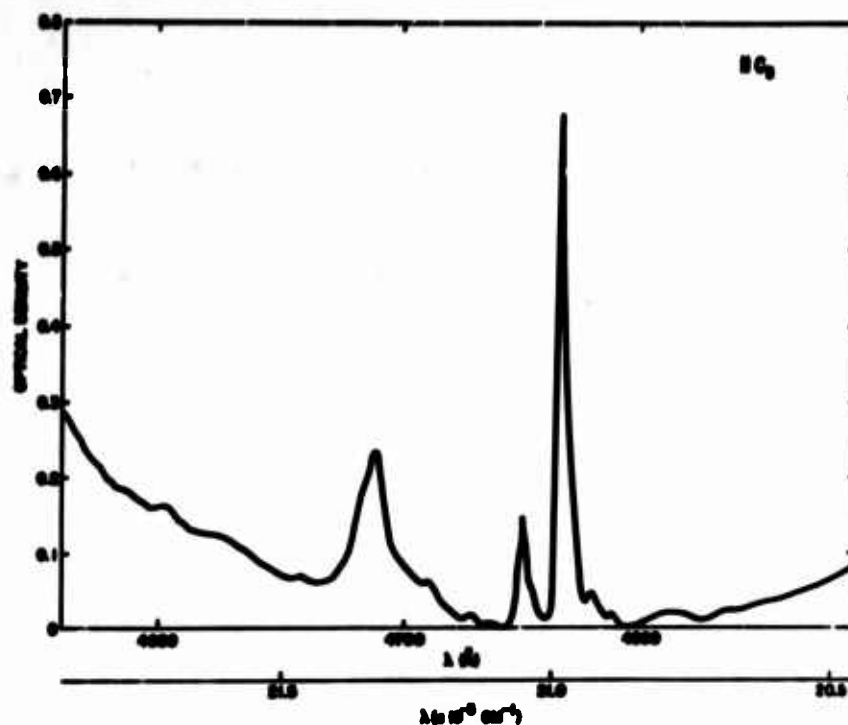


Figure 13. Absorption Spectrum ($E \parallel C$) of Ruby (0.84 mm) with 2.1% Chromium in the Region of the B Lines at 77°K

The pair band for the thick 2.1% sample at 77°K is shown in Figure 15. The peaks of the band are listed in Table 8. The observed structure is similar to that reported by Linz and Newnham (1961) and Naiman and Linz (1963) but is somewhat shifted toward longer wavelengths.

Table 8. Absorption "Pair Band" in Ruby with 2.1% Cr at 77°K

$E \perp c$		$E \parallel c$	
$\lambda (\text{\AA})$	$\tilde{\nu} (\text{cm}^{-1})$	$\lambda (\text{\AA})$	$\tilde{\nu} (\text{cm}^{-1})$
3263	30,647	3255	30,722
3272	30,562	3274	30,544
3309	30,221	3303	30,276
3360	29,762	3309	30,221
3400	29,412	3337	29,967
3407	29,351	3353	29,824
3426	29,189	3357	29,789
3440	29,070	3383	29,560
3460	28,902	3387	29,525
3474	28,785	3411	29,317
3493	28,629	3425	29,197
		3434	29,121
		3441	29,061
		3449	28,994

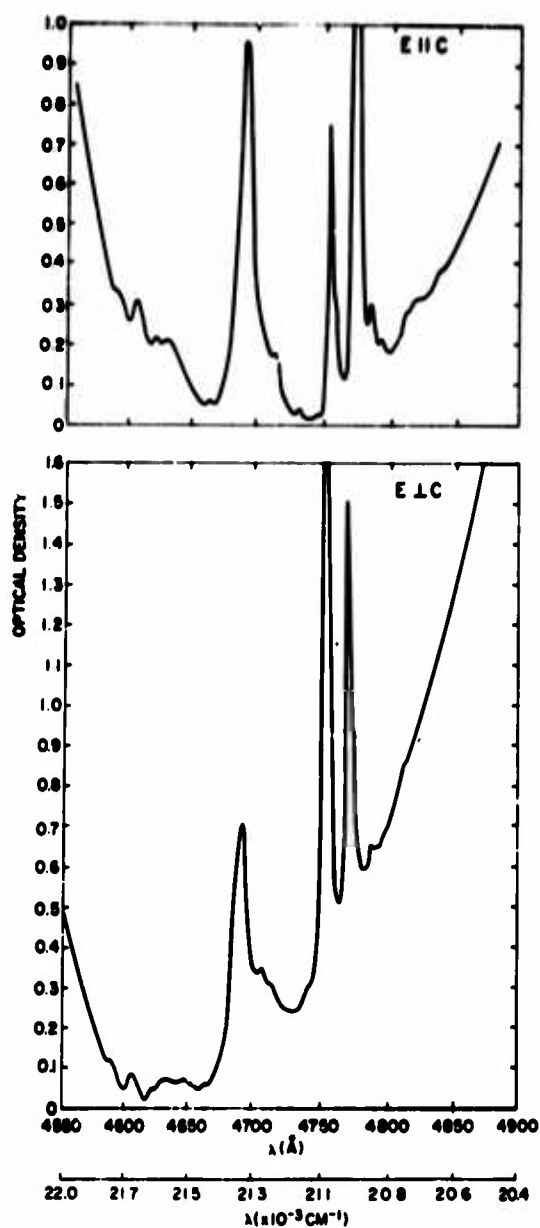


Figure 14. Absorption Spectra of Ruby (4.26 mm) with 2.1% Chromium in the Region of the B Lines at 77°K

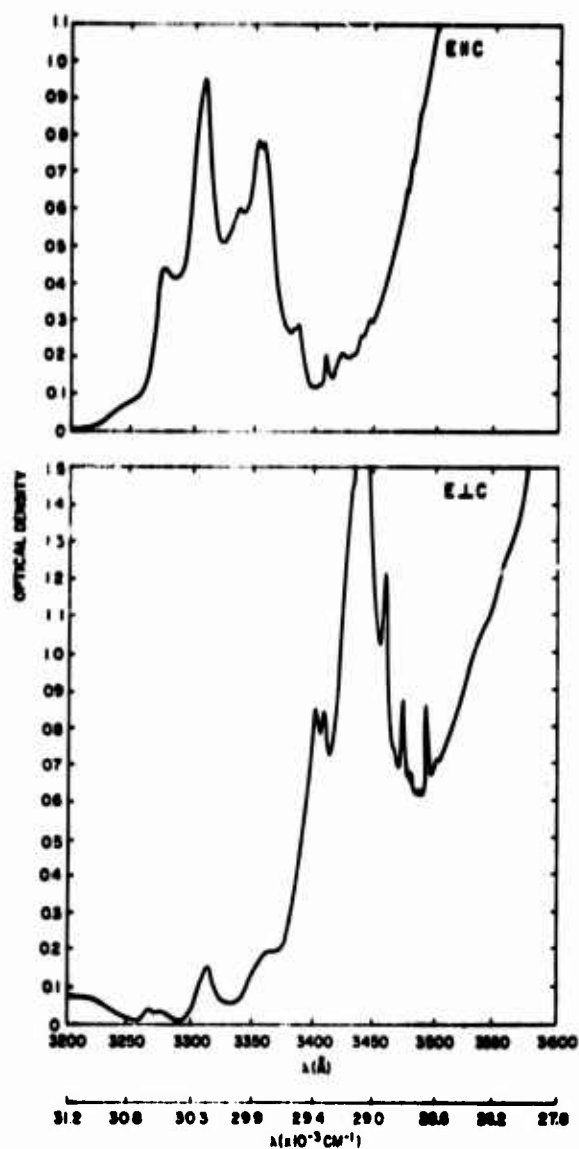


Figure 15. Absorption Spectra of Ruby (4.26 mm) with 2.1% Chromium in the Region of the "Pair Band" at 77°K

6. RESULTS AND DISCUSSION OF CONTINUOUS FLUORESCENCE EXPERIMENTS

The fluorescence spectra of ruby samples with 0.03%, 0.94%, and 2.1% chromium (samples No. 1, 2, and 3 of Table 5, respectively) were observed at several temperatures ranging from 15°K up to 705°K. The experimental equipment used was described in Section 4.3. The monochromator was used with the grating in first order and the slits opened to 20 μ which gave a resolution of 0.3 Å in the spectral region investigated. All experimental parameters were held constant as the temperature was varied. The monochromator scanning speed was reduced in the region of the R and N lines because of their sharpness. The amplifier gain was also reduced in this region so the no-phonon lines and vibronics could be seen in the same figure.

It should be noted that the spectra shown in Figures 16 to 19 have not been corrected for photomultiplier response and grating efficiency. Taking this into account would cause the no-phonon lines to be slightly greater than they appear with respect to the large band at 7750 Å.

6.1 Fluorescence Spectrum of Lightly Doped Ruby

The fluorescence spectrum of 0.03% ruby is shown in Figure 16 for various temperatures. This fluorescence spectrum consists of two parts:

- (1) The sharp no-phonon lines due to pure electronic transitions, and
- (2) The broad vibronic bands due to vibrationally assisted electronic transitions.

The bands on the high energy side of the no-phonon lines correspond to the simultaneous absorption of a phonon and emission of a photon. The vibronics on the low energy side of the no-phonon lines are due to the concurrent emission of a phonon and photon. The fluorescence observed on the high energy side of the R lines at room temperature and above, between 6600 Å and 6690 Å, is due to emission from the ${}^2T_1(t_2^3)$ levels (McClure, 1959 and Kushida). These lines have been observed to be in thermal equilibrium with the R lines (Misu, 1964).

The two broad bands and the B lines seen in absorption do not appear in the fluorescence spectrum. This is because the energy absorbed at these frequencies is transferred to the lower lying 2E metastable state by radiationless processes and then emitted at the R lines. Misu (1964) has suggested, however, that fluorescence appearing around 6210 Å may be due to emission from the 4T_2 level which gives rise to the U absorption band.

The most striking feature of the thermal dependence of the fluorescence is its change in spectral distribution. At 545°K the emission energy is spread out over a wide region of the spectrum with low intensity. As the temperature is lowered, the spectral region of the significant fluorescence decreases, more energy is

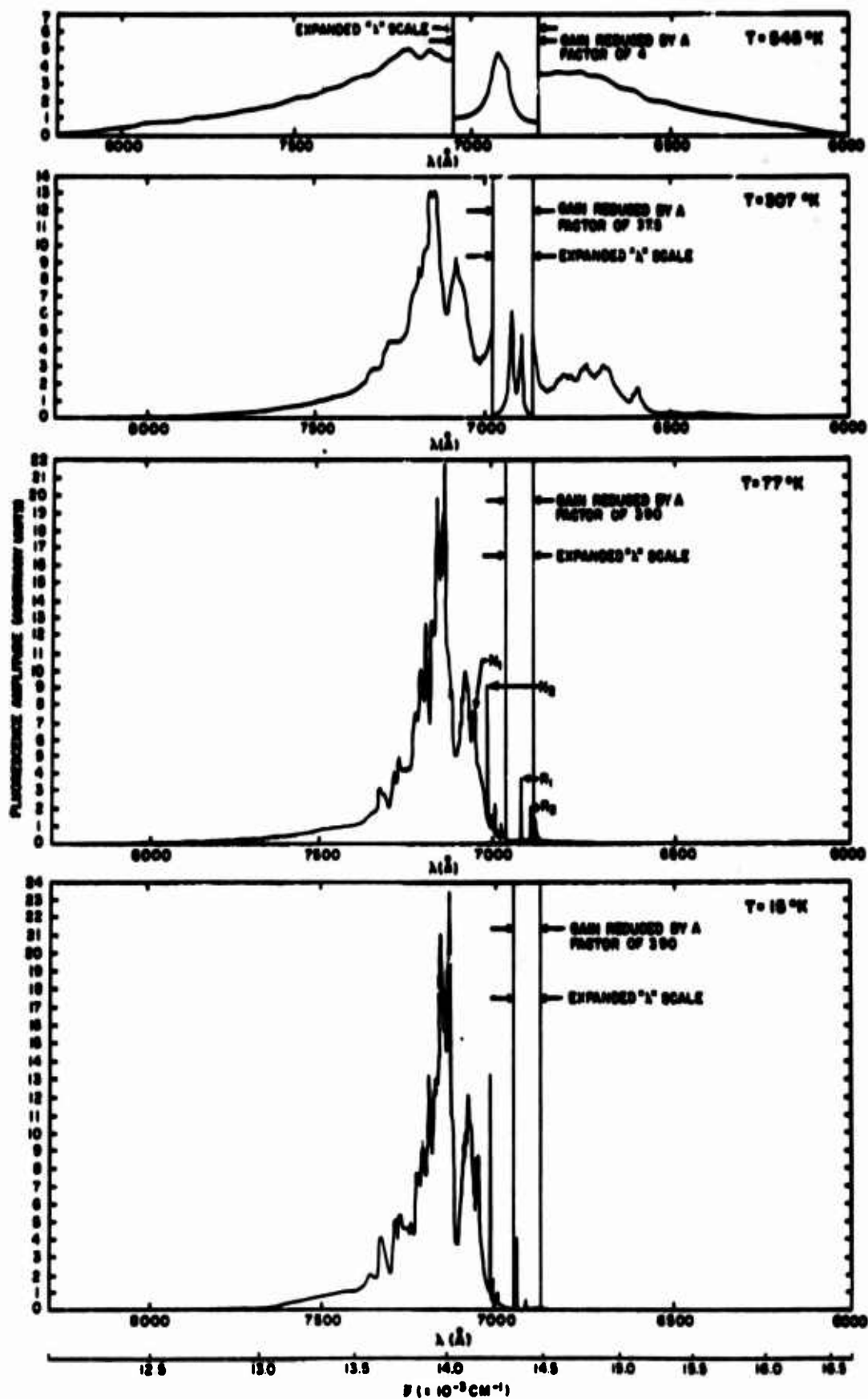


Figure 16. Fluorescence Spectrum of Ruby with 0.03% Chromium.

emitted in the no-phonon lines and less in the vibronics. At 15°K nearly all the energy is emitted in an extremely intense spike at the R_1 line.

The vibronics at 545°K are almost symmetric about the R lines. They extend from 6000 Å to 8100 Å, indicating the presence of multiphonon processes. Above room temperature their appearance is similar to that reported by Burns and Nathan (1963). As the temperature is lowered, the extent of the vibronic bands decreases indicating a lower probability of multiphonon processes. The bands exhibit a detailed structure indicating that characteristic phonon frequencies are active (Krishnan, 1947). At 15°K the high energy vibronics have vanished, as expected, due to the lack of phonons available for absorption.

The R_1 and R_2 lines tend to increase in intensity when temperature is lowered. The ratio of the intensity of the R_2 line to the R_1 line decreases, however, according to a Boltzmann factor showing that the populations of their upper levels are in thermal equilibrium (Pringsheim, 1949). At 77°K the N_1 and N_2 lines and several other pair lines can be seen on the low energy side of the R lines. As temperature is lowered to 15°K the two N lines increase in intensity. This effect will be discussed in the next section.

6.2 Fluorescence Spectrum of Heavily Doped Ruby

The fluorescence spectra of ruby with 0.94% and 2.1% Cr^{+3} are shown in Figures 17 and 18, respectively. The thermal characteristics of these spectra are the same as those of the 0.03% sample. At the higher concentrations, however, the fluorescence is spread out over a wider range and is, in general, less intense. The number and intensities of the pair lines visible in the heavily doped samples are, as expected, greater than in the lightly doped sample.

One major difference between the spectrum of heavily doped ruby and the one of lightly doped ruby is the extent and complexity of the former at wavelengths greater than 7100 Å. Figure 16 shows that the R line vibronics at low temperatures and concentrations are not significant at wavelengths greater than 7400 Å. In heavily doped ruby this vibronic spectrum will be complicated by the presence of the pair lines and their vibronics. The lines belonging to first and third nearest neighbors are found between 7150 Å and 7550 Å (Mollenauer, 1965). The band seen beyond this region with its highest peak at about 7750 Å has been attributed by Tolstoi et al. (1962) to transitions involving more than two interacting chromium ions.

The high energy vibronics are less intense in the more concentrated samples and no structure is observed in the 2.1% sample. They have completely disappeared at 77°K for both samples. The amount of fluorescence from the vibronics and the 2T_1 level is much less than in the 0.03% sample because the coupling between single ions and pairs provides a rapid decay mechanism for the ions in the metastable level.

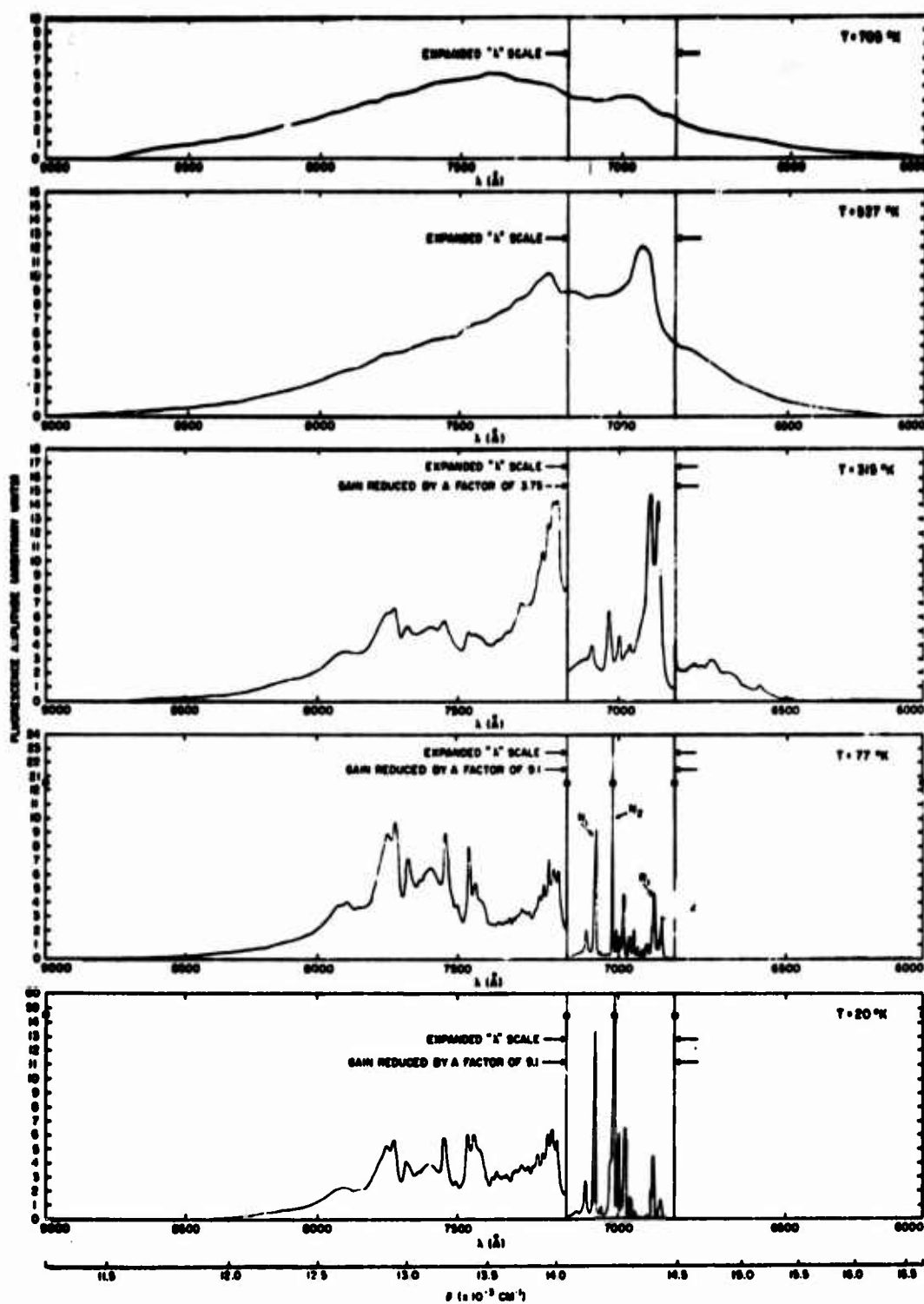


Figure 17. Fluorescence Spectrum of Ruby with 0.94% Chromium

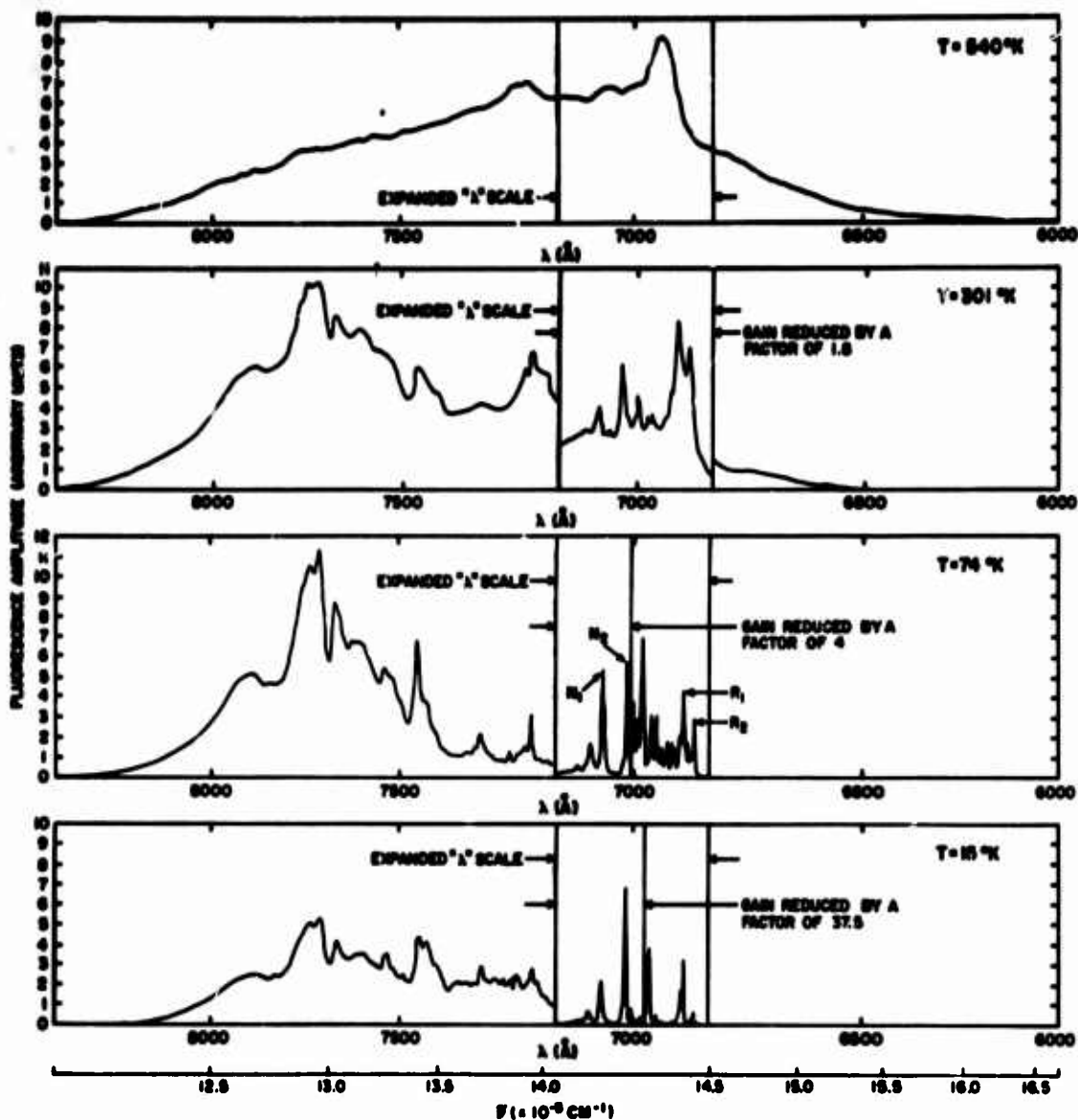


Figure 18. Fluorescence Spectrum of Ruby with 2.1% Chromium

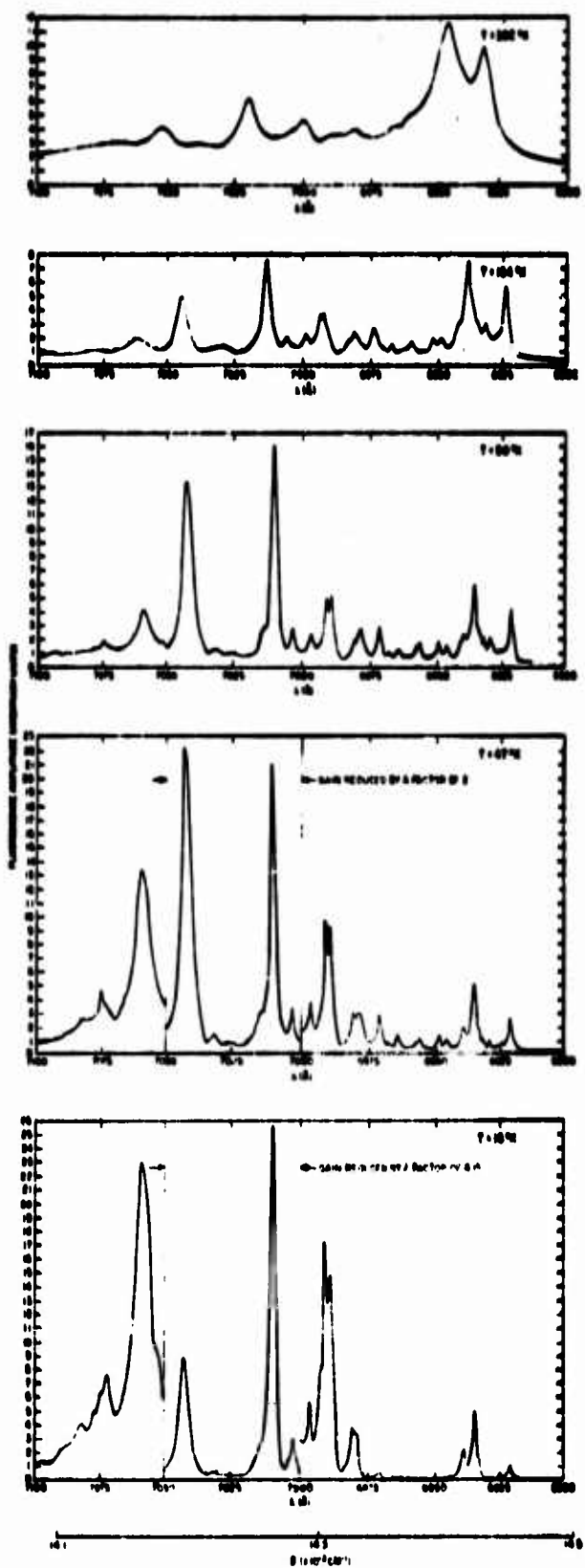


Figure 19. Fluorescence Spectrum of Ruby with 2.1% Chromium in the Region of the R and N Lines

The region of the spectrum of the 2.1% sample consisting of the R lines and the pair lines for second and fourth nearest neighbors is shown in Figure 19. In the heavily doped samples the R lines decrease as temperature is lowered. Also in these samples satellite lines appear on both sides of and in between the R_1 and R_2 lines as they did in absorption.

Both the N lines increase in intensity as temperature is lowered. The intensities of the numerous other pair lines vary differently with decreasing temperature; some increase, others decrease. These observations of the thermal variation of the intensities of the pair lines are discussed in more detail in Section 9. They are explained by considering the levels involved in the specific transitions and the energy transfer between single ion and pair systems.

The lines observed in the spectrum of heavily doped ruby at 77°K are listed in Table 9. The lines marked with an asterisk were also identified in absorption. The positions of the absorption lines are not as accurate as the positions of the fluorescence lines due to the differences in resolution and scanning speed used in the two types of experiments. The region of the fluorescence spectrum which was of interest to this work was between 6900 Å and 7100 Å. The lines listed in Table 9 between 7100 Å and 8000 Å are not as accurate as those reported from 6900 Å to 7100 Å since the former region of the spectrum was observed at a faster scanning speed than the latter region.

Key for Table 9

- * Seen also in absorption (Figure 12)
- + Second nearest neighbor pair lines (Figure 30)
- ++ Fourth nearest neighbor pair lines (Figure 30)
- ⚡ Fourth nearest neighbor pair lines consisting of two poorly resolved lines (Figure 30)

Some of the lines in the region from 7150 Å to 7550 Å have been attributed by Mollenauer (1965) to first and third nearest neighbor pairs. The vibronics also appear in this region. The lines reported at wavelengths greater than 7550 Å are superimposed on a big band with a peak near 7750 Å which has been attributed to multi-ion systems (Tolstoi, 1962).

Table 9. Fluorescence Lines of Ruby with 2.1% Cr at 74°K

$\lambda(\text{\AA})$	$\tilde{\nu}(\text{cm}^{-1})$	$\lambda(\text{\AA})$	$\tilde{\nu}(\text{cm}^{-1})$
6916.0 *	14,459.2	7075.5	14,133.3
6921.0 * (R_2)	14,448.8	7081.0	14,122.3
6924.5	14,441.5	7086.5	14,111.3
6927.2 ++	14,435.8	7092.5	14,099.4
6931.5 *	14,426.9	7110	14,065
6933.5 *	14,422.7	7125	14,035
6935.5 * (R_1)	14,418.6	7145	13,996
6937.0 ++	14,415.4	7162	13,963
6940.5	14,408.2	7179	13,930
6944.0 ++	14,400.9	7188	13,912
6949.0 +	14,390.6	7195	13,898
6956.0 * +	14,376.1	7217	13,856
6957.0 *	14,374.0	7235	13,822
6959.5 * +	14,368.8	7277	13,742
6963.5 * +	14,360.6	7288	13,721
6967.0 * +	14,353.4	7293	13,712
6971.0 * +	14,345.1	7307	13,686
6976.0 * +	14,334.9	7325	13,652
6978.0 * ++	14,330.8	7410	13,495
6978.5 * +	14,329.7	7435	13,450
6980.5 * ++	14,325.6	7453	13,417
6989.0 * ++	14,308.2	7500	13,333
6990.5 * ++	14,305.1	7522	13,294
6991.5 * ++	14,303.1	7538	13,266
6996.0 * ++	14,293.9	7591	13,173
7002.5 * ++	14,280.6	7606	13,148
7009.5 * ++ (N_2)	14,266.4	7624	13,116
7013.0 * ++	14,259.2	7666	13,045
7025.0 * +	14,234.9	7710	12,970
7032.0 * +	14,220.7	7737	12,925
7041.0 * + (N_1)	14,202.5	7769	12,872
7056.0	14,172.3	7845	12,747
7058.0 * +	14,168.3	7890	12,674
7070.0	14,141.3	7916	12,633
7073.5	14,137.3		

(Key on previous page)

7. RESULTS AND DISCUSSION OF EXCITATION EXPERIMENTS

The excitation spectra of the R_1 line of a 0.03% ruby (sample No. 1 in Table 5) and of the R_1 , N_1 , and N_2 lines and the 7750 Å band of a 2.1% ruby (sample No. 3 in Table 5) were observed at 300°K and 4.2°K. The equipment used for these experiments was described in Section 4. The Engis monochromator used to select the wavelength of the exciting radiation was scanned through the range of wavelengths where absorption was observed. The McPherson

monochromator selected the wavelength of the fluorescence to be monitored. Because of the low intensity obtained in these experiments, wide slit widths were needed for both monochromators. The Engis slits were set at 1 mm, which corresponded to a resolution of 55 Å. The McPherson slits were set at 400 μ , which gave a resolution of about 6 Å. Both instruments were used in first order.

7.1 Excitation Spectrum of the R_1 Line of Lightly Doped Ruby

Figure 20 shows the excitation spectrum of the R_1 line of the lightly doped ruby at 300°K and at 4.2°K. The spectrum is approximately the same at the two temperatures. The greatest amount of excitation is obtained by pumping in the two large absorption bands. The bands are not as sharp in excitation as they appear in absorption, probably due to the poorer resolution used in these experiments. The 4T_2 band in excitation is more intense than the 4T_1 band. This is just the opposite of what is seen in absorption and is consistent with the perpendicularly polarized excitation spectrum observed by Misu (1964). This indicates that under these conditions more energy is being transferred to the R metastable levels from the U band than from the Y band.

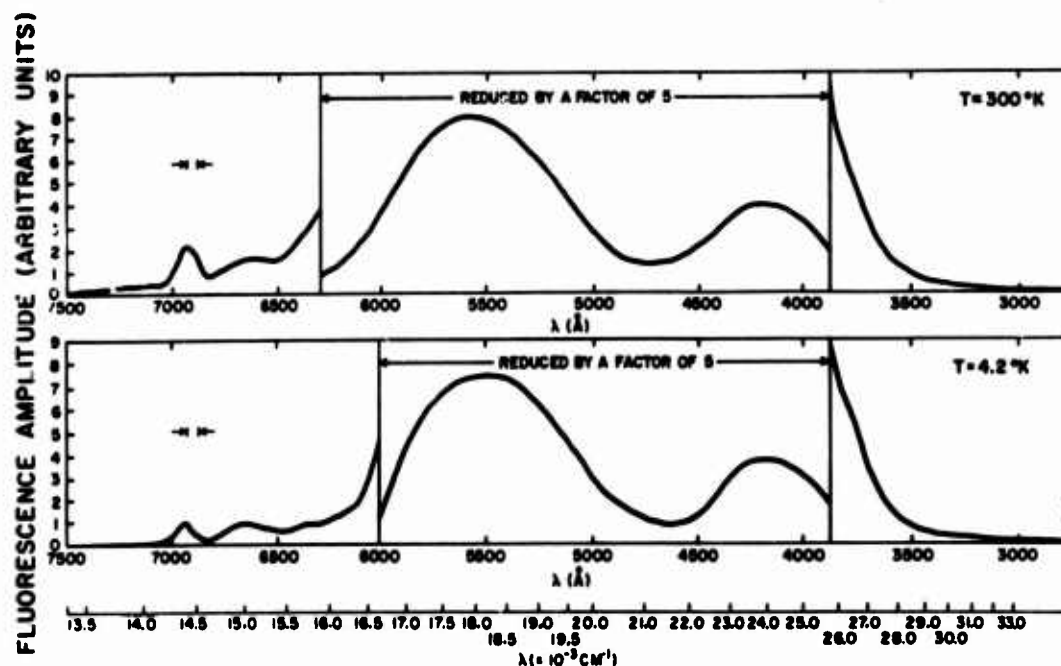


Figure 20. Excitation Spectra of the R_1 Line in Ruby with 0.03% Chromium at 300°K and 4.2°K

There also is an excitation of the R_1 line due to absorption in the region of the S lines (near 6650 Å). This is consistent with the observations of Misu (1964). Resonant radiation is observed in the region of the R_1 line itself (about 6950 Å). Because of the wide slit width the resonant radiation includes scattered light. The emission in this region may also be due to absorption in the R_2 line.

7.2 Excitation Spectra of Heavily Doped Ruby

Figures 21 and 22 show the excitation spectra of the 2.1% sample at temperatures of 300°K and 4.2°K, respectively. The R_1 , N_2 , and N_1 lines and the large fluorescence band near 7750 Å were all investigated at room temperature but at liquid helium temperature the intensity of the R_1 line was too small to give useful results.

At room temperature the three lines and the band all have similar excitation spectra. Instead of two distinct pumping bands as observed in the lightly doped sample, these spectra present a broad, less intense region of excitation with little observable structure. This "flattening" or "saturation" of the excitation spectra is due to the fact that the absorption is so strong in the bands that the incident light at these frequencies does not penetrate very far into the sample (Dexter, 1958).

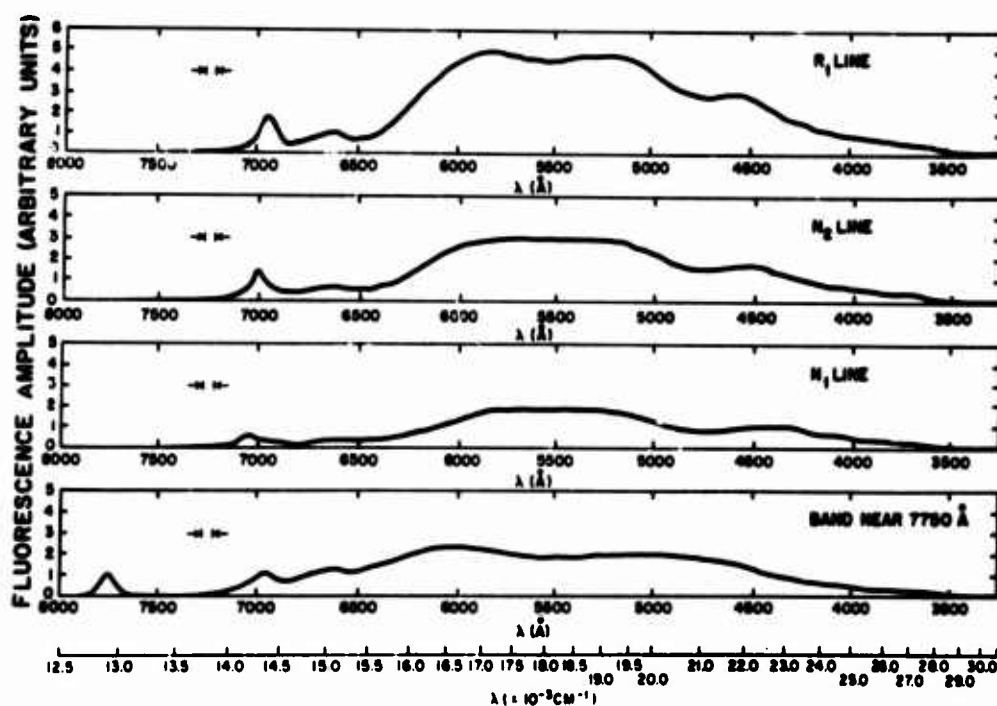


Figure 21. Excitation Spectra of the R_1 , N_1 , and N_2 Lines and the 7750 Å Band in Ruby with 2.1% Chromium at 300°K

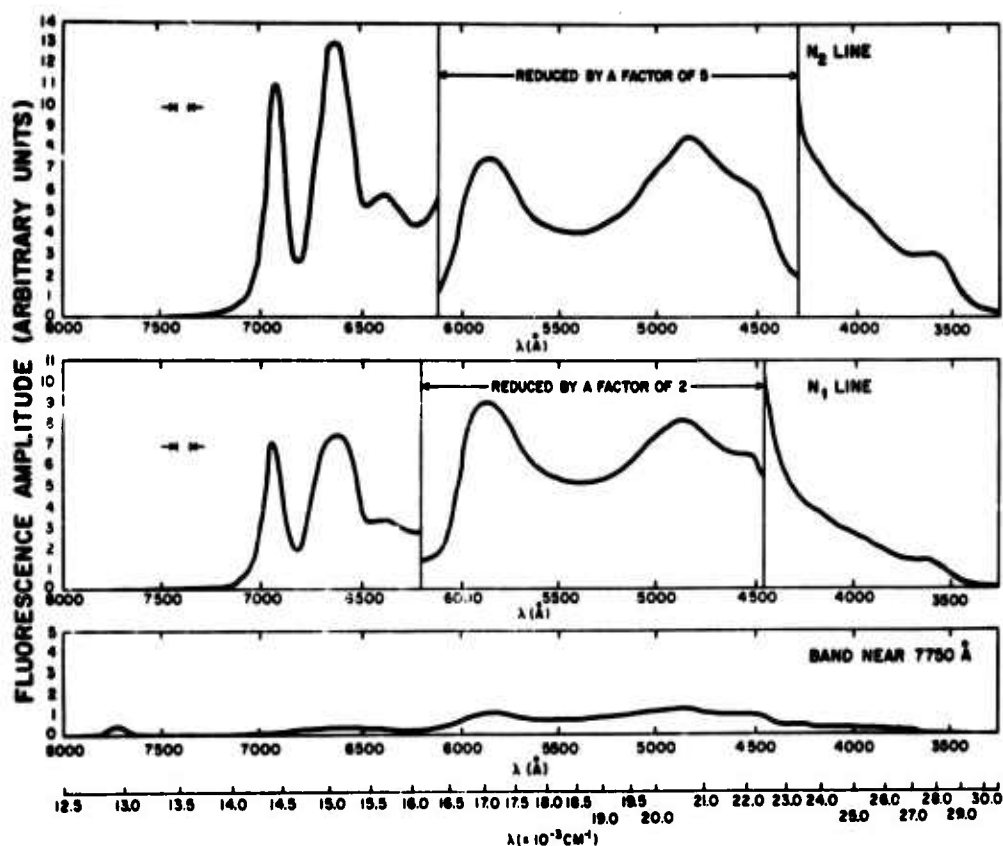


Figure 22. Excitation Spectra of the N Lines and the 7750 Å Band in Ruby with 2.1% Chromium at 4.2°K

The incident light at the frequency of the B lines is absorbed less and thus penetrates further into the sample. The result of this "size effect" is that the excitation through the B lines relative to the excitation through the bands is greater than in the weakly doped sample which absorbs less.

Each of the lines and the band exhibit a resonant excitation peak which will include some scattered radiation. They also all have a peak at about 6000 Å indicating excitation through the S lines. The 7750 Å band has a peak near 6950 Å which indicates pumping through the R lines.

At 4.2°K the excitation spectrum of the 7750 Å band is extremely weak and no distinct structure is observed. The excitation spectra of the N₁ and N₂ lines are, however, more intense at this temperature and a number of bands are observed. This is due to the fact that the fluorescence at the band decreases at low temperatures while the fluorescence at the N lines increases (see Figure 18).

In the region of the two absorption bands the N lines both appear to have two major excitation bands and an indication of a third peak not resolved from one of

the larger bands. They occur at about 4550 Å, 4900 Å, and 5900 Å. Again these peaks are shifted from the positions of the absorption bands and B lines (see Figure 9) due to the "size" effects mentioned above.

There is also a smaller band appearing at about 3600 Å, on the tail of one of the larger bands. This is probably the pair band observed in absorption near 3400 Å. Due to the low intensity of the R_1 line emission it is not clear whether or not it is also excited through this band. However, R_1 fluorescence was observed at room temperature by pulsed excitation in this band (see Section 10).

Both the N lines show strong pumping in the region of the S lines (around 6600 Å to 6700 Å). There is also a peak in the excitation spectra of both lines near 6400 Å. Absorption was also seen in this region (see Table 6 and Figure 13). The resonant absorption peak in the spectra of the two N lines is centered at about 6950 Å and extends to near 7100 Å. This indicates a pumping of the N lines by the R lines.

It should be noted that these measurements cannot throw any further light on the mechanism of excitation of the pair lines; in particular they cannot show whether the pair lines are excited directly through the bands or through the R lines. The energy transfer from single ions to pairs is discussed in more detail in Sections 9 and 10.

8. RESULTS AND DISCUSSION OF LINEWIDTH AND LINESHIFT MEASUREMENTS

The temperature dependence of the widths and positions of the four most prominent lines in the fluorescence spectrum of heavily doped ruby was measured from 13°K up to 450°K. The results for samples containing 2.1% and 0.94% chromium are compared with similar measurements made previously on lightly doped ruby (about 0.05% chromium). The samples used were listed as Nos. 2 and 3 in Table 5. The R_1 and R_2 lines are found to be broadened by microscopic strain, Raman processes, and direct processes between their excited states. The N_1 and N_2 lines are broadened by microscopic strain, Raman processes, and direct processes within the ground state manifolds. The thermal lineshift results are consistent with virtual phonon processes involving different Debye temperatures from those used to fit the linewidth data.

8.1 Theoretical Considerations

McCumber and Sturge (1963) investigated the thermal dependence of the widths and positions of the absorption R lines in lightly doped ruby. They explained the constant width below 77°K as being due to broadening by microscopic strains, and the rapid increase in width with temperature above 77°K as being due to the Raman

scattering of phonons by the impurity ions. Kurnit, Abella, and Hartmann (1966) included a direct process term between the \bar{E} and $2\bar{A}$ levels in the consideration of the R_1 linewidth and obtained a better fit with experimental results. The expression for the linewidth in units of cm^{-1} was derived in Section 3. The result was given in Eq. (92) as

$$\Delta \tilde{\nu} = \Delta \tilde{\nu}_0 + \bar{\alpha} \left(\frac{T}{T_D} \right)^7 \int_0^{T_D/T} \frac{x^6 e^x}{(e^x - 1)^2} dx + \sum_{j < i} \beta_{ij} \left(\frac{e^{\frac{\Delta E_{ij}}{KT}}}{e^{\frac{\Delta E_{ij}}{KT}} - 1} \right) + \sum_{j > i} \beta_{ij} \left(\frac{1}{e^{\frac{\Delta E_{ij}}{KT}} - 1} \right) \quad (105)$$

where:

$\Delta \tilde{\nu}_0$ = contribution due to microscopic strain,

T_D = effective Debye temperature,

and the contributions due to multiphonon processes are neglected.

As was mentioned in Section 3 the strain broadening due to the random crystal field distortion at the site of each chromium ion gives a Gaussian contribution to the line shape. The broadening due to the phonon processes, which have the same probability of occurrence for each ion, produces a Lorentzian line shape. The superposition of the two contributions gives a Voigt profile whose half width is not exactly equal to the sum of the Gaussian and Lorentzian halfwidths. Equation (105) may, however, still be considered a good approximation. The $\bar{\alpha}$ and β_{ij} are treated as adjustable parameters to obtain a fit with experimental results. They are a measure of the coupling of the impurity ion to the lattice. Temperature T_D may be different from the Debye temperature found from specific heat measurements since phonons of different frequencies may interact differently with the impurity ion.

The shift of a spectral line with temperature is caused by the continual absorption and re-emission of virtual phonons by the impurity ion in a phonon field. The temperature dependent shift expressed in units of cm^{-1} was also derived in Section 3 and the result was given in Eq. (104) as

$$\delta \tilde{\nu} = \alpha \left(\frac{T}{T_D} \right)^4 \int_0^{T_D/T} \frac{x^3}{e^x - 1} dx + \sum_{j < i} \beta_{ij}'' \left(\frac{T}{\Delta E_{ij}} \right)^2 P \int_0^{T_D/T} \frac{x^3}{e^x - 1} \frac{1}{x^2 - \left(\frac{\Delta E_{ij}}{KT} \right)^2} dx - \sum_{j > i} \beta_{ij}'' \left(\frac{T}{\Delta E_{ij}} \right)^2 P \int_0^{T_D/T} \frac{x^3}{e^x - 1} \frac{1}{x^2 - \left(\frac{\Delta E_{ij}}{KT} \right)^2} dx \quad (106)$$

where P denotes the principal part of the integral. Again the α and β'' coefficients are adjustable parameters. The last two terms represent the absorption and emission of virtual phonons with frequencies corresponding to real transitions from the levels considered. These were found to be negligible in lightly doped ruby (McCumber and Sturge, 1963). They have been found to contribute to thermal lineshifts in other materials however (Yen et al., 1964).

There is no reason to expect that T_D will have the same value for linewidth and lineshift processes since a specific phonon may contribute differently to the two types of processes on account of different selection rules. In fact, Imbusch et al. (1964) suggested that the effective phonon distributions in ruby would be different in Eqs. (105) and (106). In lightly doped ruby McCumber and Sturge found, however, that good results could be obtained assuming the same effective Debye temperature.

8.2 Experimental Results

The width of the R_1 fluorescence line in a 0.03% sample was measured at several temperatures above 77°K. The results agree quite well with the absorption data of McCumber and Sturge.

Figures 23 and 24 show the experimental results of the thermal variation of fluorescence linewidth of the R and N lines in the 2.1% and 0.94% samples, respectively, in the temperature range from 13°K to 450°K. The shifts in position of the R and N lines with temperature below their values at 0°K are shown in Figure 25 for the two samples in the same temperature range. The data was obtained using the continuous fluorescent apparatus described in Section 4. At 77°K and below, the grating was used in second order and the slits set at 10μ to achieve a resolution of 0.14 cm^{-1} . Above 77°K the grating was used in first order which gave a resolution of 0.306 cm^{-1} for a $10\text{-}\mu$ slit width.

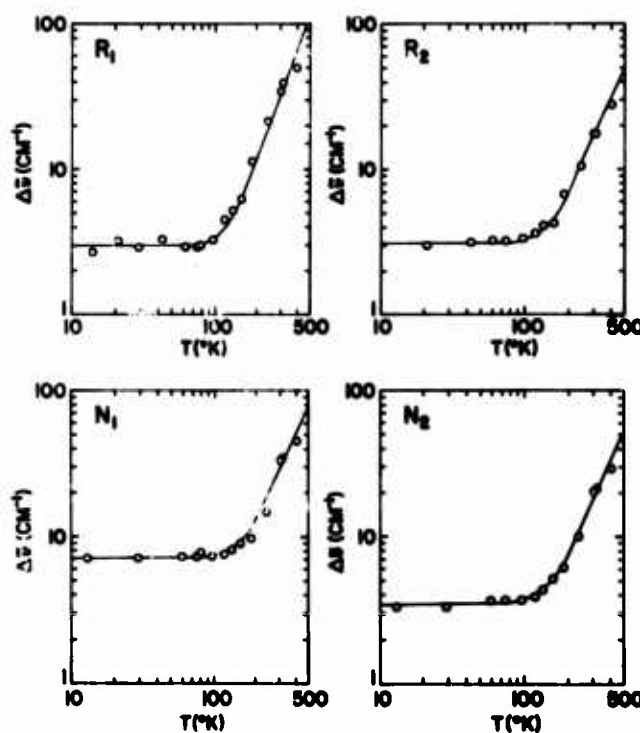


Figure 23. Linewidths of the R and N Lines in Ruby with 2.1% Chromium. The theoretical curves are obtained from Eq. (105) with the parameters shown in Table 14.

This slit width was used at all temperatures in measurements on the 0.94% sample but for the 2.1% sample above 200°K a slit width of 20 μ was used. For the 2.1% sample a scanning speed of 2.5 Å/minute was used below 300°K and 25 Å/minute above this temperature. For the 0.94% sample a scanning speed of 1.0 Å/minute was used up to 82°K; then 2.5 Å/minute was used up to 300°K and 5 Å/minute was used above this temperature. An amplifier response time of 0.1 second was used for all measurements.

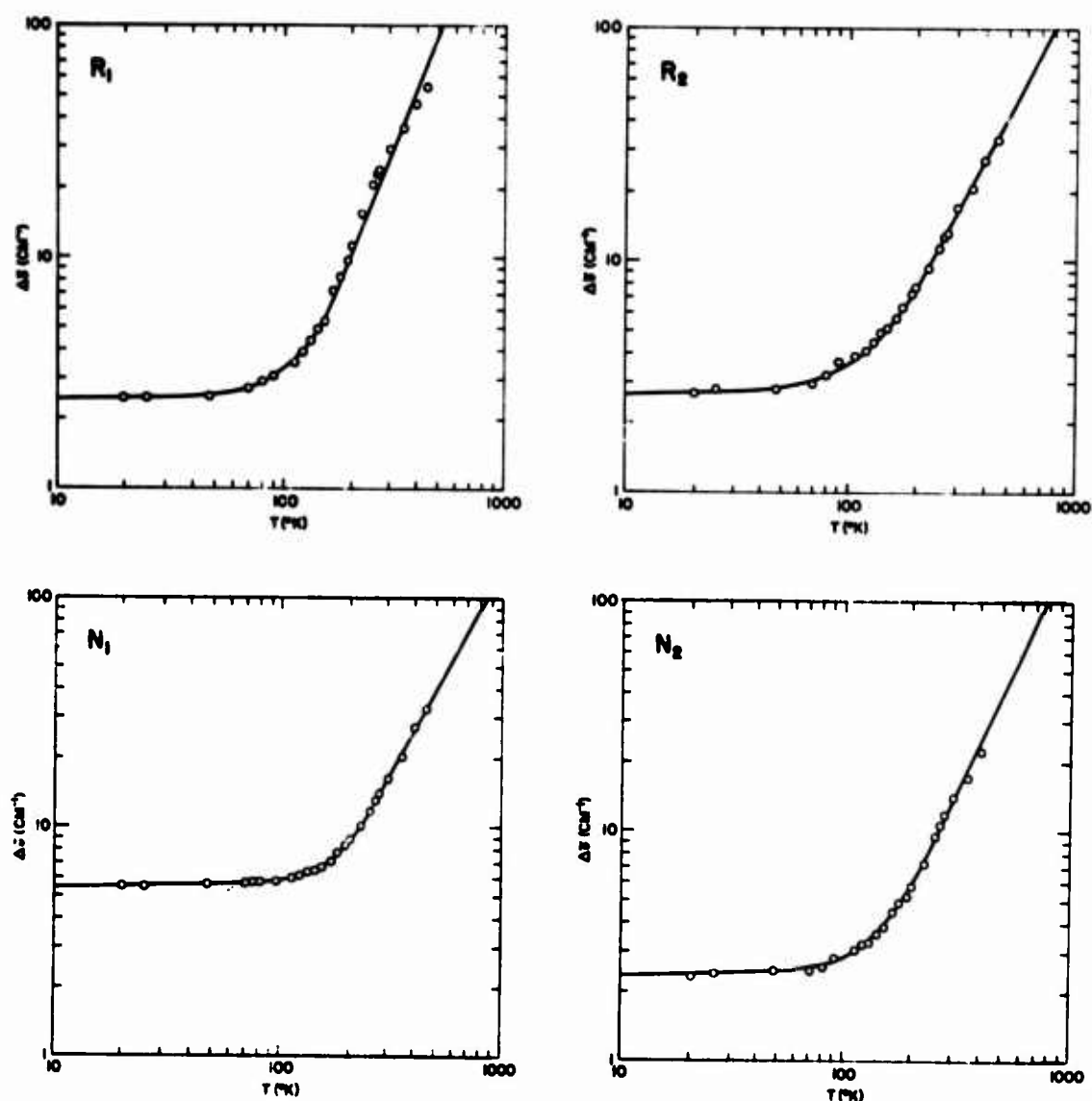


Figure 24. Linewidths of the R and N Lines in Ruby with 0.94% Chromium. The theoretical curves are obtained from Eq. (105) with the parameters shown in Table 14

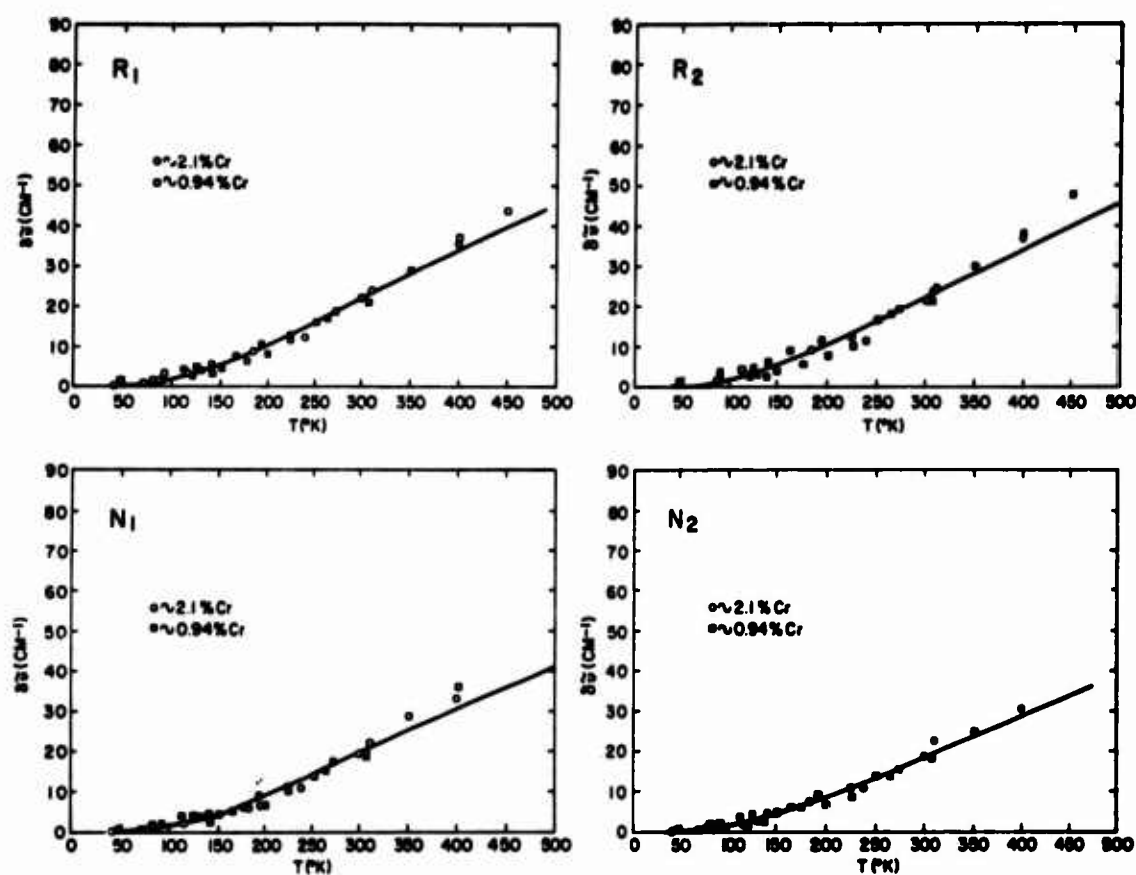


Figure 25. Energy Shift of the R and N Lines Below Their Values at 0°K for Ruby with 2.1% and 0.94% Chromium. The theoretical curves are obtained from Eq. (106) with the parameters given in Table 14.

Tables 10 and 11 list the results of the linewidth measurements for the two samples. Tables 12 and 13 list the lineshift results. The estimated accuracy of the linewidth measurements of the 2.1% sample is $\pm 10\%$ for the R lines and $\pm 5\%$ for the N lines. For the 0.94% sample the estimated accuracy of the linewidths is $\pm 2\%$ for the R lines and $\pm 5\%$ for the N lines. The estimated accuracy of the measurements of the position of a line is 1/10 to 1/20 of the linewidth.

Table 10. Experimental Data on Linewidth of Ruby (2.1% Cr)

T (°K)	$\Delta\tilde{\nu}_{R_1}$ (cm ⁻¹)	$\Delta\tilde{\nu}_{R_2}$ (cm ⁻¹)	$\Delta\tilde{\nu}_{N_1}$ (cm ⁻¹)	$\Delta\tilde{\nu}_{N_2}$ (cm ⁻¹)
13	2.70		7.06	3.32
21	3.21	3.00		
29	2.91		7.06	3.32
42	3.32	3.18		
62	2.91	3.24	7.35	3.66
74	2.91	3.24	7.26	3.66
80	3.02		7.76	3.66
96	3.25	3.37	7.27	3.74
117	4.57	3.66	7.61	3.96
132	5.20	4.17	8.06	4.39
155	6.24	4.23	8.47	5.18
184	11.42	6.78	9.68	6.24
240	21.31	10.60	14.71	10.11
301	34.22	17.70	33.15	20.30
311	39.35	17.70	34.10	21.30
400	49.60	28.08	45.50	29.35

Resolution: 0.14 cm⁻¹ for T ≤ 74°K
 0.31 cm⁻¹ for 80°K ≤ T ≤ 184°K
 0.61 cm⁻¹ for T ≥ 240°K

Table 11. Experimental Data on Linewidth of Ruby (0.94% Cr)

T (°K)	$\Delta\tilde{\nu}_{R_1}$ (cm ⁻¹)	$\Delta\tilde{\nu}_{R_2}$ (cm ⁻¹)	$\Delta\tilde{\nu}_{N_1}$ (cm ⁻¹)	$\Delta\tilde{\nu}_{N_2}$ (cm ⁻¹)
20	2.453	2.714	5.545	2.299
25	2.474	2.818	5.545	2.380
47	2.494	2.818	5.645	2.441
70	2.702	2.965	5.645	2.441
81	2.910	3.215	5.685	2.502
92	3.013	3.652	5.644	2.746
112	3.449	3.902	5.945	2.989
120	3.886	4.070	6.048	3.152
130	4.363	4.445	6.247	3.193
140	4.882	4.902	6.367	3.499
150	5.236	5.155	6.549	3.762
164	7.165	5.631	6.951	4.391
176	8.060	6.259	7.655	4.777
192	9.654	7.234	8.257	5.121
200	11.111	7.780	8.763	5.631
225	15.256	9.297	9.966	7.152
251	20.331	11.458	11.572	9.383
265	22.090	12.914	12.274	10.419
273	23.010	13.016	13.839	11.675
307	29.020	16.916	16.087	13.761
351	35.720	20.274	20.080	16.729
401	45.200	27.000	27.580	21.780
451	53.730	32.670		

Resolution: 0.14 cm⁻¹ for T ≤ 70°K
 0.31 cm⁻¹ for T ≥ 81°K

Table 12. Experimental Data on Lineshift of Ruby (2.1% Cr)

T (°K)	λ_{R_1} (Å)	$\delta\tilde{\nu}_{R_1}$ (cm ⁻¹)	λ_{R_2} (Å)	$\delta\tilde{\nu}_{R_2}$ (cm ⁻¹)	λ_{N_1} (Å)	$\delta\tilde{\nu}_{N_1}$ (cm ⁻¹)	λ_{N_2} (Å)	$\delta\tilde{\nu}_{N_2}$ (cm ⁻¹)
~ 0	6934.90	0	6920.85	0	7041.80	0	7009.80	0
42	6934.95	0.21			7041.85	0.10	7009.90	0.10
80	6935.60	1.46			7042.16	0.78	7010.48	1.38
88	6935.85	1.88	6921.50	1.73				
117	6936.50	3.33	6922.15	2.88	7042.80	2.02	7010.74	1.83
184	6939.20	8.94	6924.60	8.81	7044.80	6.05	7013.50	7.52
198					7045.09	6.63		
240	6940.78	12.22	6926.20	11.15	7047.19	10.86	7015.00	10.57
301	6945.50	22.01	6930.50	21.11	7051.50	19.53	7019.00	18.70
311	6946.50	24.08	6932.50	24.27	7053.00	22.55	7021.00	22.76
400	6952.00	35.47	6938.50	36.74	7058.50	33.60	7025.10	30.87

Resolution: 0.14 cm⁻¹ for T < 42.5°K0.31 cm⁻¹ for 80°K < T < 198.5°K0.61 cm⁻¹ for T > 240°K

Table 13. Experimental Data on Lineshift of Ruby (0.94% Cr)

T (°K)	λ_{R_1} (Å)	$\delta\tilde{\nu}_{R_1}$ (cm ⁻¹)	λ_{R_2} (Å)	$\delta\tilde{\nu}_{R_2}$ (cm ⁻¹)	λ_{N_1} (Å)	$\delta\tilde{\nu}_{N_1}$ (cm ⁻¹)	λ_{N_2} (Å)	$\delta\tilde{\nu}_{N_2}$ (cm ⁻¹)
~0	6934.90	0	6920.25	0	7042.00	0	7010.20	0
47	6935.35	1.0	6920.70	1.0	7042.45	0.9	7010.37	0.7
70	6935.05	0.3	6920.32	0.2	7042.27	0.6	7010.36	0.6
81	6935.68	1.6	6920.80	1.1	7042.90	1.8	7011.00	1.9
91	6936.32	3.0	6921.50	2.6	7043.20	2.5	7011.05	2.5
112	6936.85	4.1	6922.16	4.0	7043.97	4.0	7011.93	3.8
120	6936.30	2.9	6921.25	2.1	7042.95	2.0	7011.00	1.9
125	6937.44	5.3	6922.40	4.5	7044.20	4.4	7012.22	4.4
130	6937.00	4.4	6922.00	3.6	7044.00	4.0	7011.70	3.3
140	{6936.55 6937.60}	{3.5 5.6}	{6921.45 6923.18}	{2.5 6.1}	{7043.23 7044.40}	{2.5 4.7}	{7011.35 7012.25}	{2.7 4.5}
150	6937.10	4.6	6922.00	3.6	7044.37	4.8	7012.40	4.8
164	6938.63	7.6	6924.45	8.8	7044.60	5.2	7013.15	6.3
176	6938.10	6.6	6922.90	5.5	7045.20	6.4	7013.15	6.3
192	6940.00	10.6	6925.54	11.0	7046.47	9.0	7014.62	9.3
200	6938.97	8.5	6924.00	7.8	7045.40	6.9	7013.30	6.6
225	{6940.97 6940.10}	{10.8 12.6}	{6926.10 6925.00}	{12.2 9.9}	{7047.48 7047.00}	{11.1 10.1}	{7015.25 7014.15}	{10.6 8.4}
251	6942.75	16.3	6928.10	16.3	7048.85	13.8	7016.80	13.7
265	6943.18	17.2	6928.75	17.7	7049.65	15.4	7016.90	13.9
273	6944.05	19.0	6929.40	19.0	7050.62	17.4	7017.67	15.5
307	6945.00	21.0	6930.42	21.1	7051.60	19.3	7019.12	18.4
351	6949.00	29.2	6934.65	30.0	7056.25	28.7	7022.40	25.1
401	6952.70	36.9	6938.50	38.0	7060.00	36.2	7025.40	31.2
451	6956.20	44.2	6943.25	47.9				

Resolution: 0.07 cm⁻¹ for T ≤ 70°K
0.15 cm⁻¹ for T ≥ 81°K

8.3 Interpretation of Results and Conclusions

Qualitatively the thermal dependences of the linewidths shown in Figures 23 and 24 are similar to those of the 0.03% sample in that they are constant up to 77°K and then increase rapidly with temperature; however, the coupling coefficients are different and the thermal variations of all lines cannot be fit with theoretical curves based on Raman scattering alone.

The shapes of the lines were investigated at low temperatures to determine the extent of direct process broadening. The closeness of the satellite lines to the R lines prohibited any conclusive results with regard to these lines. Accurate shapes could be determined for both the N lines, however. For example, Figure 26 shows the shape of the N_1 line in the 2.1% sample at 21°K where broadening from Raman processes is negligible. It falls between a Gaussian and a Lorentzian curve, indicating that there are contributions to the broadening from both microscopic strain and phonon processes. By analyzing this shape using Posener's tables of Voigt profiles (1959) the two contributions were separated.*

In Section 9 the energy level systems of heavily doped ruby are established and the results shown in Figure 30. Note that the R lines terminate on the ground state while the N lines both terminate on an upper component of the exchange split ground state manifolds.

At very low temperatures the widths of the lines originating from a metastable N state and terminating on the ground state should give a good indication of the strain broadening of all the lines originating from the same level. The width of the transition to the ground state of the N_2 system was measured and found to be in

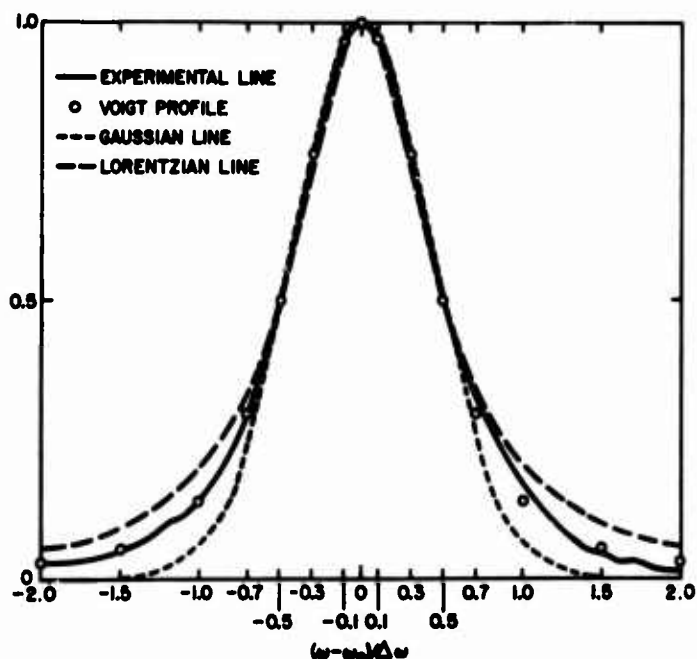


Figure 26. Shape of the N_1 Line in Ruby with 2.1% Chromium at 21°K

*The instrumental broadening at low temperatures was always much less than 10% of the strain broadening. This would also give an approximately Gaussian contribution to the linewidth (Nelson and Sturge, 1965).

good agreement with the strain broadening determined from line shape analysis of the N_2 line as mentioned above. The width of the transition to the ground state of the N_1 system is greater than expected from line shape analysis of the N_1 line. Kisliuk and Krupke (1965) found that the line they assigned to the ground state transition of this system disappeared in absorption at low temperatures. Therefore, they interpreted this line as arising from a vibronic transition near a forbidden no-phonon line. In this case we would expect it to be broader than the no-phonon line.

The strain broadening for the R lines is greater in the samples used here than in the 0.03% sample; it is greatest in the 2.1% sample. For the 2.1% sample the observed strain linewidths are in the order $\Delta\nu_{N_1} > \Delta\nu_{R_2} > \Delta\nu_{N_2} > \Delta\nu_{R_1}$. In the 0.94% sample, they are $\Delta\nu_{N_1} > \Delta\nu_{R_1} > \Delta\nu_{R_2} > \Delta\nu_{N_2}$. The N_1 line has been assigned by Kisliuk, Schawlow, and Sturge (1964) to second nearest neighbor pairs and the N_2 line to fourth nearest neighbor pairs. We would expect the strain field associated with the second nearest neighbor impurities to be greater than that associated with the fourth nearest neighbor impurities, implying that N_1 should be broader than N_2 . This is confirmed experimentally for both samples.

Theoretical fittings of the temperature dependence of the linewidths and line-shifts of the different lines were obtained by using formulas (105) and (106) respectively, with the parameters shown in Table 14. The parameters used by McCumber and Sturge for lightly doped ruby are also shown for comparison. The accuracy of the fitting parameters is approximately 10% for the effective Debye temperatures, 5% for the Raman scattering coefficients, and 20% for the direct process coefficients. The fittings shown for the R_1 and R_2 linewidths of the 2.1% sample are based entirely on Raman scattering using a Debye distribution of phonons with an effective Debye temperature of 760°K. The fittings of the R linewidths for the 0.94% sample have the same T_D but lower values of $\bar{\alpha}$; these fittings also include direct process terms for transitions between the \bar{E} and $2\bar{A}$ levels. McCumber and Sturge used the same T_D but even lower coupling coefficients. In all three samples $\bar{\alpha}_{R_1} > \bar{\alpha}_{R_2}$. For the direct process coefficient of the R_1 line in lightly doped ruby, Kurnit, Abella, and Hartmann (1966) derived a value of 0.004 cm^{-1} from photon echo lifetime results. This is much less than the β coefficients used in fitting the 0.94% curves. For the 2.1% sample, no β coefficients could be derived because of the larger strain broadening.

The fittings of the data for the N linewidths of both the 2.1% and 0.94% samples were obtained by considering a Raman scattering process with a Debye temperature of 935°K plus a direct decay process in the ground state manifold with the selection rule $\Delta S = \pm 2$. This type of process may become active through the modulation of the exchange coupling coefficient J by lattice vibrations and is important when the zero field splitting parameter D is not negligible (Gill, 1962).

Table 14. Linewidth and Lineshift Parameters of Ruby

Sample (Percent Chromium)	Line	Linewidth				Lineshift	
		T_D (°K)	$\bar{\alpha}$ (cm ⁻¹)	β (cm ⁻¹)	$\Delta\tilde{\nu}$ (strain) (cm ⁻¹)	T_D (°K)	α (cm ⁻¹)
2.1	R ₁	760	1440	0	2.90	450	-177
	R ₂	760	640	0	3.10	450	-177
	N ₁	935	1681	0.20	6.73	450	-160
	N ₂	935	1166	0.24	3.06	450	-150
0.94	R ₁	760	1071	0.24	2.45	450	-177
	R ₂	760	475	0.36	2.30	450	-177
	N ₁	935	731	0.20	5.24	450	-160
	N ₂	935	777	0.20	2.14	450	-150
0.05*	R ₁	760	544	$\begin{Bmatrix} 0 \\ (0.004) \end{Bmatrix}$	0.096	760	-400
	R ₂	760	415	0	0.1	760	-400

*Data from McCumber and Sturge (1963); β_{R_1} from Kurnit, Abella, and Hartmann (1966); ($T_D = 935^\circ\text{K}$ from specific heat measurements).

Without the inclusion of this term the theoretical curve will deviate from the experimental curve most noticeably in the temperature range from 80°K up to 150°K . From independent measurements it was found that the excited levels within the R₁, N₁, and N₂ systems are thermalized (see Section 9). These results show that the relaxation processes within the N₁ and N₂ systems, although they allow for the thermalization of the levels, do not give any relevant contribution to the widths of the lines originating from the N₁ and N₂ levels. This fact implies that these processes are somewhat slower than the corresponding processes within the R levels.

The value of β obtained from this treatment gives lifetimes for the $S = 2$ state of the N₁ system and for the $S = 1$ state of the N₂ system of about 2.7×10^{-11} seconds. [Yen, Scott, and Scott (1965) found a value of 5.7×10^{-11} seconds for the lifetime of an energy level of Er^{+3} in LaF_3 , 51 cm^{-1} above the ground state.]

The $\bar{\alpha}$ coefficients for the N lines are greater in the 2.1% sample. For the four lines of the 2.1% sample, $\bar{\alpha}_{N_1} > \bar{\alpha}_{R_1} > \bar{\alpha}_{N_2} > \bar{\alpha}_{R_2}$ and for the 0.94%

sample $\bar{\alpha}_{R_1} > \bar{\alpha}_{N_2} > \bar{\alpha}_{N_1} > \bar{\alpha}_{R_2}$. The β_{ij} coefficients for both N lines of both samples are almost the same.

The Debye temperature used for the N linewidths is the same as the Debye temperature determined from specific heat measurements. The lower effective Debye temperature used for the R linewidths indicates that the single ions are affected more by lower frequency phonons.

The temperature dependence of the lineshifts was fitted in the following way. For both the samples all the curves shown in Figure 25 were fitted by using Eq. (106) with $T_D = 450^\circ\text{K}$ and all $\beta'_{ij} = 0$. The T_D used by McCumber and Sturge for the lineshift data in lightly doped ruby was 760°K . The α coefficients are all negative, which indicates a shift toward lower energy with increasing temperature. The α coefficients are the same for both samples and $|\alpha_{R_1}| = |\alpha_{R_2}| > |\alpha_{N_2}| > |\alpha_{N_1}|$. These are all smaller than the absolute values of the coefficients used by McCumber and Sturge.

9. RESULTS AND DISCUSSION OF RELATIVE INTENSITY MEASUREMENTS

Relative intensity measurements were made on the no-phonon lines of heavily doped ruby from 13°K up to 400°K . The purpose of these measurements was two-fold: (1) the establishment of energy level systems for Cr^{3+} pairs in ruby, and (2) the study of the interactions between single-ion and pair systems in crystals.

In order to establish the energy levels for the pair systems, the relative intensities of all the no-phonon lines of a sample with a 2.1% chromium (No. 3 in Table 5) were measured at various temperatures. For studying the energy transfer from single ions to pairs, the thermal dependences of the intensity ratios of the R and N lines were obtained for the 2.1% sample and a sample with 0.94% chromium (No. 2 in Table 5).

The experimental apparatus used was the continuous fluorescence equipment described in Section 4. The intensities of all the pair lines were obtained by scanning the continuous spectrum using a monochromator slit width of 20μ (see Figure 19). The results are listed in Table 15. The intensities of the R and N lines were obtained by scanning slowly over each line using various settings for the monochromator slit widths. The results are listed in Tables 16 and 17.

Table 15. Fluorescence Intensities of Pair Lines in Ruby with 2.1% Cr

λ (Å)	I at 16°K	I at 47.5°K	I at 92°K	I at 163°K
6948.56	----	4.63	8.96	18.05
6954.10	----	3.76	7.40	15.46
6964.13	----	3.51	5.36	9.60
6969.55	----	16.51	19.99	19.91
6978.37	----	12.00	19.69	26.98
6979.44	37.0	16.50	11.30	13.70
6987.74	----	61.08	39.46	31.76
6989.38	113.0	56.17	30.87	33.95
6996.80	41.7	20.01	14.35	17.33
7001.81	229.9	37.67	14.12	15.07
7008.84	1409.0	298.00	109.49	83.24
7029.50	33.5	13.42	5.36	---
7040.63	1305.0	599.00	187.07	70.27
7053.16	521.0	265.68	62.57	32.54

Resolution: 0.3Å

Table 16. Relative Intensities of the R and N Lines in Ruby with 2.1% Cr

T (°K)	$\frac{1}{T}$ (°K) ⁻¹	$\frac{I_{R1}}{I_{N1}}$	$\frac{I_{R1}}{I_{N2}}$	$\frac{I_{R2}}{I_{N1}}$	$\frac{I_{R2}}{I_{N2}}$	$\frac{I_{N2}}{I_{N1}}$
14	0.0755	0.02	0.02			0.874
21	0.0475			0.004	0.002	
29	0.0345	0.02	0.03			0.667
42	0.0235	0.04	0.07	0.018	0.033	0.546
62	0.0160					0.495
74	0.0135	1.18	0.21	0.055	0.113	0.574
80	0.0125	0.12	0.27			0.587
96	0.0105	0.33	0.70	0.166	0.254	0.654
117	0.0085	0.57	0.68	0.304	0.368	0.829
132	0.0075	0.73	0.83	0.437	0.500	0.875
155	0.0065	1.19	1.15	0.754	0.720	1.038
184	0.0055	2.14	1.80	1.099	0.924	1.190
301	0.0030	3.07	1.96	1.601	1.023	1.515
311	0.0030	3.45	2.87	1.609	1.340	1.201
400	0.0025	4.78	3.69	3.121	2.410	1.292

Resolution: 0.07Å for $T \leq 74^\circ\text{K}$
 0.15Å for $80^\circ\text{K} \leq T \leq 184^\circ\text{K}$
 0.30Å for $T \geq 301^\circ\text{K}$

Table 17. Relative Intensities of the R and N Lines in Ruby with 0.94% Cr

T (°K)	$\frac{1}{T} (^{\circ}\text{K})^{-1}$	$\frac{I_{R_1}}{I_{N_1}}$	$\frac{I_{R_1}}{I_{N_2}}$	$\frac{I_{R_2}}{I_{N_1}}$	$\frac{I_{R_2}}{I_{N_2}}$	$\frac{I_{N_2}}{I_{N_1}}$
20	0.0515	0.27	0.09	0.051	0.017	3.077
25	0.0390	0.23	0.09	0.074	0.029	2.528
47	0.0210	0.20	0.13	0.134	0.088	1.520
70	0.0145	0.31	0.29	0.201	0.019	1.049
82	0.0125	0.42	0.41	0.289	0.277	1.045
92	0.0110	0.46	0.47	0.367	0.376	0.986
108	0.0095	0.55	0.54	0.411	0.403	1.020
117	0.0085	0.83	0.68	0.534	0.436	1.227
128	0.0080	1.03	0.86	0.768	0.590	1.212
138	0.0070	1.28	1.08	0.798	0.681	1.189
148	0.0065	1.45	1.06	1.020	0.740	1.366
175	0.0055	1.62	1.62	1.125	1.136	1.000
178	0.0055	1.90	1.21	1.330	1.665	1.534
199	0.0050	2.26	2.43	1.555	1.670	0.931
224	0.0045	3.08	2.53	4.400	1.770	1.739
308	0.0030	5.67	4.66	4.680	7.080	1.806

Resolution: 0.07\AA for $T \leq 69.5^{\circ}\text{K}$
 0.15\AA for $T \geq 81.5^{\circ}\text{K}$

9.1 Construction of the Energy Level Systems and Assignments of Transitions

As was mentioned in Section 2, Kisliuk and Krupke (1965) used Daly's (1961) monochromatic excitation data and the recurrence of previously established ground state splittings (Kisliuk et al., 1964) to construct energy level diagrams and assign observed lines to transitions within the second and fourth nearest neighbor pair systems. From the measurements of the relative intensities of the fluorescence lines, it was possible to establish similar energy level diagrams for the two pair systems and assign the observed lines to specific transitions. Two facts were used in interpreting the results of the relative intensity measurements: (1) the intensities of the fluorescence lines originating from the same level have the same temperature dependence, and (2) the intensities of the fluorescence lines originating from different levels in thermal equilibrium obey the relationship

$$\frac{I_1}{I_2} = \text{Const.} \times \exp\left(\frac{-\Delta E_{12}}{KT}\right). \quad (107)$$

The relative intensities of the R and N lines listed in Tables 16 and 17 are plotted versus $1/T$ in Figure 27. At high temperatures, these results show that

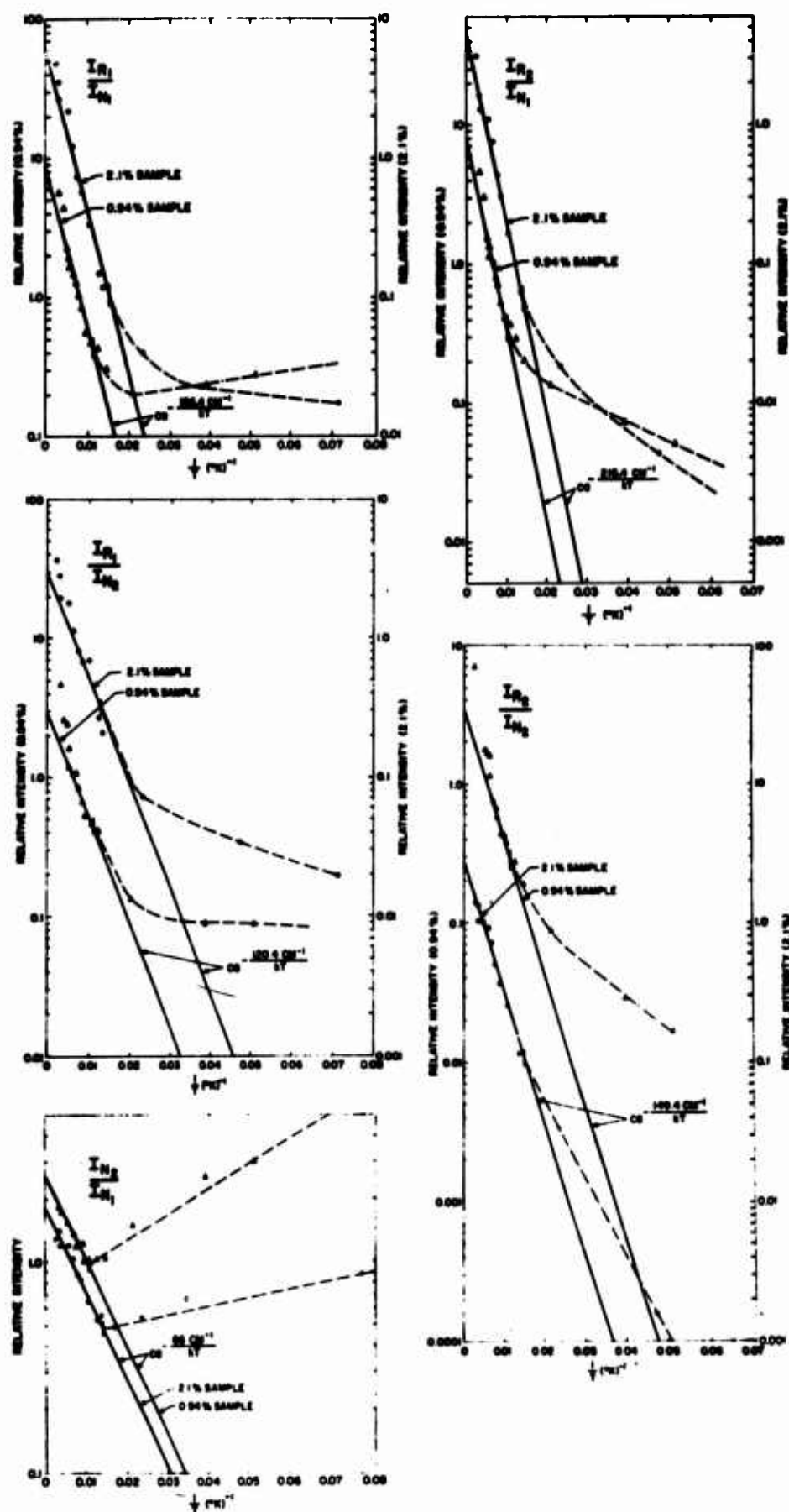


Figure 27. Relative Intensities of the R and N Fluorescence Lines in Ruby with 2.1% and 0.94% Chromium

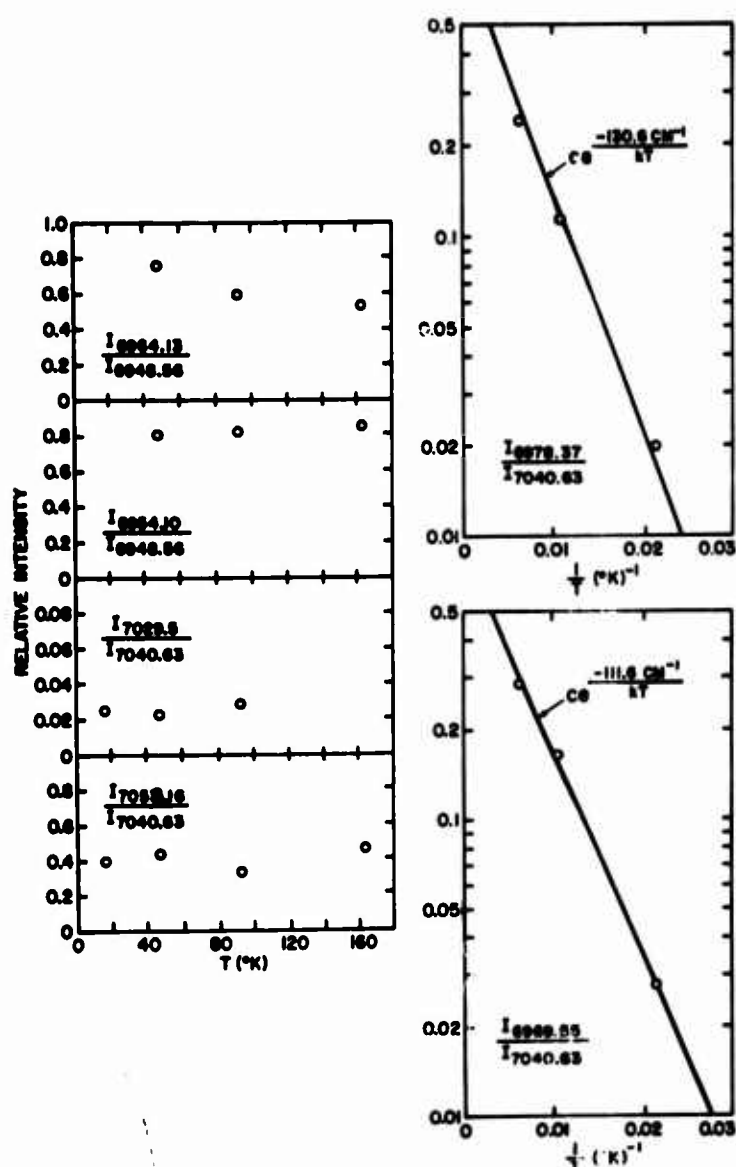


Figure 28. Relative Intensities of Second Nearest Neighbor Pair Lines in Ruby

with constant intensities relative to these lines established by thermalization were assigned to specific transitions. This fixed the ground-state levels marked with A. Three or more lines having the same temperature dependence and differing in energy by amounts equal to certain ground state splittings were used to establish the excited states marked with B. A number of other observed lines which were not well enough resolved to obtain an accurate temperature dependence were assigned to specific transitions by considering their qualitative change with temperature and

the R_1 , R_2 , N_1 , and N_2 metastable levels are in thermal equilibrium. The deviation of these intensity ratios from a Boltzmann dependence at low temperatures is discussed in the next section. The temperature dependences of the relative intensities of the various other pair lines listed in Table 15 are shown in Figures 28 and 29. From the results shown in these three figures, the energy levels for the two pair systems can be established and pair lines can be assigned to specific transitions. The results are shown in Figure 30.

Starting with the well-known R line transitions, thermalization of relative intensities fixed the levels involved in the N_1 and N_2 transitions. These and other pair levels established by thermalization measurements are indicated by a T. Then, lines

the established energy splittings (see Table 6). These assignments, although based mainly on those lines whose temperature dependences could be measured accurately, established the energy level scheme on a firmer ground.

The results obtained are consistent with those of Kisliuk and Krupke (1965). For the N_1 pair, four ground state levels and the four excited state levels were established.

Twelve lines were assigned to transitions between various sets

of levels in this system. One of them, the 6978.4 Å line, was not assigned by previous workers.

The more closely spaced levels belonging to the N_2 pair system made accurate intensity measurements more difficult for these lines. For this system, only three of the four levels of the ground state and three of the six levels of the excited state were firmly fixed. The other levels established by Kisliuk and Krupke are marked by K. Also, only twelve transitions were assigned within the N_2 system where Kisliuk and Krupke assigned eighteen.

At least seven lines not assigned previously were observed near the R lines (see Table 6). These lines are too closely spaced to obtain accurate intensity measurements. However, by virtue of their general change with temperature and their energy splittings compared with the ground states of the pair systems, it seems quite reasonable to assign at least three of these lines to specific transitions. These transitions establish a new excited state level in the N_2 pair system which falls between the R_1 and R_2 metastable levels and is marked by a D in Figure 30. This is consistent with the observation by Daly (1961) of fluorescence at the N_2 line while exciting at a frequency between the R_1 and R_2 lines. The position of this new level may be useful in explaining the energy transfer between single ions and pairs as discussed in the following section.

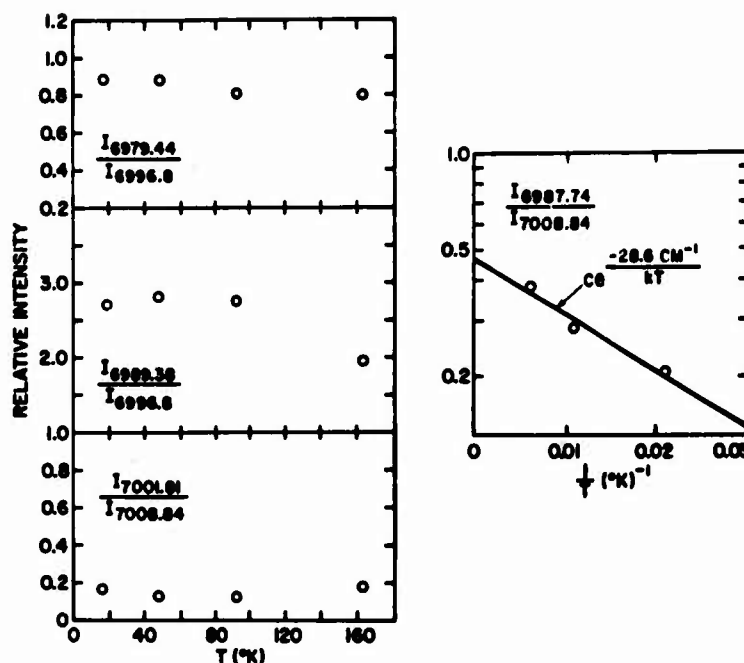


Figure 29. Relative Intensities of Fourth Nearest Neighbor Pair Lines in Ruby

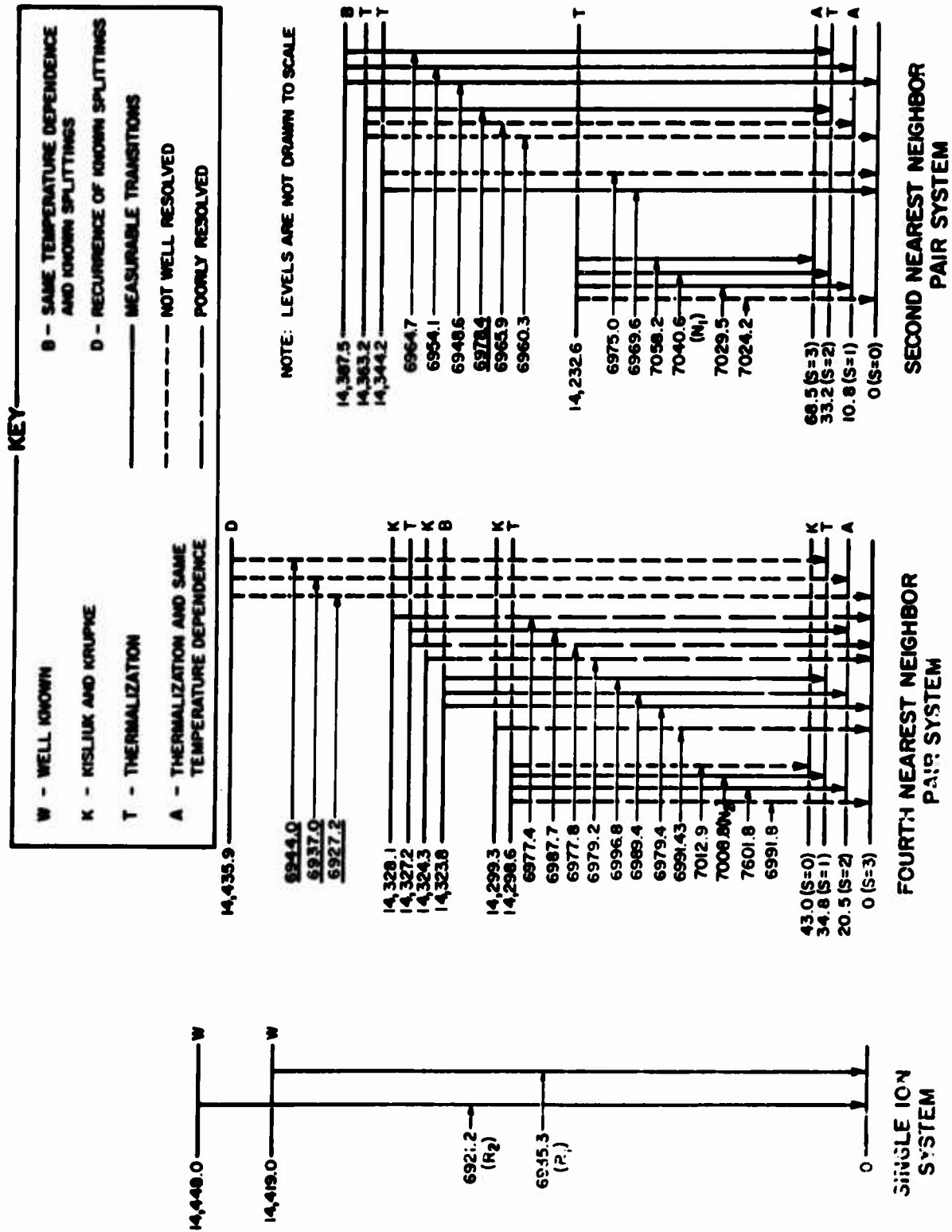


Figure 30. Energy Levels and Transitions of Single Ion and Pair Systems in Ruby

9.2 Energy Transfer Between Single-Ion and Pair Systems: Relative Intensities of the R and N Lines

As mentioned in Section 2, the transfer of energy from single ions to pairs has been observed in various ways. Schawlow and co-workers (1959) first suggested the presence of energy transfer from single ions to pairs because the increase in the relative intensity of the N_2 line to the R_1 line as a function of concentration was observed to be greater than linear above about 0.3% chromium. Wieder and Sarles (1961) excited a sample of heavily-doped ruby with the R_1 emission of a ruby laser and observed the fluorescence in the N lines thus explicitly demonstrating the energy transfer from single ions to pairs. Imbusch (1966) investigated this energy transfer by measuring the lifetimes at the R and N lines. He concluded that the energy transfer comes from the main body of chromium ions and not just from the ions located near the pairs. He also found that this transfer becomes very efficient at concentrations of about 1.0% Cr_2O_3 .

The relative intensities of the R_1 , R_2 , N_1 , and N_2 lines shown in Figure 27 also contain information about the coupling of the single ion and pair systems. These curves for the two samples are indicative of the temperature and concentration dependence of the energy transfer mechanism. The fact that the departure from thermalization occurs at a higher temperature in the 0.94% sample than in the 2.1% sample and that for each line the amount of deviation from thermalization is greater in the less doped sample shows that the coupling of the R and N systems is greater for the more heavily doped sample. The deviation from thermalization occurs at about 68°K for the 2.1% sample and 91°K for the 0.94% sample. The intensities of the lines within each pair system are observed to remain thermalized even at low temperature, thus giving additional evidence of the existence of separate systems.

One possible mechanism which can explain the observed characteristics of the energy transfer between the R, N_1 , and N_2 systems is cross-relaxation, which implies that a transition in one direction in one system is accompanied by a transition in the opposite direction in another system. Any energy mismatch of the two transitions can be balanced by phonon processes. The level in the N_2 pair system which was found between the R_1 and R_2 excited levels could be used with minimum energy mismatch in cross-relaxation between single-ion and pair systems. We also notice that the N_1 line was observed in fluorescence by Daly (1961) when excited at a level slightly above the R_2 level. This result is consistent with the excitation measurements reported in Section 7. This level could play a role in the energy transfer between the R and the N_1 systems with minimum energy mismatch. The nature of this transfer mechanism has been investigated by Imbusch (1966) who noted some experimental findings of its quadrupole-quadrupole character. Our experimental evidence that the R and N levels are thermalized over a range of

temperatures is an additional proof that the transfer is nonradiative.

Consider the simplified model of cross-relaxation between two systems of ions shown in Figure 31 where systems A and B represent the R and N systems, respectively. The rate equations for the populations of the various levels can be written as follows (Seigman, 1964):

$$\left. \begin{aligned} \dot{N}_2 &= WN_1 - A_{21}N_2 + n_2N_1 \frac{\omega'_{cr}}{n} - N_2n_1 \frac{\omega_{cr}}{n} \\ \dot{N}_1 &= -\dot{N}_2 \end{aligned} \right\} \quad (108)$$

$$\left. \begin{aligned} \dot{n}_2 &= -n_2 A'_{21} - n_2N_1 \frac{\omega'_{cr}}{n} + N_2n_1 \frac{\omega_{cr}}{n} \\ \dot{n}_1 &= -\dot{n}_2 \end{aligned} \right\} \quad (109)$$

In the above equations, the assumptions have been made that the radiationless decay from the absorption band in system A to level 2 is extremely fast and that system B is pumped only through cross-relaxation from system A. Cross-relaxation between the two systems in the simple scheme shown in Figure 31 can take place only with the assistance of phonons of energy equal to the energy gap between level 2 of system A and level 2 of system B, designated ΔE_{22} . Because of this

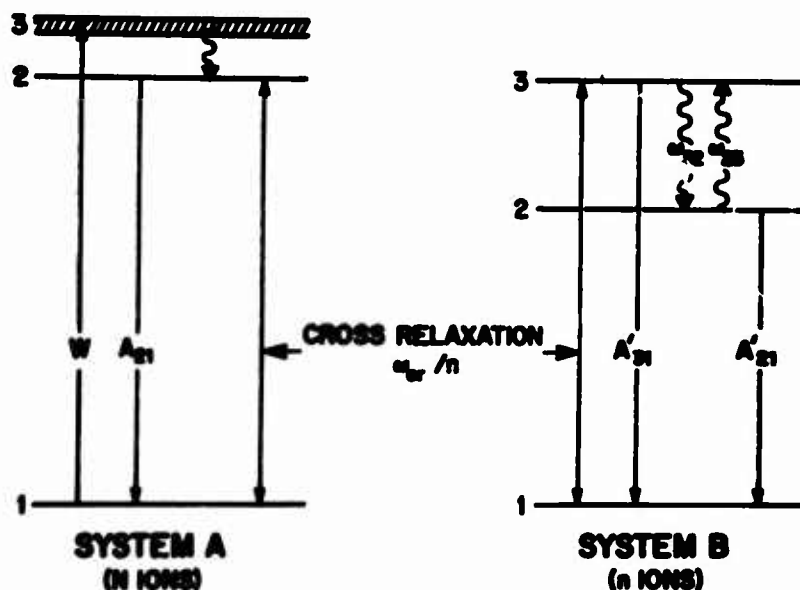


Figure 31. Cross-relaxation Between Two Fluorescent Systems

emission and absorption of phonons concurrent with the cross-relaxation process, we may expect that

$$\frac{\omega_{cr}}{\omega'_{cr}} = e^{-\Delta E_{22}/KT}. \quad (110)$$

The more complicated scheme having an additional level 3 in system B with about the same energy of level 2 of system A would require the presence of phonon excitation and relaxation processes between levels 2 and 3 of B, resulting in a similar temperature dependence of the cross-relaxation probabilities.

Equations (108) and (109) can be solved for equilibrium conditions with the assumptions that $N_1 \simeq N$ and $n_1 \simeq n$. The results are

$$\begin{aligned} n_2 &= \frac{\omega_{cr} WN}{\left(A'_{21} + \frac{N}{n} \omega'_{cr}\right) \left(A_{21} + \omega_{cr}\right) - \frac{N}{n} \omega'_{cr} \omega_{cr}} \\ N_2 &= \frac{\left(A'_{21} + \frac{N}{n} \omega'_{cr}\right) WN}{\left(A'_{21} + \frac{N}{n} \omega'_{cr}\right) \left(A_{21} + \omega_{cr}\right) - \frac{N}{n} \omega'_{cr} \omega_{cr}} \end{aligned} \quad (111)$$

$$\therefore \frac{N_2}{n_2} = \frac{A'_{21}}{\omega_{cr}} + \frac{N}{n} \frac{\omega'_{cr}}{\omega_{cr}}. \quad (112)$$

The intensity of a fluorescence line is proportional to the population of the level from which it originates. Thus, Eq. (112) should explain the relative intensity curves shown in Figure 27. At high temperatures, the observed thermalization of the R and N levels, as seen in Figure 27, implies that $A'_{21} \ll \omega'_{cr} \frac{N}{n}$. In Eq. (112), the second term is predominant. Substituting Eq. (110) into Eq. (112) gives (for high temperatures)

$$\frac{N_2}{n_2} = \frac{N}{n} e^{-\Delta E_{22}/KT}. \quad (113)$$

This indicates that the ratio I_R/I_N will be proportional to a Boltzmann factor at high temperatures as observed experimentally. It also predicts that I_R/I_N should be greater for the less concentrated sample; this concurs with the experimental results.

At low temperatures, ω'_{cr} is expected to be very small and the first term in Eq. (112) is predominant. In this region, I_R/I_N will be proportional to

$$\frac{N_2}{n_2} = \frac{A'_{21}}{\omega_{cr}}. \quad (114)$$

The temperature variation in this region may be considered to be due mainly to the variation of ω_{cr} . The relevant times for the cross pumping can be seen from Figure 27 to be in the order

$$\tau_{cr}(R_1 \rightarrow N_1) > \tau_{cr}(R_1 \rightarrow N_2) > \tau_{cr}(R_2 \rightarrow N_1) > \tau_{cr}(R_2 \rightarrow N_2), \quad (115)$$

where $\tau_{cr}^{-1} = \omega_{cr}$. The above relation implies that, at low temperatures, the N_1 level is pumped less than the N_2 level; this agrees with the dependence of the I_{N_2}/I_{N_1} ratio on temperature (see Figure 27). This relation also implies that the pumping of the N levels through the R_2 level is more efficient than pumping through the R_1 level.

In the above considerations, it is assumed that direct pumping of the N levels from the absorption bands affects both N levels by the same amount. Evidence of direct pumping from the bands is found from fluorescent lifetime measurements and is discussed in the next section.

10. RESULTS AND DISCUSSION OF FLUORESCENT LIFETIME MEASUREMENTS

Fluorescence decay measurements were made on three ruby samples from 13°K up to 700°K. Measurements were made at the R_1 line of a sample with 0.03% chromium (No. 1 in Table 5) and at the R_1 , R_2 , N_1 , and N_2 lines and the 7750 Å band in the 0.94% and 2.1% samples listed as Nos. 2 and 3 in Table 5, respectively. The comparison of the results for the three samples gives more information about the energy transfer from single ions to pairs.

The experimental apparatus used for these measurements was described in Section 4. The time resolution of the apparatus was about 13 μsec. Five pictures were taken of each fluorescence decay and an average decay time was determined.

10.1 Experimental Results

The measured lifetimes at the R_1 line of the 0.03% sample are listed in Table 18. They are plotted versus temperature in Figure 32 along with the results obtained by Nelson and Sturge (1965) for very thin, dilute samples with negligible

reabsorption lengthening. The rapid decrease in the lifetime above 300°K is due to the increasing importance of vibronic processes. Below this temperature the lifetimes of the 0.03% sample are observed to be lengthened due to reabsorption (Varsanyi et al., 1959).

Table 18. Fluorescent Lifetimes at the R_1 Line in Ruby with 0.03%Cr

T (°K)	τ_{R_1} (msec)
14	10.57
52	10.98
80	9.95
104	9.06
129	7.60
148	6.74
166	6.40
185	5.64
250	4.44
260	4.15
300	3.90
406	2.27
540	0.72
694	0.08

The decay times measured at the R_1 , R_2 , N_1 , and N_2 lines of the 2.1% and 0.94% samples are listed in Tables 19 and 20, respectively. They are shown plotted versus T in Figure 33.

For temperatures in the thermalization range all the lines present a purely exponential decay with the same time constants. For the 2.1% sample all the lifetimes coincide and increase from 0.04 msec at 700°K to 2 msec at 350°K and decrease as the temperature is lowered further. For the 0.94% sample all the lifetimes coincide and increase from 700°K to a maximum of 3.5 msec at 250°K and decrease slightly as the temperature is lowered further.

At temperatures lower than the one at which thermalization ceases (68°K for 2.1% sample and 91°K for 0.94% sample) the R lines continue to present a purely exponential decay whereas the N lines present an initial rise in their fluorescence. The time t_{\max} at which the maximum occurs increases as the temperature is lowered and is larger for the 0.94% sample. The values of t_{\max} are given in Table 21. The experimentally observed decay times, shown in Figure 33 for N_1 and N_2 at low temperatures, are the decay times of the tail occurring after the initial rise.

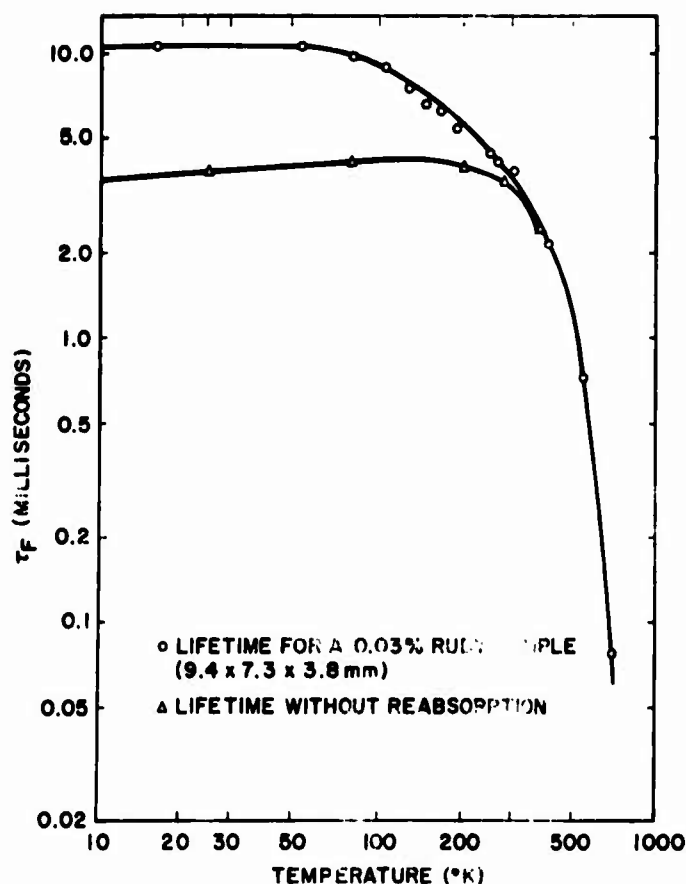


Figure 32. Fluorescent Lifetimes at the R_1 Lines of Ruby (3.76 mm) with 0.03% Chromium. The results shown for negligible reabsorption are from the data of Nelson and Sturge (1965)

lifetime measurements shown in Figures 32 to 34 are consistent with results obtained previously by Tolstoi and Tkachuk (1959). The change in the lifetime at the R lines with concentration is consistent with the results reported by Deutschbein (1962) and by Brown (1964) at 300°K and 77°K.

10.2 Interpretation of Results

The results of the lifetime measurements give further information about the energy transfer from single ions to pairs. The fact that for both heavily doped samples all the lifetimes coincide at high temperatures where pure exponential decays were observed indicates that the upper levels of the various transitions are in thermal equilibrium. The deviation of the decays of the N lines and 7750 Å band from pure exponentials at low temperatures indicates that thermalization no longer exists. These observations are consistent with the results of the relative intensity measurements discussed in the previous section.

The lifetimes at the band near 7750 Å are also listed in Tables 19 and 20 and are shown in Figure 34. Above 400°K the lifetimes coincide with those at the R lines. Below this temperature a double decay is observed in the 0.94% sample with the longer lifetime equal to that at the R lines. For the 2.1% sample an initial rise in the fluorescence is observed with the tail of the fluorescence showing a decay time equal to the lifetime at the R line. Also in this case t_{\max} increases as the temperature is lowered (see Table 21). The decay times shown in Figure 34 for the 2.1% sample at low temperatures are the decay times of the fluorescence tail.

Figure 35 shows typical pictures for the various types of decays. The results of the

Table 19. Fluorescent Lifetimes in Ruby with 2.1% Cr

T (°K)	τ_{R_1} (msec)	τ_{R_2} (msec)	τ_{N_1} (msec)	τ_{N_2} (msec)	$\tau_{7750\text{\AA}}$ (msec)
10	0.63		1.48	0.93	0.66
13	0.59		1.49	0.84	0.60
39	0.69	0.69	1.35	0.41	0.66
55	0.66	6.73	1.10	0.83	0.70
73	0.60	0.63	0.98	0.79	0.67
84	0.64	0.62	0.86	0.75	0.69
107	0.71	0.76	0.79	0.73	0.65
123	0.78	0.80	0.82	0.76	0.75
140	0.81		0.74	0.75	0.70
166	0.94	0.95	0.88	0.95	0.87
178	1.04	1.06	1.04	0.97	0.97
207	1.23	1.23	1.17	1.23	1.13
231	1.33	1.29	1.28	1.21	1.22
251	1.33		1.37	1.32	1.26
281	1.63	1.62	1.55	1.61	1.41
298	1.63	1.71	1.49	1.55	1.53
300	1.85		1.85	1.75	1.61
405	1.87		1.85	1.90	1.80
537	1.16		1.17	1.11	1.00
712	0.04		0.04	0.04	0.04

Table 20. Fluorescent Lifetimes in Ruby with 0.94% Cr

T (°K)	τ_{R_1} (msec)	τ_{R_2} (msec)	τ_{N_1} (msec)	τ_{N_2} (msec)	$\tau_{7750\text{\AA}}$ (msec)
15	2.53	2.50	2.84	2.73	1.29, 2.17
37	2.56	2.56	2.85	2.63	1.30, 2.31
65	2.60	2.60	2.83	2.76	1.62, 2.61
81	2.60	2.63	2.81	2.76	1.70, 2.56
93	2.60	2.68	2.85	2.66	1.68, 2.40
104	2.61	2.61	2.80	2.82	1.71, 2.44
114	2.61	2.73	2.89	2.82	1.89, 2.58
128	3.00	3.03	2.96	3.00	2.05, 2.87
140	3.00	3.00	2.88	2.91	1.72, 2.88
160	3.06	3.11	2.91	2.92	2.03, 3.18
181	3.20	3.17	2.91	2.90	1.95, 2.96
207	3.32	3.30	3.03	2.99	2.06, 3.25
235	3.42	3.38	3.31	3.25	1.78, 3.15
252	3.56	3.57	3.34	3.33	1.93, 3.41
296	3.21	3.22	3.00	3.05	1.92, 3.21
350	3.68	3.68	3.32	3.22	2.00, 3.12
400	2.81	2.86	2.70	2.77	2.25
450	2.08	2.03	2.02	2.00	1.90
500	1.47	1.50	1.50	1.50	1.44
578	0.52	0.52	0.42	0.52	0.60
670	0.17	0.22	0.16	0.16	0.14

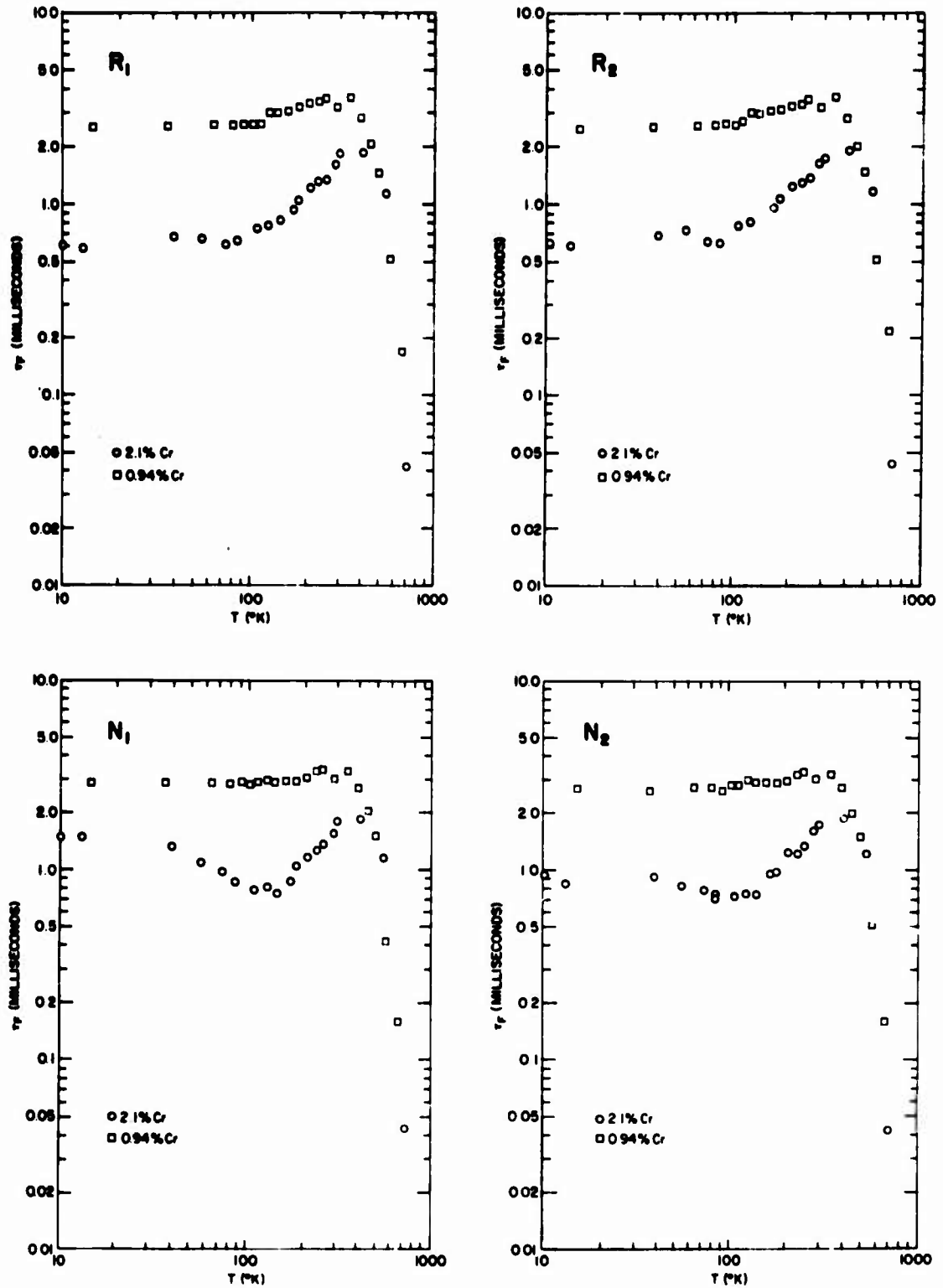


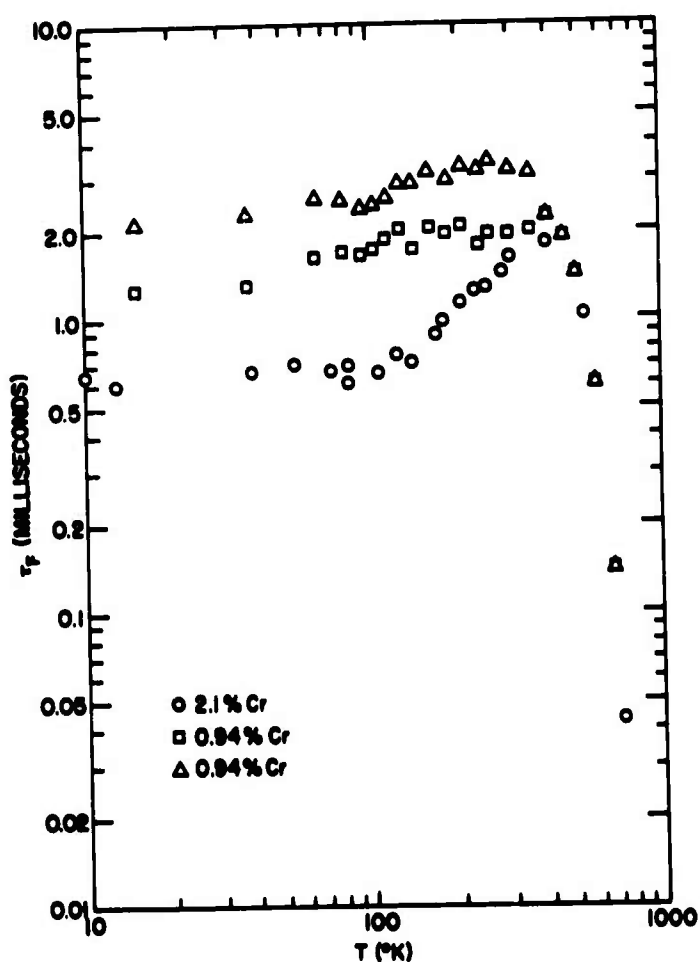
Figure 33. Fluorescent Lifetimes at the R and N Lines in Ruby with 2.1% Chromium (4.26 mm) and 0.94% Chromium (0.97 mm). For the N lines below 100°K for the 0.94% sample and 77°K for the 2.1% sample the experimental points are the decay times after an initial rise in fluorescence

Table 21. Measured Values of t_{\max}

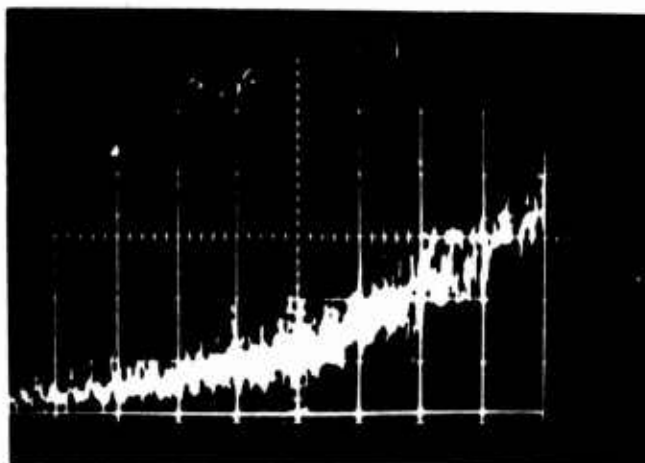
Sample (% Cr)	T ($^{\circ}$ K)	t_{\max} (sec)		
		N_1	N_2	7750 \AA
2.1	10	0.11×10^{-3}	0.07×10^{-3}	0.03×10^{-3}
	80	0	0	0.03×10^{-3}
	300	0	0	0
0.94	15	0.27×10^{-3}	0.26×10^{-3}	Double Decay
	77	0.25×10^{-3}	0.25×10^{-3}	
	102	0.14×10^{-3}	0.10×10^{-3}	
	112	0.14×10^{-3}	0	

Accuracy: $\pm 0.03 \times 10^{-3}$ sec

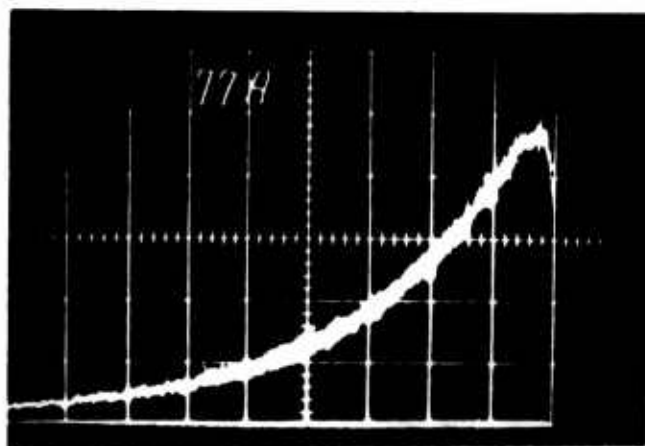
Figure 34. Fluorescent Life-times at the 7750 \AA Band in Ruby with 2.1% Chromium (4.26 mm) and 0.94% Chromium (0.97 mm). Below 300 $^{\circ}$ K the experimental points for the 2.1% sample are the decay times after an initial rise in fluorescence. The 0.94% sample has a double decay below 400 $^{\circ}$ K



(a)



(b)



(c)

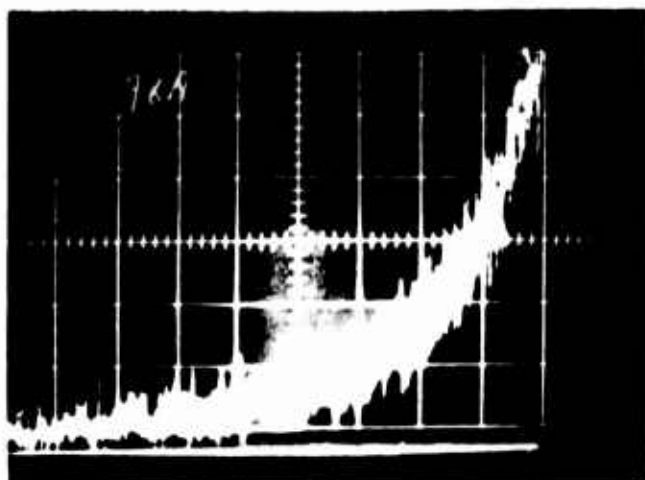


Figure 35. Examples of Different Types of Decays: (a) Pure Exponential Decay, (b) Initial Rise, (c) Double Decay. The pulse duration used to obtain these pictures was about $13 \mu\text{sec}$

The thermal dependence of the lifetimes of heavily doped ruby in the temperature range where the systems are thermalized can be explained as follows. Consider the two fluorescence systems interacting through cross-relaxation shown in Figure 31. The rate equations for the populations of these levels were given in Eqs. (108) and (109) as

$$\left. \begin{aligned} \dot{N}_2 &= WN - A_{21}N_2 + n_2 \frac{N}{n} \omega'_{cr} - N_2 \omega_{cr} \\ \dot{n}_2 &= -n_2 A'_{21} - n_2 \frac{N}{n} \omega'_{cr} + N_2 \omega_{cr} \end{aligned} \right\}, \quad (116)$$

where the assumptions have again been made that $N_1 \simeq N$ and $n_1 \simeq n$. Taking the time at the end of the exciting pulse to be $t = 0$, the Laplace transforms of these equations for $t > 0$ are

$$\left. \begin{aligned} S\bar{N}_2 - N_2(0) &= -\beta\bar{N}_2 + p'_{cr}\bar{n}_2 \\ S\bar{n}_2 - n_2(0) &= p_{cr}\bar{N}_2 - \alpha\bar{n}_2 \end{aligned} \right\}, \quad (117)$$

where

$$\left. \begin{aligned} \alpha &= \frac{N}{n} \omega'_{cr} + A'_{21} = p'_{cr} + A'_{21} \\ \beta &= \omega_{cr} + A_{21} = p_{cr} + A_{21} \end{aligned} \right\}, \quad (118)$$

$$p_{cr} = \omega_{cr}$$

$$p'_{cr} = \omega'_{cr} \frac{N}{n}.$$

The Laplace transform of n_2 is \bar{n}_2 .

The value of n_2 at the end of the exciting pulse is $n_2(0)$.

Equations (117) can be solved to give

$$\left. \begin{aligned} \bar{N}_2 &= \frac{N_2(0)(S+\alpha) + n_2(0)p'_{cr}}{(S+\alpha)(S+\beta) - p_{cr}p'_{cr}} = \frac{N_2(0)(S+\alpha) + n_2(0)p'_{cr}}{(S-S_1)(S-S_2)} \\ \bar{n}_2 &= \frac{N_2(0)p_{cr} + n_2(0)(S+\beta)}{(S+\alpha)(S+\beta) - p_{cr}p'_{cr}} = \frac{N_2(0)p_{cr} + n_2(0)(S+\beta)}{(S-S_1)(S-S_2)} \end{aligned} \right\} \quad (119)$$

where S_1 and S_2 are the roots of the equation

$$(S + \alpha)(S + \beta) - p_{cr} p'_{cr} = S^2 + (\alpha + \beta)S + (\alpha\beta - p_{cr} p'_{cr}) = 0. \quad (120)$$

This has the solution

$$S = \frac{-(\alpha + \beta) \pm \sqrt{(\alpha + \beta)^2 - 4(\alpha\beta - p_{cr} p'_{cr})}}{2}. \quad (121)$$

The right-hand sides of Eq. (119) can be separated into two parts by means of partial fractions. The results are

$$\begin{aligned} N_2 &= \left[\frac{N_2(0)(S_1 + \alpha) + n_2(0)p'_{cr}}{S_1 - S_2} \right] \frac{1}{S - S_1} \\ &+ \left[\frac{N_2(0)(S_2 + \alpha) + n_2(0)p'_{cr}}{S_2 - S_1} \right] \frac{1}{S - S_2} \\ \bar{n}_2 &= \left[\frac{n_2(0)(S_1 + \beta) + N_2(0)p_{cr}}{S_1 - S_2} \right] \frac{1}{S - S_1} \\ &+ \left[\frac{n_2(0)(S_2 + \beta) + N_2(0)p_{cr}}{S_2 - S_1} \right] \frac{1}{S - S_2}. \end{aligned} \quad (122)$$

The inverse Laplace transforms of these equations are

$$\begin{aligned} N_2(t) &= \frac{N_2(0)(S_1 + \alpha) + n_2(0)p'_{cr}}{S_1 - S_2} e^{S_1 t} \\ &+ \frac{N_2(0)(S_2 + \alpha) + n_2(0)p'_{cr}}{S_2 - S_1} e^{S_2 t} \\ n_2(t) &= \frac{n_2(0)(S_1 + \beta) + N_2(0)p_{cr}}{S_1 - S_2} e^{S_1 t} \\ &+ \frac{n_2(0)(S_2 + \beta) + N_2(0)p_{cr}}{S_2 - S_1} e^{S_2 t}. \end{aligned} \quad (123)$$

Now consider the situation when the radiationless transitions between the excited levels are much more probable than radiative transitions to the ground state, that is,

$$p_{cr}, p'_{cr} \gg A_{21}, A'_{21} \quad (124)$$

In this case S_1 and S_2 can be found expanding the radical in Eq. (121).

$$\begin{aligned} S &\approx -\frac{(\alpha + \beta)}{2} \pm \frac{(\alpha + \beta)}{2} \left[1 \pm 2 \frac{A'_{21} p_{cr} + A_{21} p'_{cr}}{(\alpha + \beta)^2} \right] \\ \therefore S_1 &\approx -\left(\frac{A'_{21} p_{cr} + A_{21} p'_{cr}}{p'_{cr} + p_{cr}} \right) \\ S_2 &\approx -(p'_{cr} + p_{cr}). \end{aligned} \quad (125)$$

Substituting these values into Eq. (123) gives

$$\begin{aligned} N_2(t) &= \left[\frac{N_2(0) p'_{cr} + n_2(0) p_{cr}}{p_{cr} + p'_{cr}} \right] e^{-pt} \\ &\quad - \left[\frac{n_2(0) p'_{cr} - N_2(0) p_{cr}}{p_{cr} + p'_{cr}} \right] e^{-(p_{cr} + p'_{cr})t} \\ n_2(t) &= \left[\frac{n_2(0) p_{cr} + N_2(0) p'_{cr}}{p_{cr} + p'_{cr}} \right] e^{-pt} \\ &\quad - \left[\frac{N_2(0) p_{cr} - n_2(0) p'_{cr}}{p_{cr} + p'_{cr}} \right] e^{-(p_{cr} + p'_{cr})t} \end{aligned} \quad (126)$$

where

$$p = \frac{A'_{21} p_{cr} + A_{21} p'_{cr}}{p'_{cr} + p_{cr}} \quad (127)$$

If a Boltzmann distribution has been established in the two metastable levels by the time $t = 0$, then

$$\frac{N_2(0)}{n_2(0)} = \frac{p'_{cr}}{p_{cr}} = \frac{N}{n} e^{-\Delta E_{22}/KT} \quad (128)$$

Substituting this into Eq. (126) gives

$$\left. \begin{aligned} N_2(t) &= N_2(0) e^{-pt} \\ n_2(t) &= n_2(0) e^{-pt} \end{aligned} \right\} \quad (129)$$

where p is given by (127). This shows that levels in thermal equilibrium decay with the same decay time. This common decay time can be written as

$$p = \frac{1}{\tau} = \frac{1}{\tau_N} \frac{\frac{n}{N} e^{\Delta E_{22}/KT}}{1 + \frac{n}{N} e^{\Delta E_{22}/KT}} + \frac{1}{\tau_R} \frac{1}{1 + \frac{n}{N} e^{\Delta E_{22}/KT}} \quad (130)$$

where

$$\tau_N^{-1} = A'_{21} \quad ,$$

$$\tau_R^{-1} = A_{21} \quad .$$

Using Eq. (128), Eq. (130) can also be expressed as

$$\frac{1}{\tau} = \frac{1}{\tau_N} \frac{n_2(0)}{N_2(0) + n_2(0)} + \frac{1}{\tau_R} \frac{N_2(0)}{N_2(0) + n_2(0)} \quad .$$

Thus,

$$\frac{1}{\tau_{R+N}} \propto \frac{n_R(0)}{\tau_R} + \frac{n_N(0)}{\tau_N} = n_R(0) \left(\frac{1}{\tau_R} + \frac{n_N(0)}{n_R(0)} \frac{1}{\tau_N} \right) \quad (131)$$

Thus, the lifetime of the coupled system will depend on concentration and temperature. The intrinsic lifetimes of the N_1 and N_2 lines at 77°K are 1.3 msec and 1.1 msec, respectively (Imbusch, 1966). These lifetimes are even smaller between 400°K and 100°K. On the other hand the R lifetime is larger and goes from 2 msec at 400°K to 4.2 msec at 100°K (Nelson and Sturge, 1965). As the temperature is lowered n_N increases and the lifetime of the coupled R+N states comes closer to the intrinsic values of the N states; this explains the decrease of

the lifetimes in the 400°K to 100°K range (see Figure 33). It also explains why the sample with less concentration has a smaller decrease after its maximum; this is because more of the population resides in the R levels in this sample than in the more heavily doped sample.

The behavior of the lifetimes at temperatures lower than the one at which thermalization ceases may be explained by using the rate equations given in (116) by letting $\omega'_{cr} \sim 0$.

$$\dot{N}_2 = -(\omega_{cr} + A_{21}) N_2 + WN \quad (132)$$

$$\dot{n}_2 = \omega_{cr} N_2 - A'_{21} n_2 \quad (133)$$

Again taking the time at the end of the pulse to be $t = 0$, the solution for Eq. (132) at $t > 0$ is:

$$N_2(t) = N_2(0) e^{-p_3 t}, \quad (134)$$

where $p_3 = \omega_{cr} + A_{21}$.

Substituting this into Eq. (133) and taking the Laplace transform gives

$$S\bar{n}_2 - n_2(0) = \frac{\omega_{cr} N_2(0)}{S + p_3} - A'_{21} \bar{n}_2$$

or

$$\bar{n}_2 = \frac{n_2(0)}{S + A'_{21}} + \frac{p_3 N_2(0)}{(S + p_3)(S + A'_{21})}$$

Taking the inverse Laplace transform of this expression gives

$$n_2(t) = \left[n_2(0) + \frac{\omega_{cr} N_2(0)}{p_3 A'_{21}} \right] e^{-A'_{21} t} - \frac{\omega_{cr} N_2(0)}{p_3 - A'_{21}} e^{-p_3 t} \quad (135)$$

Two cases are of interest:

A. Initial Rise

If the pulse is short enough a maximum can occur for $n_2(t)$ at a time t_{\max} after the end of the pulse. This is found by setting

$$\dot{n}_2(t)_{\max} = 0$$

$$\begin{aligned} \dot{n}_2(t_{\max}) = & \left[n_2(0) + \frac{\omega_{cr} N_2(0)}{p_3 - A'_{21}} \right] (-A'_{21}) e^{-A'_{21} t_{\max}} \\ & + \frac{\omega_{cr} p_3 N_2(0)}{p_3 - A'_{21}} e^{-p_3 t_{\max}} = 0 \end{aligned}$$

$$\therefore e^{-(p_3 - A'_{21}) t_{\max}} = \frac{A'_{21} n_2(0) + \frac{\omega_{cr} A'_{21} N_2(0)}{p_3 - A'_{21}}}{\frac{p_3 \omega_{cr}}{p_3 - A'_{21}} N_2(0)}$$

or

$$t_{\max} = \frac{1}{A'_{21} - p_3} \ln \left[\frac{A'_{21}}{p_3} + \frac{A'_{21} (p_3 - A'_{21})}{p_3 \omega_{cr}} \left(\frac{n_2(0)}{N_2(0)} \right) \right]. \quad (136)$$

The condition of obtaining an initial rise can be determined by finding \dot{n}_2 at the end of the pulse. This will be the slope of the initial decay which will be a positive number for an initial rise and a negative number otherwise.

$$\dot{n}_2(0) = -n_2(0) A'_{21} + \omega_{cr} N_2(0). \quad (137)$$

Thus the condition for an initial rise is

$$A'_{21} < \frac{\omega_{cr} N_2(0)}{n_2(0)}. \quad (138)$$

B. Double Decay

$$A'_{21} > p_3, \quad n_2(0) > \frac{\omega_{cr} N_2(0)}{A'_{21} - p_3}.$$

In this case Eq. (135) reduces to

$$n_2(t) = A e^{-t/\tau_N} + B e^{-t/\tau_R}, \quad (139)$$

where A and B are both positive, $\tau_N^{-1} = A'_{21}$ and $\tau_R^{-1} = p_3$.

The lifetime of the R levels in the 2.1% and 0.94% samples at low temperature is shorter than its intrinsic value (Nelson and Sturge, 1965). This fact is due to the presence of energy transfer even at low temperatures as confirmed by the smaller value that this lifetime has at high concentration. At high temperatures the cross-relaxation processes are active only in creating a thermalization condition and the measured lifetime is the lifetime of the coupled systems. On the other hand, at low temperatures where the R and N systems are decoupled, τ_R tends to $(\omega_{cr} + A_{21})^{-1}$, where ω_{cr} now directly affects the lifetime. Disregarding reabsorption effects, the transfer efficiency near 10°K is about 80% for the 2.1% ruby and about 20% for the 0.94% ruby where

$$\eta = \frac{\tau_R^* - \tau_R}{\tau_R^*}, \quad (140)$$

and τ_R^* is found from the data of Nelson and Sturge (1965) shown in Figure 32. Note that this transfer efficiency includes energy transfer from the R levels to all other excited levels.

The behavior of the N decays at low temperatures, where an initial rise is observed, can be explained as due to the presence of the conditions of Case A above. For both samples using only the first term in the square brackets in Eq. (136) we find values for t_{max} bigger (within one order of magnitude) than those given in Table 21. These values are given in Table 22. The second term in the brackets is negligible for both samples under the assumption that the N levels are pumped only through the R levels. The consideration of this first term gives the right trends for the dependence of t_{max} on temperature and concentration. To come closer to the experimental value, however, the second term in the brackets of Eq. (136) must be considered. The presence of direct pumping of the N levels from the absorption bands can actually make this term relevant, increasing the value of $n_2(0)$. The difference in the values listed in Tables 21 and 22 is considered as experimental evidence of the relevance of direct pumping at low temperatures. Notice also that for a 2.1% sample the decays after the rise have the lifetimes of the N levels, whereas for the 0.94% sample the decays after the rise have the lifetimes of the R levels. This is due to the fact that for t large enough, only the exponential with the longer lifetime persists.

For the band near 7750Å the decay times for both samples coincide with the decay times for the R and N lines in the thermalization range. At lower temperatures in the 2.1% sample an initial rise in fluorescence is observed with the subsequent decay having the R lifetime. For the 0.94% sample a double decay is observed at the band with the longer decay time being equal to the R lifetime.

Table 22. Theoretical Predictions for t_{\max}

Sample (% Cr)	T (°K)	Line	P_3 (sec ⁻¹)	A'_{21} (sec ⁻¹)	t_{\max} (sec)*
2.1	10	N_1	1.67×10^3	0.60×10^3	0.91×10^{-3}
		N_2	1.67×10^3	1.11×10^3	0.73×10^{-3}
		7750Å	1.67×10^3	0.77×10^3	0.86×10^{-3}
	73	N_1	1.67×10^3	1.02×10^3	0.30×10^{-3}
		N_2	1.67×10^3	1.26×10^3	0.68×10^{-3}
		7750Å	1.67×10^3	0.59×10^3	0.96×10^{-3}
0.94	15	N_1	0.40×10^3	0.60×10^3	2.00×10^{-3}
		N_2	0.40×10^3	1.11×10^3	1.44×10^{-3}
	81	N_1	0.38×10^3	1.02×10^3	1.53×10^{-3}
		N_2	0.38×10^3	1.26×10^3	1.35×10^{-3}

$$*t_{\max} \approx \frac{1}{A'_{21} - P_3} \ln \frac{A'_{21}}{P_3}.$$

These results indicate that the initial level of the band is in thermal equilibrium with the initial levels of the R, N_1 , and N_2 systems at high temperatures but not at low temperatures. The observed characteristics of the fluorescence decay fall into Case A for the 2.1% sample and into Case B for the 0.94% sample.

For the 2.1% sample (taking the shorter decay for the 0.94% sample as the intrinsic lifetime of the band) the consideration of the first term in the brackets of Eq. (136) gives for t_{\max} a value about 30 times larger than the experimental value. This seems to imply that for the band the direct pumping is very relevant at low temperatures. This is also in agreement with the fact that the band and the R system decouple at a higher temperature than the R and N systems (see Figures 33 and 34). As concentration decreases the ratio $N_2(0)/n_2(0)$ becomes larger, but ω_{cr} for the R \rightarrow band transfer is smaller. Apparently, as concentration goes from 2.1% to 0.94% the decrease in ω_{cr} exceeds the increase in the $N_2(0)/n_2(0)$ ratio shifting the conditions from Case A to Case B. A similar effect was found by Imbusch who observed a double decay for the N levels of a 0.2% ruby and,

consistent with our measurements, a fluorescence rise for the same levels in a 1% ruby (Imbusch, 1966).

10.3 Selective Lifetime Experiments

Selective lifetime measurements were also made on the 2.1% sample (No. 3 in Table 5) at 300°K and 78°K. The experimental arrangement described in Section 4.5 was used for these measurements. The FX-33 flashtube with a 100 μ f capacitor provided an excitation pulse of 150 μ sec duration at wavelengths selected by the Engis monochromator. The McPherson monochromator was used to monitor the fluorescence decay at the R_1 , N_1 , and N_2 lines and at the 7750 Å band while the sample was pumped in the two large absorption bands, the B lines, and the "pair band."

The results of these measurements are reported in Table 23. At the two temperatures investigated there seem to be no significant differences in decay times when pumping in the various absorption regions. The information of interest in these measurements is obtained in the type of fluorescence decay which is observed, that is, double decay, initial rise, or pure exponential. The low fluorescence intensity encountered in these experiments made it necessary to use a long excitation pulse to obtain sufficient energy input. This long pulse caused all the decays to appear as pure exponentials and thus no useful information was obtained. It should be noted, however, that the R_1 line was observed to be pumped through the "pair band."

Table 23. Selective Lifetimes in Ruby with 2.1% Cr

Pump Band (Å)	T = 78°K				T = 300°K			
	τ_{R_1} (msec)	τ_{N_1} (msec)	τ_{N_2} (msec)	$\tau_{7750\text{Å}}$ (msec)	τ_{R_1} (msec)	τ_{N_1} (msec)	τ_{N_2} (msec)	$\tau_{7750\text{Å}}$ (msec)
3400		1.03	0.70	0.67	1.64	1.56	1.50	1.40
4100	0.67	1.05	0.83	0.78	1.56	1.58	1.64	1.62
4775		1.03	0.85	0.72	1.48	1.40	1.44	1.32
5550		1.00	0.70	0.77	1.44	1.54	1.42	1.34

11. RESULTS AND DISCUSSION OF REABSORPTION EXPERIMENTS

The fluorescence spectrum of heavily doped ruby was described in Section 6. The changes in this spectrum were studied when the fluorescence from one ruby sample was passed through a similar non-fluorescing piece of material before being measured. This experiment had the purpose of studying the effects of reabsorption on the different lines of the spectrum, especially on those lines which originate from the pairs of Cr^{+3} ions. The effects of reabsorption on such lines can be used to bring further information on the assignment of the transitions and the consistency of the energy level scheme. It has also been found here that reabsorption may have some effects on the linewidths and relative intensities of fluorescent lines and may throw light on the interaction mechanisms between such systems as single and pair Cr^{+3} ions in ruby.

Jekeli (1965) has recently reported on reabsorption studies of ruby with 1% (atomic) Cr^{+3} . He saw no effects on the N_1 and N_2 lines due to reabsorption, but observed that the R_1 and R_2 lines were self-reversed after the exciting radiation had traveled through only a small amount of material.

The effects of reabsorption on all the fluorescence lines of ruby with 2.1% chromium were studied at 70°K, at 125°K, and at 307°K. The fluorescence spectrum at each temperature was compared to the spectrum which resulted from passing the emission through a second sample of 3.25-mm thickness. The R_1 and R_2 lines were observed to be self-reversed in agreement with Jekeli's (1965) work. In general the widths and intensities of the other spectral lines were changed but the effects of the reabsorption were different for each line and varied with temperature. The results can be explained by considering the absorption cross sections for the lines, the populations of the various energy levels, and the dynamics of the excitation of these levels.

The experimental apparatus used for the measurements was the continuous fluorescence equipment described in Section 4 with the monochromator set for a resolution of 0.75 Å.

For observation of the reabsorbed spectra two samples were mounted on the cold finger of the cryostat with their c-axes oriented in the same direction. One sample was exposed to the exciting radiation; the second sample was placed between the first sample and the monochromator and shielded from the exciting radiation. Thus, the fluorescence from the first sample had to pass through 3.25 mm of non-excited material before being detected. The 2.1% ruby samples that were used were cut from the same region of the same boule. They are listed as sample Nos. 5 and 6 in Table 5.

11.1 Experimental Results

The results of these measurements made at 307°K are shown in Figure 36. The R lines at this temperature are both self-reversed and are affected almost equally by the presence of the second sample. The N lines are both broadened in the reabsorbed spectrum and have much smaller decreases in intensity than the R lines.

Figure 37 shows the results obtained at 125°K. The R lines are slightly less self-reversed than they were at room temperature. The N lines are both greater in the reabsorption spectrum than in the fluorescence spectrum at this temperature considering the respective backgrounds. Along with the R and N lines the numerous other pair lines are visible at this temperature. In general reabsorption causes a slight broadening and enhancement of these lines relative to the background at this temperature.

The results of these measurements near 70°K are shown in Figure 38. The self-reversal of both the R lines is greater than at either of the higher temperatures. Also, the amount of enhancement of both the N lines is greatest at this temperature. The enhancement of the other pair lines is smaller at this temperature in the presence of the second sample and some of them show a loss in intensity in the presence of the second sample.

Tables 24 and 25 list the reabsorption data of the R and N lines. The reabsorption ratios shown in the first table are the peak height of each reabsorbed line divided by the peak height of the same line in fluorescence multiplied by a factor for normalizing the two backgrounds. Thus the smaller numbers indicate a greater intensity loss due to reabsorption. Numbers greater than one indicate an enhancement of the line due to reabsorption.

The linewidths of the N lines are shown in the second table. For both lines, at all three temperatures, the reabsorbed linewidth is greater than that of the fluorescent line. Also for both lines the relative difference in linewidths is greatest at 125°K.

The fluorescence and reabsorbed spectra were also observed at wavelengths out to 8000 Å. An attempt was made to observe the effect of reabsorption on vibronic bands. However, due to the complexity of the spectrum in this region only the 7076 Å vibronic band could actually be measured at 125°K and 70°K. It appeared unaffected by reabsorption. The band at 7750 Å was observed to be greater in reabsorption than in fluorescence.

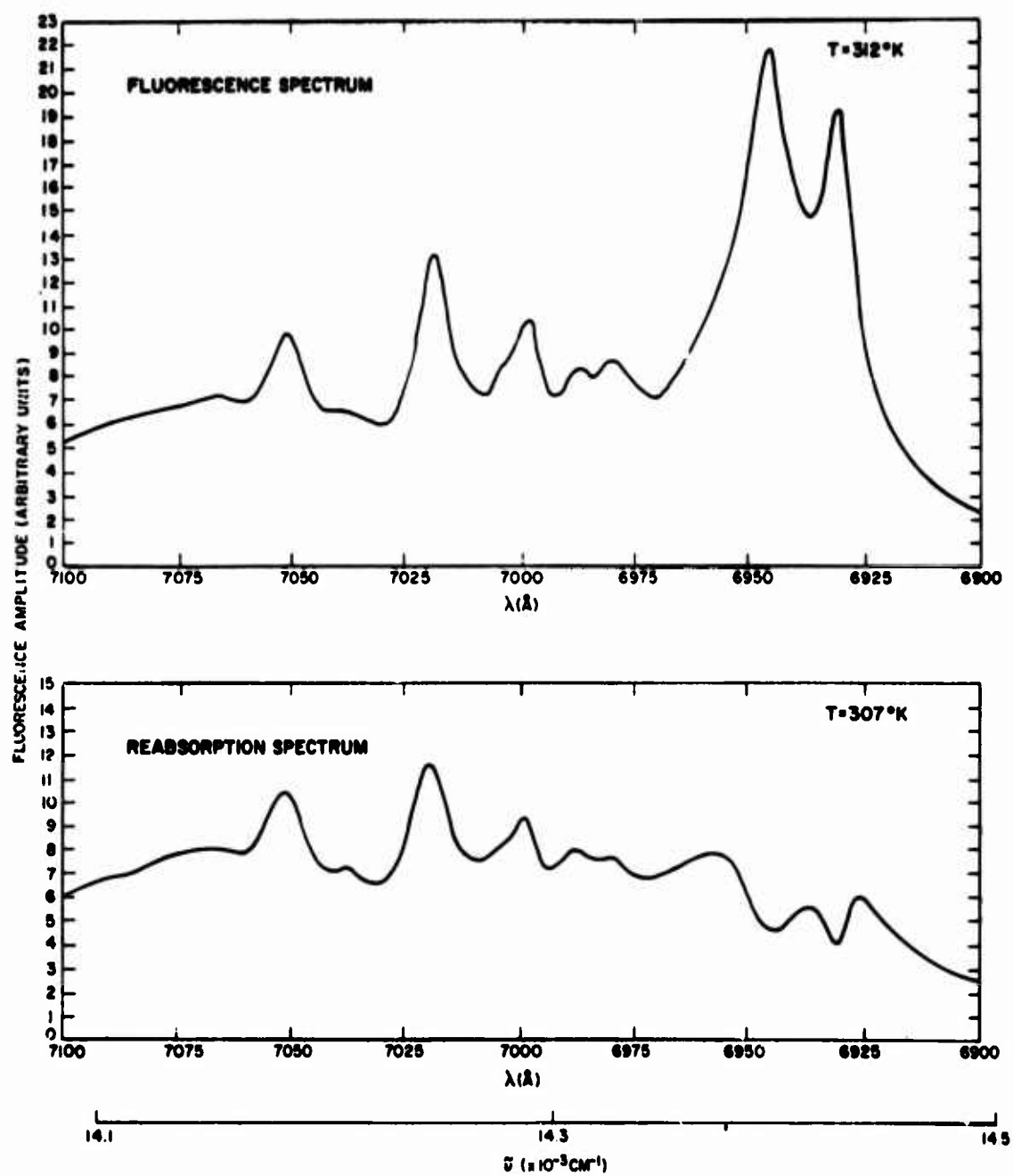


Figure 36. Fluorescence and Reabsorbed Spectra of Ruby with 2.1% Chromium Near 300°K

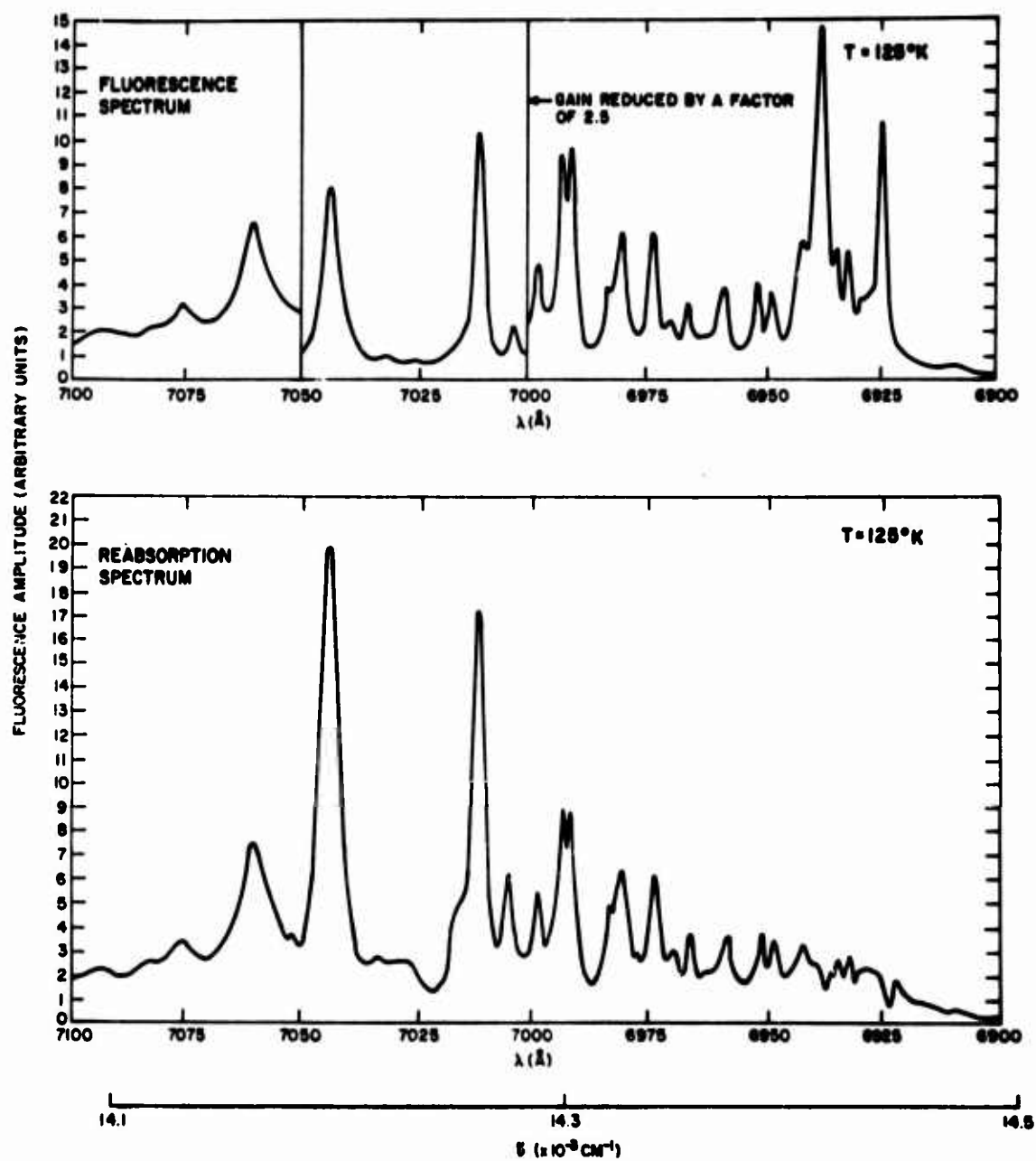


Figure 37. Fluorescence and Reabsorbed Spectra of Ruby with 2.1% Chromium Near 125°K

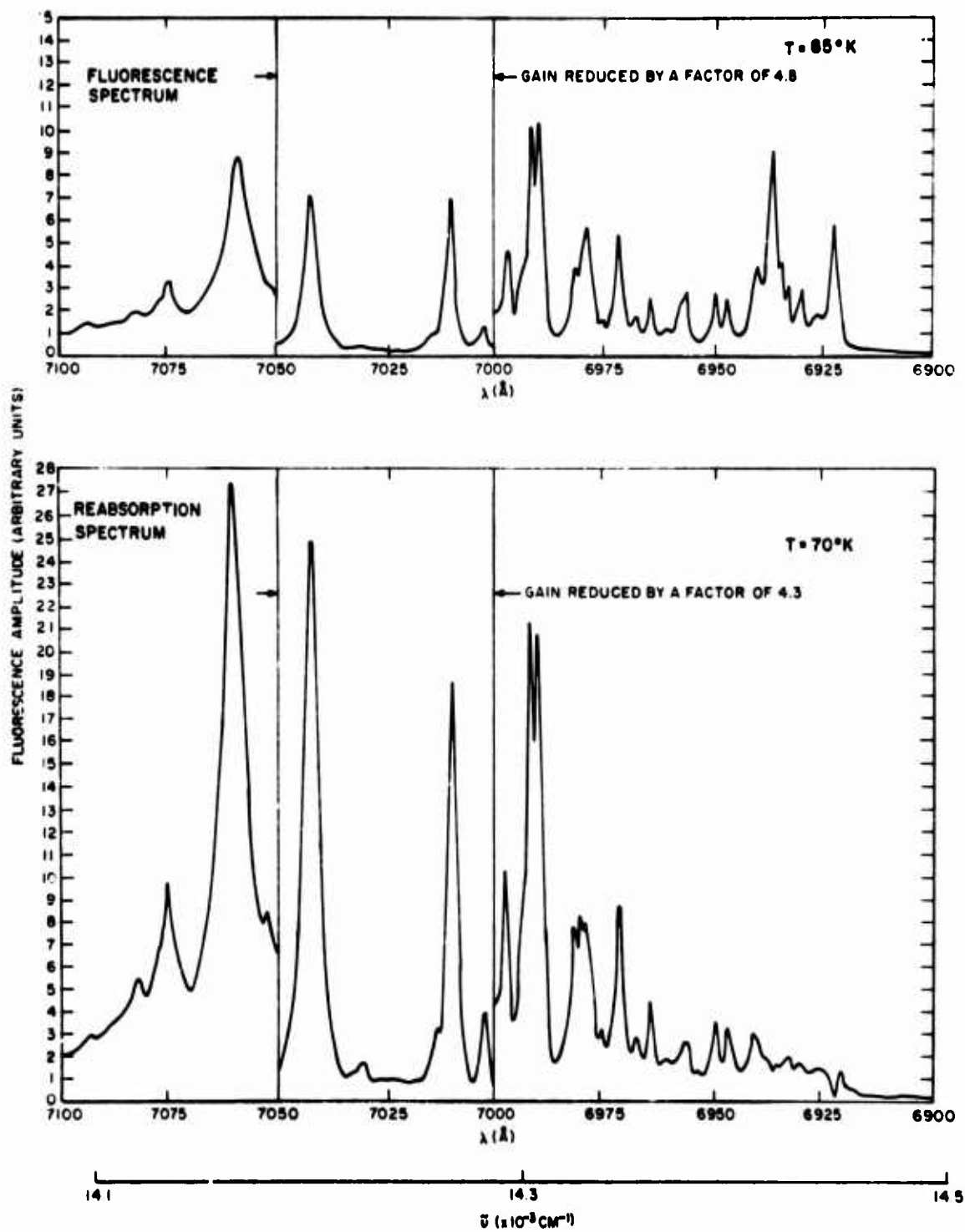


Figure 38. Fluorescence and Reabsorbed Spectra of Ruby with 2.1% Chromium Near 75°K

Table 24. Reabsorption Ratios I_{ra}/I_f

T (°K)	R ₂	R ₁	N ₂	N ₁
307	0.07	0.07	0.68	0.90
125	0.08	0.16	1.45	2.22
70	0.01	0.06	1.82	2.33

Table 25. Linewidths

T (°K)	N ₂			N ₁		
	$\Delta\lambda_f$	$\Delta\lambda_{ra}$	$\frac{\Delta\lambda_{ra} - \Delta\lambda_f}{\Delta\lambda_f}$	$\Delta\lambda_f$	$\Delta\lambda_{ra}$	$\frac{\Delta\lambda_{ra} - \Delta\lambda_f}{\Delta\lambda_f}$
307	10.2	11.8	0.2	14.0	16.0	0.1
125	2.4	3.4	0.4	3.5	4.3	0.2
70	1.8	2.0	0.1	3.4	3.9	0.1

11.2 Discussion of Reabsorption Effects

The effects which the second sample has on the fluorescence from the first sample can be divided into two categories. The first consists of the effects arising from the absorption of the radiation as it passes through the material. The second consists of the effects arising from the redistribution and possible re-emission of the absorbed energy.

The effects in the first category are exemplified for a typical fluorescence (normalized) line in Figure 39. After passing through a material of thickness d , the intensity of the line is decreased by a factor of $e^{-\alpha(\nu)d}$. Here $\alpha(\nu)$ is the absorption coefficient and equals $n\sigma(\nu)$ where n is the number of ions in the initial state of the absorption transition and $\sigma(\nu)$ is the absorption cross section. The intensity of the line is decreased to a different extent at each point due to the dependence of the absorption cross section on frequency. This frequency selective intensity decrease has two results. First, the linewidth at half maximum increases as the amount of reabsorption increases. Second, when $\alpha(\nu)d$ becomes greater than one, self-reversal begins. This condition also applies to a Gaussian line shape (Jekeli, 1965).

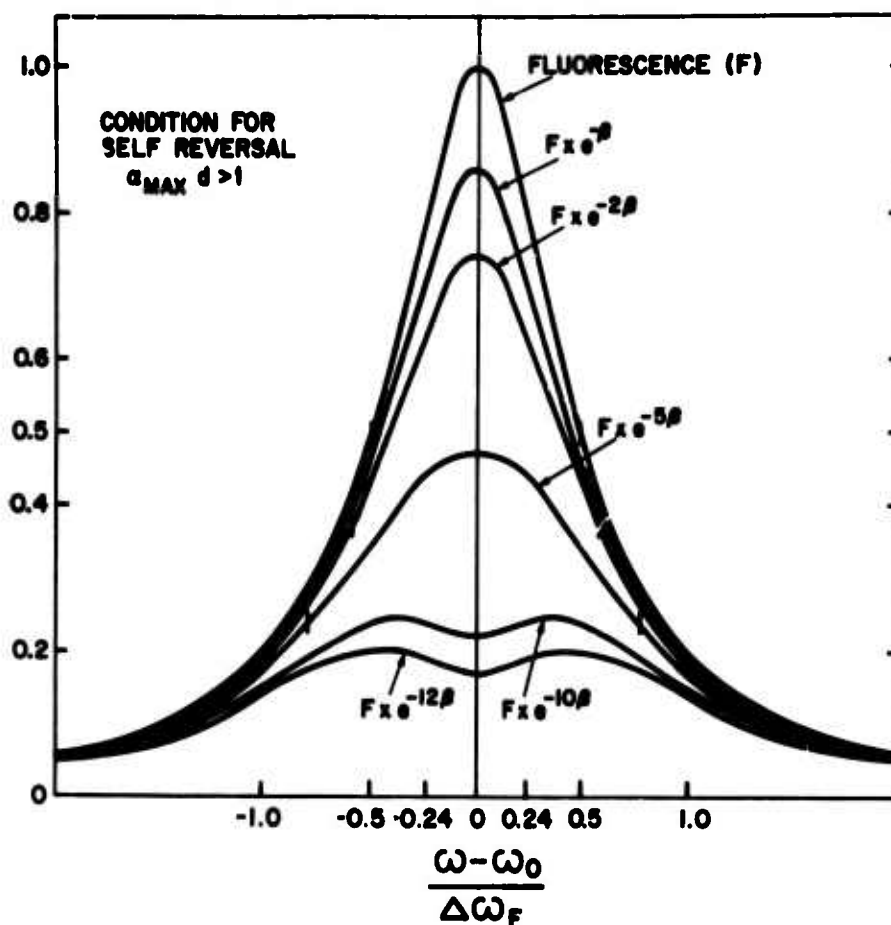


Figure 39. Shape of a Reabsorbed Line. The shape of $\beta(\nu)$ is assumed to be the same as that of the fluorescence line with $\beta_{\max} = 0.15$

The magnitude of these effects of reabsorption for a specific line depends on the following factors:

- (1) The concentration of the type of ions from which the line originates.
- (2) The distance the fluorescence travels through the unexcited material.
- (3) The absorption cross section.
- (4) The population of the lower level of the transition.

Factors (1) and (2) are independent of temperature but both (3) and (4) may be temperature dependent. The peak absorption cross section increases as temperature is lowered and its halfwidth becomes smaller.

In purely electronic transitions we expect the integrated absorption cross section to be constant at all temperatures as verified by Nelson and Sturge (1965) for ruby R lines. So we expect, in general, greater reabsorption at low temperature.

This effect has produced observed lengthening of the R lines' fluorescent lifetime (Varsanyi et al., 1959). The population of the lower level of the transition will depend on temperature if the level is part of a manifold of levels in thermal equilibrium. In this case population changes tend to cause fluorescence lines terminating on the ground state to show increasing reabsorption as temperature is lowered while those terminating on higher levels show decreasing reabsorption as temperature is lowered.

The second category of reabsorption effects involves the re-emission of the absorbed energy at frequencies other than that of the original line. The fluorescence line originating from a certain level may be reabsorbed and re-emitted by the second sample at different frequencies from the same or, in the case of an effective energy transfer, from another fluorescent level. Vibronic transitions may also decrease the amount of re-emission in a specific no-phonon line. If the material has two or more energy level systems, similar results are obtained if a fluorescence line associated with one system is reabsorbed by a transition of the same energy in the other system instead of by resonant reabsorption. The magnitude of these reabsorption effects depends on the probabilities for the various transitions involved. This can be a function of temperature in various ways depending on the type of transitions, that is, radiationless, vibronic, or cross-relaxation. The amount of vibronic loss decreases with decreasing temperature.

If the upper levels involved in a reabsorption transition are part of a manifold of states in thermal equilibrium, then a high frequency line, when reabsorbed, may actually be used by the second sample to pump optically the lower frequency lines of the same manifold. This effect, which is more enhanced at low temperatures when all the population drops into the lower metastable level, produces an apparent loss for the fluorescent signal at high frequency and an increase of the fluorescent signals at lower frequencies. It may happen that all the effects favoring the re-emission at a particular frequency may compensate and even overcome the reabsorption losses; in such a case, a fluorescence line may appear enhanced in the reabsorption spectrum.

Two points in the above discussion should be re-emphasized. First, fluorescent lines terminating on the ground state should, in general, be more affected by reabsorption than lines not terminating on the ground state. Second, in the reabsorbed spectrum each line is the superposition of the original fluorescence line attenuated by the second sample and of the emission from the second sample at the same frequency. The attenuation a line experiences increases the width of the line, whereas the additional energy emitted by the second sample produces the opposite effect.

11.3 Interpretation of Results

Let us now apply the conclusions of the previous section to the specific case of heavily doped ruby using the energy level diagram as shown in Figure 30. The R lines are most affected by reabsorption and are the only lines that are self-reversed. The presence of more single ions than pairs is one reason why the R lines show greater reabsorption effects than the rest of the lines. Both R line transitions have the ground state as their lower level and thus will be reabsorbed relatively strongly at all temperatures. The upper levels of their transitions are thermalized and the R_2 level is slightly higher than the R_1 level. Thus, some of the reabsorbed R_2 energy may be transferred to the R_1 level and re-emitted, causing the reabsorption loss of R_2 to be greater than that of R_1 . This effect is greater at lower temperatures where more of the population will drop into the lowest level. Both lines transfer energy to the pair systems, which adds to their reabsorption loss. Again this loss increases as temperature is lowered, as was seen in Section 9. These fluorescence lines may, however, increase with respect to the background at lower temperatures because of the smaller probability for vibronic emission. These two factors seem to balance each other in the temperature interval from 300°K down to 125°K. The energy transfer process dominates and the reabsorption losses increase from 125°K to 70°K.

Since the N lines both have as their lower levels one of the upper components of an exchange split ground state manifold, we expect them to be less reabsorbed at lower temperatures where the population of these levels decreases. At the same time, at low temperatures their upper levels become more populated since they are the lowest components of the excited state manifolds favoring the pumping of the N levels due to more energetic reabsorbed lines. Both these facts will cause any reabsorption losses to decrease as the temperature is lowered. The energy transfer from single ions to pairs tends also to increase the N line emission at the expense of the R line emission in both the fluorescence and reabsorbed spectra. This effect also increases as temperature is lowered in the temperature range investigated. At low temperatures the N lines are actually enhanced in the reabsorbed spectrum due to the dominance of this energy transfer. Since some of the energy of the N_2 line can be transferred to the N_1 line, the reabsorption ratios for the N_1 line are greater than those for the N_2 line.

As mentioned before, the widths of the N lines are greater in reabsorption than in fluorescence and the relative amount of broadening for both lines is greatest at 125°K. This indicates an increase in the attenuation of these lines between 307°K and 125°K, which may be attributed to an increase in absorption cross section at the central frequency. The decrease from 125°K down to 70°K may be due to the decrease in the lower level population or to the increase in fluorescence intensity at lower temperatures.

The temperature behavior of the reabsorption ratios of the other pair lines can be explained by considerations similar to those discussed above. For example, two lines in the N_1 pair system (6948.6 and 6964.7 Å), which in fluorescence originate from the uppermost state of the N_1 system and terminate respectively on the ground state and on a state 33 cm^{-1} above the ground state, present greater reabsorption at 70°K than at 125°K, due to the transfer of their reabsorbed energies to lower energy levels. At both temperatures the 6948.6 Å line is more reabsorbed than the 6964.7 Å line because the former fluorescence line terminates on the ground state and the latter one terminates on a higher level.

The vibronic band at 7076 Å was also measured at 125°K and 70°K and found to be unaffected by reabsorption, as expected.* However, the band near 7750 Å was more intense in the reabsorbed spectra than in fluorescence. This is attributed to the transfer of energy from the single ion levels to the band which was observed by lifetime measurements and excitation measurements.

12. SUMMARY AND CONCLUSIONS

An extensive spectroscopic investigation was conducted on heavily doped ruby. Absorption, excitation, continuous fluorescence, and pulse fluorescence measurements were made. The changes in the widths, positions, intensities, and lifetimes of the R_1 , R_2 , N_1 , and N_2 lines were measured at numerous temperatures from 13°K up to 700°K. Measurements were also made of the lifetimes at the 7750 Å band, of the intensities of all the lines of the second and fourth nearest neighbor pairs, and of the effects of reabsorption on the fluorescence spectrum. The results of these experiments are now summarized and conclusions, which can be drawn from these results, are discussed. Finally, several suggestions for further work in this area are mentioned.

12.1 Summary of Results

The various investigations discussed in Sections 5 through 11 led to the following results:

(1) A great deal of structure was reported in the absorption spectrum of heavily doped ruby near the S lines, the B lines, and the "pair band." Much of this structure has not been reported previously.

(2) The excitation spectra of heavily doped ruby showed the N lines to be pumped through the "pair band," the R lines, and at wavelengths slightly less than the R lines.

*Since low energy absorption vibronics disappear at low temperatures due to the lack of phonons for absorption, the reabsorbing sample is transparent to the low energy fluorescence vibronics at these temperatures.

(3) The continuous fluorescence measurements showed a very complex spectrum consisting of pair lines, a multiple ion band and vibronics. The vibronics were the most important emission process at high temperatures and the N lines were the dominant spectral feature at low temperatures.

(4) The energy level diagrams for the two established pair systems were constructed and numerous lines were assigned to transitions between levels in these systems. These results were consistent with previous investigations but one new level was established and four new lines were given assignments.

(5) The single-ion and the two-pair metastable levels were all observed to be in thermal equilibrium at high temperatures and to decouple at low temperatures. The temperature at which the levels decouple and the amount of deviation from thermalization were both greater for the less concentrated sample indicating that the probability for energy transfer between these levels is greater for more concentrated samples.

(6) A cross-relaxation process was proposed as the means of energy transfer between the R and N systems. In the scheme used this process produces thermalization of the R and N levels at high temperatures and allows continuous pumping from the R to the N levels at low temperatures. It was also established that the pumping efficiency is greater for the N_2 than for the N_1 level and that pumping from the R_2 level is greater than pumping from the R_1 level.

(7) The results of lifetime measurements made at the R and N lines and at the band near 7750 \AA were consistent with the results of intensity measurements in that all the decays were pure exponentials with the same decay time in the range of thermalization. The observations of initial rises in fluorescence and double decays, when the systems were decoupled, were indicative of the concentration and temperature dependence of the energy transfer process. The rate equations used to explain the relative intensity measurements were also used to explain the results of the lifetime measurements. Evidence was given for the presence of a certain amount of direct pumping from the absorption bands to the N levels and to the band at 7750 \AA at low temperatures.

(8) The thermal dependence of the widths of the R and N lines determined experimentally was explained by considering microscopic strain, direct phonon processes, and Raman scattering processes. The thermal dependence of the positions of the R and N lines was explained by considering the continual absorption and emission of virtual phonons by an impurity ion. A Debye distribution of phonons was used with different Debye temperatures for the line broadening processes and the lineshift processes. The broadening processes for the R lines were also explained using a different Debye temperature than that used for the N lines. For the direct process contribution to the broadening of the N lines only phonon transitions in the ground state manifolds with the selection

rule $\Delta S = \pm 2$ were found to be important.

(9) The changes in the fluorescence spectrum of heavily doped ruby were studied when the emission from one sample was passed through a similar nonfluorescing piece of material before being measured. Reabsorption was seen to affect all the no-phonon lines in the fluorescence spectrum of heavily doped ruby. The R lines were self-reversed and the N lines enhanced due to reabsorption. The intensities of the numerous other pair lines were also affected by reabsorption; some increased, others decreased, consistently with the energy level schemes constructed previously for the single ion and pair systems and with the observed energy transfer between these systems. The reabsorbed lines were all observed to be broadened due to the frequency dependence of the absorption cross section. No effects of reabsorption were observed on the vibronics. The band near 7750 Å was enhanced by reabsorption due to the energy transfer to it from the single-ion levels.

12.2 Discussion of Results and Conclusions

The results listed in the previous section indicate the wide variety of information obtainable from spectroscopic investigations of paramagnetic ions in crystals. Knowledge was obtained about the environment of the impurity ion, the vibrations of the host lattice, and the quantum electronic aspects of the whole system.

The high intensity of the S and B lines and their satellite lines in the absorption spectrum of ruby with 2.1% Cr shows one important reason for the study of heavily doped materials. The increased intensity facilitates the analysis of the results. This is due to the fact that the large number of absorbing centers compensates for the weakness of those transitions which are forbidden by the selection rules. These results can be correlated, in principle, with results obtained using the new experimental technique of excited state absorption. In these experiments on ruby, spin allowed doublet-doublet transitions are observed instead of the spin forbidden quartet-doublet transitions appearing in the ground state absorption spectrum.

Also the knowledge of pair effects gained from the study of heavily doped crystals is of practical importance even though most crystals used in device applications are lightly doped. In Section 6 it was seen that pair lines may appear in the fluorescence spectrum of ruby with 0.03% Cr. Thus, ion pairs may provide a loss mechanism for crystals used as lasers.

An important conclusion to be drawn from the results of the fluorescence work is the validity of a model of ruby which allows for the existence of individual optically active systems of single ions and pairs, the relevance of the various systems being determined by the concentration of chromium. This follows from the observation that lines within each system remain thermalized at low temperatures but

they are not thermalized with lines belonging to other systems.

Another important conclusion is the validity of a cross-relaxation model for the interaction between the single-ion and pair systems. This model predicts the thermalization observed at high temperatures and the pumping of the lower levels at low temperatures. The observed thermalization at high temperatures of levels belonging to different systems indicates the nonradiative character of the interaction. A radiative energy transfer would take too long to permit thermalization. Further evidence in favor of the cross-relaxation model is found from the fluorescent lifetime measurements. This model explains the observed temperature and concentration dependence of the various lifetimes observed in both the high and low temperature ranges.

The results obtained in this work show the importance of studying energy transfer in crystals over a wide range of temperatures, rather than at two or three temperatures as it is usually done. The energy transfer may depend on temperature in such a way that different results are obtained at high temperatures (for example, thermalization) and at low temperatures (pumping of the lower levels).

The results of this work also show the importance of correlating lifetime and intensity measurements. The same physical model should be used in explaining the results of the two types of measurements. The mathematical expressions obtained from the theoretical model should be solved under equilibrium conditions to explain the results of intensity measurements and under dynamical conditions to explain the results of lifetime measurements.

The use of different Debye temperatures in explaining the observed thermal dependence of the widths of the R and N lines indicates that the effective phonon distributions are different for Raman scattering by single ions and by pairs. Similarly, the lineshift processes have different effective phonon distributions than the line broadening processes. The different values of μ used for the two samples investigated indicate that the coupling of the active ions to the lattice increases with concentration. The results of the linewidth and lineshift studies also show the relevance of direct processes and can be used to determine the presence of specific types of processes [for example, Orbach processes (Yen et al., 1965)]. An indication of the lifetimes of certain states can also be obtained from these measurements. The selection rule $\Delta S = \pm 2$ obtained for the ground state manifolds of the pair systems implies long lifetimes for levels $S = 1$ of the N_1 system and for $S = 2$ of the N_2 system and the feasibility of the use of these levels for submillimeter maser action (Strain, 1963).

The model used for ruby with interacting single-ion and pair systems is consistent with the results of the reabsorption experiments. Energy transfer may cause an enhancement of some of the reabsorbed lines. Reabsorption itself has the greatest effect on lines terminating on the ground state. Due to energy

transfer, however, fluorescence lines not terminating on the ground state may be significantly changed in the reabsorbed spectrum. Also, the width of a reabsorbed line, as well as its intensity, is important since it may give an indication of the extent of reabsorption even for a line whose intensity is enhanced.

12.3 Implications for Further Work

The results obtained in this investigation suggest several interesting topics which could be the subject of future work:

(1) A rigorous theoretical explanation of the coupling of the ion pairs is needed to successfully explain the excited state splittings and the magnitudes of J.

(2) More experimental work using samples with a wider range of concentration is needed to firmly establish the nature of the coupling mechanism between single ions and pairs (Imbusch, 1966).

(3) The regions near the B and S lines in the absorption spectrum of heavily doped ruby should be investigated further to determine the possible vibronic or pair nature of the numerous transitions observed in these regions. Also the absorption "pair band" should be further studied to establish the nature of the transitions giving rise to it.

(4) Excitation experiments should be performed using greater resolution in order to better ascertain the pumping processes which excite the N lines, especially by pumping in the pair band and at wavelengths slightly shorter than the R lines. Low emission intensities may, however, prove to be a problem in this work.

(5) The origin of the fluorescence band near 7750 \AA should be better established and the vibronic spectrum of heavily doped ruby should be determined. Also the satellite lines appearing near the R lines of heavily doped ruby in both absorption and fluorescence should be given assignments.

(6) A quantitative explanation of the relative intensity measurements should be attempted using the cross-relaxation model developed in Section 9.

(7) It would also be interesting to perform reabsorption measurements similar to those described in Section 11 using pulsed excitation. This would indicate the effects of reabsorption on fluorescence lifetimes.

(8) Lifetime measurements at some of the most prominent pair lines other than N_1 and N_2 (for example, 6948.6 \AA , 6989.4 \AA , 7001.8 \AA , and 7058.2 \AA) should be made. This would give further confirmation of their assignment to specific pair systems and of the energy transfer from the R to the N systems.

It is obvious that even with the voluminous amount of literature available on ruby there is still a great deal which is not understood about this material and which could be the subject of further fruitful studies.

Acknowledgments

The author wishes to acknowledge the help he received from Dr. B. DiBartolo, Dr. C.S. Naiman, and Mr. B. Birang of Mithras Inc., Cambridge, Massachusetts.

References

- Bak, T.A., ed. (1964) Phonons and Phonon Interactions, W.A. Benjamin, Inc., New York, Introductory lectures on the free phonon field, by H. Jensen, p.1.
- Brown, G.C. (1964) Measurement of Relaxation Times of Paramagnetic Ions in Crystals: Ruby, Tech Rpt No. AF-111, Johns Hopkins University, Carlyle Barton Laboratory.
- Burns, G., and Nathan, M. (1963) Quantum efficiency of ruby, J. Appl. Phys. 34:703.
- Clogston, A.M., Emission Spectrum of Exchange Coupled Chromium Ions in Ruby, Bell Telephone Laboratories, unpublished report.
- Cohen, M.G., and Bloembergen, N. (1964) Magnetic- and electric-field effects of the B_1 and B_2 absorption lines in ruby, Phys. Rev. 135:A950.
- Czerny, M., and Turner, A.F. (1930) Uber den A stigmatismus bei Spiegelspektrometern, Z. Physik 61:792.
- Daly, R.T. (1961) Paper No. TB16, Fluorescence of the Cr^{+++} Pair Spectrum in Synthetic Ruby, presented at the Optical Society of America Meeting in Pittsburgh, Penn.
- Deutschbein, O. (1932) Linienhafte Emission d. Chromphosphore I, Ann. Physik 5:722.

References

- Deutschbein, O. (1962) Radiative and Non-Radiative Transitions in Rubies, report from the Centre National D'Etudes Des Telecommunications.
- Dexter, D.L. (1958) Theory of optical properties of imperfections in nonmetals, in Solid State Physics, edited by F. Seitz and D. Turnbull, Academic Press Inc., New York, Vol. 6, p. 404.
- Dodd, D.M., Wood, D.L., and Barns, R.C. (1964) Spectrophotometric determination of chromium concentration in ruby, J. Appl. Phys. **35**:1183.
- Geschwind, S., and Remeika, J.P. (1962) Spin resonance of transition metal ions in corundum, J. Appl. Phys. **33** (Suppl.):370.
- Gill, J.C. (1962) Spin-lattice relaxation of chromium ions in ruby, Proc. Phys. Soc. (London) **79**:58.
- Griffith, J.S. (1961) The Theory of Transition-Metal Ions, Cambridge University Press, Cambridge, p. 52.
- Hettler, W. (1954) The Quantum Theory of Radiation, Oxford University Press, London, p. 54.
- Imbusch, G.F., Yen, W.M., Schawlow, A.L., McCumber, D.E., and Sturge, M.D. (1964) Temperature dependence of the width and position of the ${}^2E \rightarrow {}^4A_2$ fluorescence lines of Cr^{3+} and V^{2+} in MgO, Phys. Rev. **133**:A1029.
- Imbusch, G.F. (1966) Energy Transfer in Ruby, Paper No. 7B-5 presented at the Quantum Electronics Meeting in Phoenix, Arizona.
- Jacobs, S.F. (1956) Spectra and Zeeman Effects of Ruby Single Crystals at Low Temperatures, doctorate thesis, Johns Hopkins University, Baltimore, Md.
- Jekeli, W. (1965) Self-reversal of R lines in red ruby, J. Opt. Soc. Am. **55**:1442.
- Kaplyanskii, A., and Prevuskii, A. (1962) Strain induced splitting of the U-band and the John-Teller effect in excited 4T_2 state of Cr^{+3} ions in ruby, Soviet Phys. -Doklady **7**:37.
- Kisliuk, K., and Krupke, W.F. (1963) Biquadratic exchange energy in ruby -- 0.5% Cr_2O_3 , Appl. Phys. Letters **3**:213.
- Kisliuk, P., Schawlow, A.L., and Sturge, M.D. (1964) Energy levels in concentrated ruby, in Quantum Electronics, edited by P. Grivet and B. Bloembergen, Columbia University Press, New York, Vol. 3, p. 725.
- Kisliuk, K., and Krupke, W.F. (1965) Exchange interactions between chromium ions in ruby, J. Appl. Phys. **36**:1025.
- Kittel, C. (1956) Introduction to Solid State Physics, John Wiley and Sons Inc., New York, p. 128.
- Kittel, C. (1963) Quantum Theory of Solids, John Wiley and Sons Inc., New York.
- Krishnan, R.S. (1947) Raman spectrum of alumina and the luminescence and absorption spectra of ruby, Nature **160**:26.
- Kurnit, N.A., Abella, I.D., and Hartmann, S.R. (1966) Photon echoes in ruby, in Physics of Quantum Electronics, edited by P.L. Kelley, B. Lax, and P.O. Tannewald, McGraw Hill Book Company Inc., New York, p. 267.
- Kushida, T., Emission Properties of Satellite Bands Near the R Lines of Ruby, unpublished.
- Linz, A., and Newnham, R.E. (1961) Ultraviolet absorption spectra in ruby, Phys. Rev. **123**:500.

References

- Louisell, W. (1964) Radiation and Noise in Quantum Electronics, McGraw-Hill Book Company Inc., New York, p. 195.
- Low, W. (1960) Absorption Lines of Cr^{+3} in Ruby, J. Chem. Phys. 33:1162.
- Margerie, J. (1962) Identification des Composantes de la Transition $^4\text{A}_2 \rightarrow ^2\text{F}_1$ du Rubis, Compt. Rend. 255:1598.
- McClure, D. (1959) Electronic Spectra of Molecules and Ions in Crystals, Academic Press Inc., New York, p. 137.
- McClure, D.S. (1962) Optical spectra of transition-metal ions in corundum, J. Chem. Phys. 36:757.
- McCumber, D.E., and Sturge, M. C. (1963) Linewidth and temperature shift of the R lines in ruby, J. Appl. Phys. 34:1682.
- Misu, A. (1964) Emissions of ruby, J. Phys. Soc. Japan 19:2260.
- Mollenauer, L.F. (1965) Exchange-Coupled Chromium Ion Pairs in Ruby, doctorate thesis, Stanford University, Palo Alto, California.
- Naiman, C.S., and Linz, A. (1963) The ultraviolet absorption spectra in ruby, reprinted from the Proceedings of the Symposium on Optical Masers, Polytechnic Institute of Brooklyn.
- Nelson, D.E., and Sturge, M.D. (1965) Relation between absorption and emission in the regions of the R lines of ruby, Phys. Rev. 137:A117.
- Orbach, R. (1962) Spin-lattice relaxation in solids, in Fluctuation, Relaxation and Resonance in Magnetic Systems, edited by D. ter Haar, Plenum Press, New York, p. 219.
- Posener, D.W. (1959) The shape of spectral lines: Tables of the Voigt Profile

$$\frac{a}{\pi} \int_{-\infty}^{\infty} \frac{e^{-y^2} dy}{a^2 + (v-y)^2}, \text{ Australian J. Phys. 12:184.}$$
- Pringsheim, P. (1949) Fluorescence and Phosphorescence, Interscience Publishers Inc., New York, p. 641.
- Schawlow, A.L., Wood, D.L., and Clogston, A.M. (1959) Electronic spectra of exchange-coupled ion pairs in crystals, Phys. Rev. Letters 3:271.
- Schawlow, A.L., and Devlin, G.E. (1961) Simultaneous maser action in two ruby satellite lines, Phys. Rev. Letters 6:96.
- Siegman, A.E. (1964) Microwave Solid State Masers, McGraw Hill Book Co. Inc., New York, p. 235.
- Statz, H., Rimai, L., Weber, M.J., and DeMars, G.A. (1961) Chromium ion pair interactions in the paramagnetic resonance spectrum of ruby, J. Appl. Phys. 32 (Suppl.):218S.
- Strain, R.J. (1963) Submillimeter Wave Quantum Electronics Using Ion Pairs in Ruby, doctorate thesis, University of Illinois, Urbana, Illinois.
- Sugano, S., and Tanabe, Y. (1958) Absorption spectra of Cr^{+3} in Al_2O_3 , Part A. Theoretical studies of the absorption bands and lines, J. Phys. Soc. Japan 13:880.
- Sugano, S., and Tsujikawa, I. (1958) Absorption spectra of Cr^{+3} in Al_2O_3 , Part B. Experimental studies of the Zeeman effect and other properties of the line spectra, J. Phys. Soc. Japan 13:899.

References

- Sugano, S., and Peter, M. (1961) Effect of configuration mixing and covalency on the energy spectrum of ruby, Phys. Rev. 122:381.
- Tolstoi, N.A., and Tkachuk, A.M. (1959) Investigation of the spectral distribution of the luminescence decay time of ruby by the pulse Taumeter method, Opt. Spectry. (USSR) 6:427.
- Tolstoi, N.A., Shun'-Fu, Liu, and Lapidus, M.E. (1962) Luminescence kinetics of chromium luminors, III, Ruby, Opt. Spectry. (USSR) 13:133.
- Tolstoi, N.A., and Abramov, A.P. (1963) Luminescence kinetics of chromium phosphors, VII. The interaction of chromium ions, Opt. Spectry. (USSR) 14:365.
- Varsanyi, F., Wood, D.L., and Schawlow, A.L. (1959) Self-absorption and trapping of sharp-line resonance radiation in ruby, Phys. Rev. Letters 3:544.
- Wieder, I., and Sarles, L.R. (1961) Scattering of resonance radiation in ruby, . Advances in Quantum Electronics, edited by J. Singer, Columbia University Press, New York, p. 214.
- Wieder, I., and Sarles, L.R. (1961) Stimulated optical emission from exchange-coupled ions of Cr^{+3} in Al_2O_3 , Phys. Rev. Letters 6:95.
- Wyckoff, R.W.G. (1948) Crystal Structure, Interscience Publishers Inc., New York, Vol. II, p. 7.
- Yen, W.M., Scott, W.C., and Schawlow, A.L. (1964) Phonon-induced relaxation in excited optical states of trivalent praseodymium in LaF_3 , Phys. Rev. 136:A271.
- Yen, W.M., Scott, W.C., and Scott, P.L. (1965) Correlation of the Orbach relaxation coefficient with optical linewidths: $\text{LaF}_3:\text{Er}^{3+}$, Phys. Rev. 137:A1109.

Unclassified

Security Classification

DOCUMENT CONTROL DATA - R&D		
(Security classification of title, body of abstract and indexing a notation must be entered when the overall report is classified)		
1. ORIGINATING ACTIVITY (Corporate author)		2a. REPORT SECURITY CLASSIFICATION
Hq AFCRL, OAR (CRW) United States Air Force Bedford, Massachusetts		Unclassified
		2b. GROUP
		-
3. REPORT TITLE		
The Interaction of Chromium Ions in Ruby Crystals		
4. DESCRIPTIVE NOTES (Type of report and inclusive dates)		
Scientific Report, Interim.		
5. AUTHOR(S) (Last name, first name, initial)		
POWELL, Richard C.		
6. REPORT DATE	7a. TOTAL NO. OF PAGES	7b. NO. OF REFS
December 1966	130	59
8a. CONTRACT OR GRANT NO.	9a. ORIGINATOR'S REPORT NUMBER(S)	
	AFCRL-66-830 PSRP No. 299	
b. PROJECT AND TASK NO. 5620-05		
c. DOD ELEMENT 61445014	9b. OTHER REPORT NO(S) (Any other numbers that may be assigned this report)	
d. DOD SUBELEMENT 681301	AFCRL-66-830	
10. AVAILABILITY/LIMITATION NOTICES		
Distribution of this document is unlimited.		
11. SUPPLEMENTARY NOTES		12. SPONSORING MILITARY ACTIVITY
		Hq AFCRL, OAR (CRW) United States Air Force Bedford, Massachusetts
13. ABSTRACT		
<p>Absorption, excitation, continuous fluorescence, and pulse fluorescence measurements were made on ruby samples with 0.94% and 2.1% Cr^{+3} in the temperature range from 4.2°K up to 700°K. The widths, positions, intensities, and lifetimes of the R and N fluorescence lines were determined at numerous temperatures.</p> <p>The results for the temperature dependence of the linewidths are explained in terms of microscopic strains, Raman scattering of phonons by the impurity ions, and direct phonon processes. The results for the lineshifts with temperature are due to the absorption and emission of virtual phonons.</p> <p>Ratios of the intensities of the R_1, R_2, and N_2 lines to the N_1 line are proportional to the relation $\exp[-\Delta E/(KT)]$ at high temperatures but not at low temperatures, indicating that energy transfer between single-ion and double-ion systems is temperature and concentration dependent. The temperature dependence of the relative intensity ratios of the no-phonon lines is used to construct energy level diagrams for two pair systems and to assign the lines to specific transitions.</p> <p>The observed lifetimes of the R and N lines coincide in the temperature range where the systems are thermalized and the observed decays are pure exponentials. At temperatures where the systems are decoupled, an initial rise in fluorescence is observed at the N lines. The subsequent decay has the lifetime of the R lines for a 0.94% sample and the lifetime of the N lines for a 2.1% sample. These results are also explained in terms of energy transfer from single ions to pairs.</p> <p>The effects of reabsorption on the fluorescence spectrum are also discussed. ()</p>		

DD FORM 1473
1 JAN 64

Unclassified

Security Classification

Unclassified
Security Classification

14. KEY WORDS	LINK A		LINK B		LINK C	
	ROLE	WT	ROLE	WT	ROLE	WT
Ruby Quantum Electronics Energy Transfer Linewidths Lifetimes Pair Effects Spectroscopy Reabsorption						

INSTRUCTIONS

1. ORIGINATING ACTIVITY: Enter the name and address of the contractor, subcontractor, grantee, Department of Defense activity or other organization (*corporate author*) issuing the report.

2a. REPORT SECURITY CLASSIFICATION: Enter the overall security classification of the report. Indicate whether "Restricted Data" is included. Marking is to be in accordance with appropriate security regulations.

2b. GROUP: Automatic downgrading is specified in DoD Directive 5200.10 and Armed Forces Industrial Manual. Enter the group number. Also, when applicable, show that optional markings have been used for Group 3 and Group 4 as authorized.

3. REPORT TITLE: Enter the complete report title in all capital letters. Titles in all cases should be unclassified. If a meaningful title cannot be selected without classification, show title classification in all capitals in parentheses immediately following the title.

4. DESCRIPTIVE NOTES: If appropriate, enter the type of report, e.g., interim, progress, summary, annual, or final. Give the inclusive dates when a specific reporting period is covered.

5. AUTHOR(S): Enter the name(s) of author(s) as shown on or in the report. Enter last name, first name, middle initial. If military, show rank and branch of service. The name of the principal author is an absolute minimum requirement.

6. REPORT DATE: Enter the date of the report as day, month, year, or month, year. If more than one date appears on the report, use date of publication.

7a. TOTAL NUMBER OF PAGES: The total page count should follow normal pagination procedures, i.e., enter the number of pages containing information.

7b. NUMBER OF REFERENCES: Enter the total number of references cited in the report.

8a. CONTRACT OR GRANT NUMBER: If appropriate, enter the applicable number of the contract or grant under which the report was written.

8b, 8c, & 8d. PROJECT NUMBER: Enter the appropriate military department identification, such as project number, subproject number, system numbers, task number, etc.

9a. ORIGINATOR'S REPORT NUMBER(S): Enter the official report number by which the document will be identified and controlled by the originating activity. This number must be unique to this report.

9b. OTHER REPORT NUMBER(S): If the report has been assigned any other report numbers (either by the originator or by the sponsor), also enter this number(s).

10. AVAILABILITY/LIMITATION NOTICES: Enter any limitations on further dissemination of the report, other than those imposed by security classification, using standard statements such as:

- (1) "Qualified requesters may obtain copies of this report from DDC."
- (2) "Foreign announcement and dissemination of this report by DDC is not authorized."
- (3) "U. S. Government agencies may obtain copies of this report directly from DDC. Other qualified DDC users shall request through _____."
- (4) "U. S. military agencies may obtain copies of this report directly from DDC. Other qualified users shall request through _____."
- (5) "All distribution of this report is controlled. Qualified DDC users shall request through _____."

If the report has been furnished to the Office of Technical Services, Department of Commerce, for sale to the public, indicate this fact and enter the price, if known.

11. SUPPLEMENTARY NOTES: Use for additional explanatory notes.

12. SPONSORING MILITARY ACTIVITY: Enter the name of the departmental project office or laboratory sponsoring (paying for) the research and development. Include address.

13. ABSTRACT: Enter an abstract giving a brief and factual summary of the document indicative of the report, even though it may also appear elsewhere in the body of the technical report. If additional space is required, a continuation sheet shall be attached.

It is highly desirable that the abstract of classified reports be unclassified. Each paragraph of the abstract shall end with an indication of the military security classification of the information in the paragraph, represented as (TS), (S), (C), or (U).

There is no limitation on the length of the abstract. However, the suggested length is from 150 to 225 words.

14. KEY WORDS: Key words are technically meaningful terms or short phrases that characterize a report and may be used as index entries for cataloging the report. Key words must be selected so that no security classification is required. Identifiers, such as equipment model designation, trade name, military project code name, geographic location, may be used as key words but will be followed by an indication of technical context. The assignment of links, rules, and weights is optional.

Unclassified
Security Classification